eman ta zabal zazu

Universidad del País Vasco
Euskal Herriko Unibertsitatea

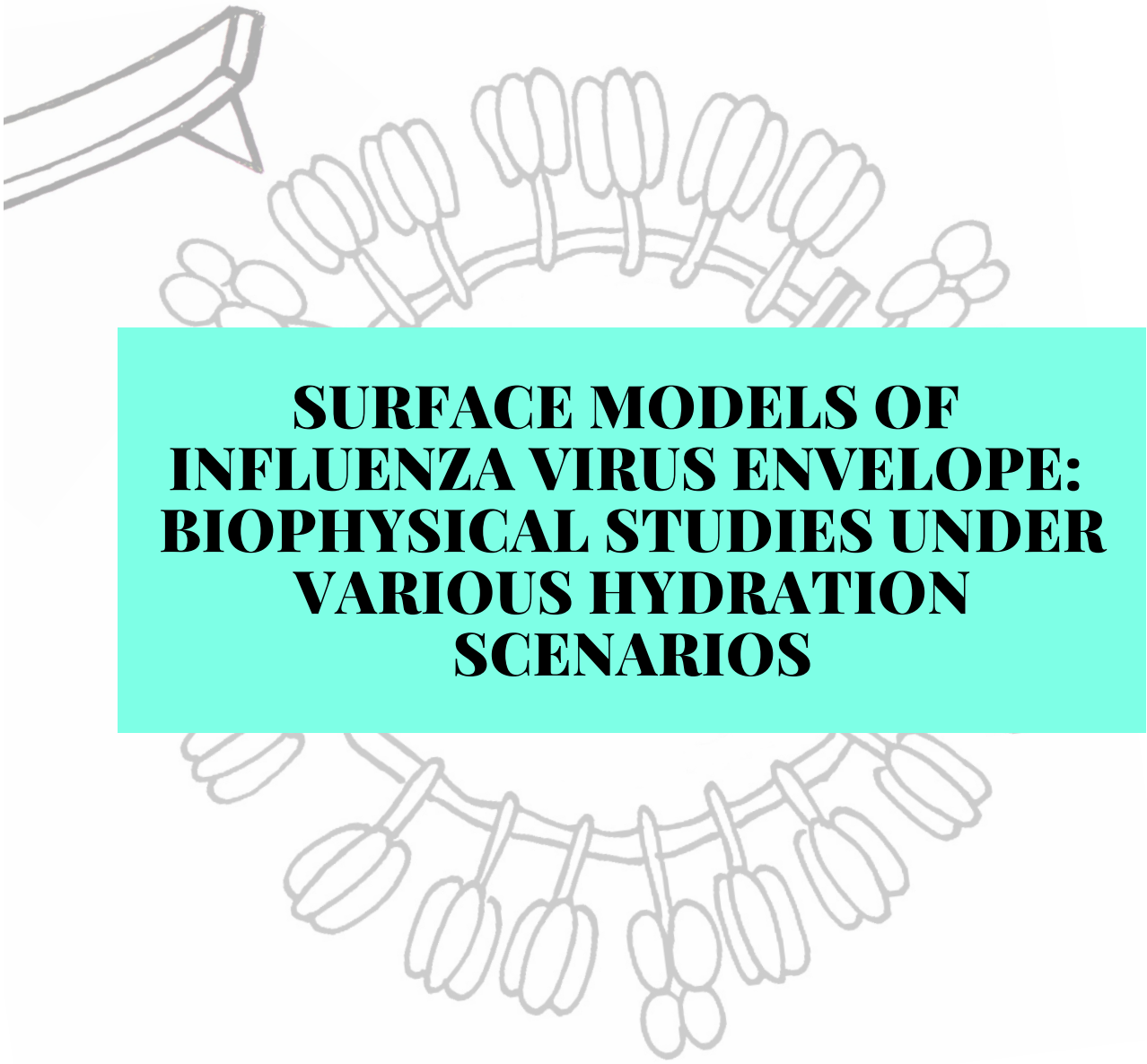

SURFACE MODELS OF INFLUENZA VIRUS ENVELOPE: BIOPHYSICAL STUDIES UNDER VARIOUS HYDRATION SCENARIOS

MAIARA A. IRIARTE ALONSO

PhD thesis

2022

eman ta zabal zazu

Universidad del País Vasco
Euskal Herriko Unibertsitatea

UNIVERSITY OF THE BASQUE COUNTRY

Surface models of Influenza virus envelope: Biophysical studies under various hydration scenarios

Dissertation presented to the
Department of Advanced Polymers and Materials:
Physics, Chemistry and Technology

For the degree of
Doctor of Philosophy

Presented by

MAIARA A. IRIARTE ALONSO

Supervised by

Dr. Alexander M. Bittner
& Dr. Silvina Cerveny Murcia

FEBRUARY 2022

"Influenza virus" (J. de Combi)

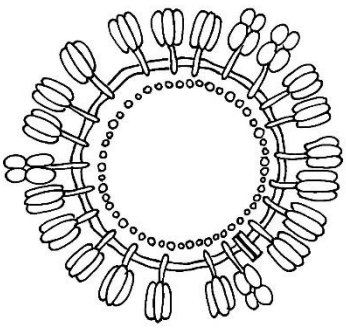

This PhD thesis has been developed at:

CIC-nanoGUNE (BRTA)
Self-Assembly Group
Donostia – San Sebastian, Spain

Materials Physics Center
Polymers and Soft Matter Group
Donostia – San Sebastian, Spain

University of Potsdam
Cell Membrane Biophysics Group –
Physikalische Biochemie
Potsdam – Golm, Germany

Fritz Haber Institute of the
Max Planck Society
Nonlinear Spectro-electrochemistry Group
Berlin, Germany

The international research visits performed during this PhD thesis have been awarded by:

European Molecular Biology Organization
Short-Term Fellowship 2019
Grant number 8397

German Academic Exchange Service
Research Grants – Short-Term Grants 2020
Grant number 57507442

"A man of wisdom delights in water"

Confucius (Analects ch. 6, v. 21)

Abstract

Water, the most abundant molecule in our planet, is truly and empirically accepted as an essential component to sustain life on Earth. The extraordinary properties of this unique and universal "matrix of life" have served over this quarter century, as the driving force – for theoreticians and experimentalists – to perform novel research on the structural basis and molecular dynamics taking place in very different environments. Even today, scientists are still discovering new phenomena in water, especially at the nanoscale.

When referred to bio-systems, water is usually seen as the liquid environment – or "matrix" – where physical and chemical processes take place. Here, the molecules of life are thought of being wet – this is, completely immersed in liquid water or, in other words, in fully hydrated conditions. While this is true for most living cells, a surprising number of processes require merely traces of water, which could be vapor or a layer as thin as nanometers. Indeed, this is observed in situations in which, because of extremes of either heat or cold, liquid water is scarce. Here, the hydration layer of the molecules – understood as an entity that differs from bulk water – should confer certain stability to keep the biomolecules still functional; and the processes taking place at the air interface should play a prominent role.

In this direction, the transmission of many airborne viruses – through respiratory droplets (e.g. aerosols) – requires, actually, survival in dry conditions. Influenza A virus (IAV), is one of the best-known cases, for which the transmission and thus survival is tightly connected to seasonal factors. Seasonal epidemics generally occur during winter, when air temperature and humidity are low. Under these conditions, the respiratory droplets must confer some structural stability to the contained viruses; membrane collapse, for example, should be in principle avoided. However, this assumption is yet poorly understood and experimental data based on biophysical methods are in great demand to obtain a solid knowledge base for the restriction of virus transmission (in addition to vaccination strategies).

This thesis represents the outcome of almost four years of intensive work in the field of applied biophysics in life sciences. Here, we explore the possibilities to mimic IAV by different model systems, by mostly focusing on the role of hydration water under various relative humidity (RH) conditions, namely hydration scenarios. To date, RH has been one of the less investigated and one of the most controversial environmental factors. Its effect on the transmission, survival and stability of the virus is still under debate, while the influence of air temperature, e.g., is quite well established.

In this research, the structure of the IAV envelope is studied in a range of model systems and by a combination of very different techniques, providing new biophysical insights on the micro- and nanoscale, from dehydrated to fully hydrated conditions.

To this aim, in **Chapter 1**, an overview on the scope of this investigation is provided. Here, we include an introduction to the science of hydration as well as information on the

IAV structure and seasonality. Finally, a detailed description on the developed model systems is offered.

In **Chapter 2**, all the experimental techniques used in this research are described and specific considerations for performing the experiments are noted.

In **Chapter 3**, we introduce the first approximation for mimicking the IAV surface "spike" glycoproteins (e.g. hemagglutinin, HA), by the use of dimannoside-coated gold nanoparticles (*Dimanno*-AuNPs). In this research, unprecedented observations on the stability and hydration water of the particles are provided in solution – by Dynamic Light Scattering (DLS) and Zeta Potential (ZP) measurements – and after dehydration – by a combination of Vibrational Sum Frequency Generation Spectroscopy (VSFG), Fourier Transform Infrared Spectroscopy (FT-IR) and Electron Microscopy. The study culminates with the analysis on the water adsorption of the particles at various RH, by Atomic Force Microscopy (AFM). Here, the hydration properties of mannosides in air, from dehydrated states to high humidity are demonstrated.

In **Chapter 4**, a supported lipid bilayer, with HA anchored at high surface density is proposed as a "flattened" and simplified model of the IAV envelope. The effect of RH is investigated, in complete cycles of hydration, dehydration and rehydration. The membrane performance is evaluated in terms of structure and dynamics, by combining Confocal Fluorescence Microscopy, Raster Image Correlation Spectroscopy (RICS), Line-Scan Fluorescence Correlation Spectroscopy (LSFCS) and AFM. The macro- and nanoscopic effects of HA under dehydration stress are studied in detail, revealing new information on the stabilization mechanisms operating in the IAV envelope at low RH.

In **Chapter 5**, the use of a monovalent live attenuated Influenza vaccine (LAIV) as a more realistic model of the IAV envelope is explored. Here, revealing the morphological features of the IAV envelope is attempted by performing AFM on solid surfaces in air. Although the detailed surface structure of the virus is not revealed, complete assembled viruses are identified after dehydration, suggesting that adsorbed LAIV can be used as an analogous model of the IAV envelope during airborne transmission.

Finally, **Chapter 6** contains concluding remarks for the studies presented in this thesis, and an outlook to further investigations.

Resumen

Siendo el líquido más abundante en nuestro planeta, el agua, constituye sin lugar a dudas el componente esencial para que el desarrollo de la vida en la Tierra sea posible. Ciertamente, donde encontremos agua, habrá vida, o al menos eso hemos aprendido. Las extraordinarias propiedades de esta "matriz de la vida" – única y universal en sus características – han servido durante este último cuarto de siglo, como piedra angular para el desarrollo de investigaciones nóveles en términos de estructura y dinámica del agua. Incluso actualmente, gracias a la investigación multidisciplinaria y complementaria de teóricos y experimentalistas, nuevos fenómenos continúan descubriéndose, especialmente en la nanoescala y a nivel molecular.

Considerando los sistemas biológicos, el agua suele ser percibida como el medio líquido – o "matriz" – donde ocurren la mayoría de los procesos físicos y químicos a nivel celular. Para ser precisos, se considera que las biomoléculas se encuentran completamente sumergidas en el medio acuoso o, en otras palabras, en condiciones de hidratación total. Si bien esto es cierto para la mayoría de las células, existen procesos que requieren pocas trazas de agua, desde capas nanométricas de hidratación, hasta incluso simplemente vapor. Esto es cierto en situaciones extremas de calor o frío donde el agua líquida generalmente escasea. En estos casos, la capa de hidratación de las biomoléculas – entendida como una entidad distinta del agua de "bulk" – y los procesos asociados en la interface con el aire, deberían conferirles algún tipo de estabilidad, garantizando así la conocida relación entre estructura y función.

En este contexto, muchos virus de trasmisión aérea necesitan sobrevivir en entornos extremadamente secos para lograr una trasmisión efectiva a través de gotas respiratorias (como los aerosoles). Para ser exactos, el virus de la Influenza A (comúnmente conocido como virus de la gripe A) es uno de los casos más conocidos y estudiados. Tanto la trasmisión como la supervivencia del virus está estrechamente relacionada a factores ambientales. Los brotes estacionales ocurren generalmente durante el invierno, donde la temperatura y la humedad del aire son bajas. En estas condiciones, las gotas respiratorias deberían cumplir un rol primordial en mantener la estructura a los virus que contienen; evitando así, por ejemplo, el colapso de la membrana y desintegración del virus. Sin embargo, esto supone una mera interpretación ya que, hasta la fecha, se han desarrollado pocos estudios en materia de hidratación del virus. En este sentido, estudios basados en métodos biofísicos resultan esenciales; no solo para obtener una base de conocimiento sólida en la materia si no para diseñar estrategias efectivas en la prevención de la transmisión del virus.

Esta tesis representa casi cuatro años de intenso trabajo en el campo de la biofísica aplicada a las ciencias de la vida y desafía entender la estabilidad del virus de la Influenza A en distintas humedades. Aquí, exploramos las posibilidades de imitar la estructura externa del virus a través de sistemas modelo, centrándonos en el rol del agua de

hidratación en distintas humedades relativas. Mediante la aplicación y combinación de técnicas diferentes, logramos caracterizarlos desde una perspectiva biofísica en la micro y nanoescala, desde condiciones de deshidratación hasta condiciones de hidratación total. Hasta la fecha, la humedad relativa ha sido uno de los factores ambientales menos investigados y más controversiales. Su efecto sobre la transmisión, supervivencia y estabilidad del virus sigue siendo objeto de debate, mientras que la influencia de la temperatura del aire, por ejemplo, se encuentra ampliamente establecida.

En el **Capítulo 1** se desarrolla el alcance de esta investigación. Además se introducen conceptos como la hidratación, la estructura y estacionalidad del virus de la gripe y se describen detalladamente los modelos experimentales diseñados.

En el **Capítulo 2**, se describen todas las técnicas experimentales utilizadas, considerando puntos específicos para los estudios desarrollados en los capítulos posteriores.

En el **Capítulo 3**, se presenta la primera aproximación a la estructura externa del virus de la Influenza A. El empleo de nanopartículas de oro recubiertas de dimanósidos (*Dimanno*-AuNPs) supone la emulación de las glicoproteínas de superficie del virus (por ejemplo, la hemaglutinina, HA). Aquí, se estudia la estabilidad de las partículas junto con el agua de hidratación en solución y luego de su deshidratación. En el primer caso, se emplean técnicas de Dispersión de Luz Dinámica (DLS) y de Potencial Zeta (ZP), mientras que en el segundo, se combinan la Espectroscopia de Generación de Frecuencias de Suma Vibracional (VSFG), Espectroscopia Infrarroja por Transformada de Fourier (FT-IR) y Microscopía Electrónica. El estudio culmina con el análisis de la adsorción de agua en la superficie de las partículas mediante Microscopía de Fuerza Atómica (AFM). En esta investigación se demuestran las propiedades de hidratación de los manósidos en el aire, a distintas humedades relativas, desde estados deshidratados – o baja humedad – hasta condiciones de alta humedad.

En el **Capítulo 4**, se propone el uso de una bicapa lipídica sintetizada sobre un soporte sólido, con la HA anclada a alta densidad superficial. En consecuencia, se propone un modelo plano y simplificado de la envoltura del virus, el cual se investiga en ciclos de hidratación, deshidratación y rehidratación. El rendimiento de la bicapa se evalúa en términos de estructura y dinámica, mediante la combinación de Microscopía de Fluorescencia Confocal, Espectroscopia de Correlación de Imágenes de Barrido de Trama (RICS), Espectroscopia de Correlación de Fluorescencia de Barrido de Línea (LSFCS) y AFM. En este estudio, se revela el efecto de la HA en la preservación de la bicapa lipídica en condiciones de deshidratación a baja humedad relativa, desde un análisis en la macro y nanoescala.

En el **Capítulo 5**, se explora el uso de una vacuna viva atenuada contra la Influenza (LAIV) fisisorbida a superficies sólidas, como modelo más realista y aproximado de la estructura externa del virus. El objetivo es revelar sus características morfológicas mediante AFM en aire y a pesar de que no se revelan resultados al detalle, es posible identificar virus completamente íntegros una vez deshidratados. Esto sugiere que el uso

de una LAIV adsorbida a una superficie plana, puede considerarse como modelo análogo del virus durante su transmisión en aire.

Por último, el **Capítulo 6** contiene observaciones finales sobre los estudios presentados en esta tesis y plantea perspectivas para futuras investigaciones.

Contents

1. Introduction **1**
1.1 The science of hydration 2
1.2 Influenza virus 4
1.2.1 Influenza virus structure 5
1.2.2 Influenza A virus (IAV) transmission and seasonality 7
1.3 Model systems 10
1.3.1 Dimannoside-coated gold nanoparticles adsorbed on modified surfaces 10
1.3.2 Supported lipid bilayers (SLBs) with incorporated hemagglutinin (HA) 13
1.3.3 Live attenuated Influenza vaccines (LAIVs) 14
1.4 Objectives 15

2. Methodology **17**
2.1 Contact angle 18
2.2 Dynamic Light Scattering (DLS) 19
2.3 Zeta Potential (ZP) 21
2.4 Sodium Dodecyl Sulfate Polyacrylamide Gel Electrophoresis (SDS-PAGE) 22
2.5 Fourier Transform Infrared Spectroscopy (FT-IR) 23
2.6 Vibrational Sum Frequency Generation Spectroscopy (VSFG) 25
2.7 Scanning Electron Microscopy (SEM) 26
2.8 Fluorescence Microscopy 27
2.8.1 Advanced quantitative Fluorescence Microscopy 29
2.9 Atomic Force Microscopy (AFM) 32

3. Humidity effects on glycosylated gold nanoparticles **39**
3.1 Introduction 40
3.2 Materials and methods 41
3.2.1 Materials 41

3.2.2 Synthesis of nanoparticles ... 42
3.2.3 DLS and ZP measurements ... 43
3.2.4 Preparation of hydrophilic and hydrophobic substrates ... 43
3.2.5 Contact angle measurements ... 44
3.2.6 Adsorption of nanoparticles ... 44
3.2.7 FT-IR measurements ... 44
3.2.8 VSFG measurements ... 45
3.2.9 Electron Microscopy imaging ... 45
3.2.10 AFM measurements ... 46
3.2.11 Statistical analysis ... 47
3.3 Results ... 47
3.3.1 Analysis of the chemical groups ... 47
3.3.2 Particle size and shape ... 51
3.3.3 Adsorption on hydrophilic and hydrophobic substrates ... 54
3.3.4 AFM scanning in water vapor ... 57
3.4 Discussion ... 64
3.5 Conclusions ... 67

4. Investigating the protective effects of Influenza A virus hemagglutinin against dehydration ... 68
4.1 Introduction ... 69
4.2 Materials and methods ... 70
4.2.1 Materials ... 70
4.2.2 SDS-PAGE ... 71
4.2.3 Fluorescence labeling ... 71
4.2.4 Preparation of SLBs ... 72
4.2.5 Protein binding to the SLBs ... 72
4.2.6 Sample dehydration and rehydration ... 72
4.2.7 Fluorescence Microscopy ... 73

4.2.8 AFM measurements ... 74
4.2.9 Statistical analysis ... 76
4.3 Results ... 76
4.3.1 Fluorescence Microscopy and Raster Image Correlation Spectroscopy (RICS) measurements on SLBs after dehydration-rehydration cycles ... 76
4.3.2 Fluorescence Microscopy and RICS measurements of proteins on SLBs after dehydration-rehydration cycles ... 82
4.3.3 Line-Scan Fluorescence Correlation Spectroscopy (LSFCS) measurements of HA on SLBs after dehydration-rehydration cycles ... 85
4.3.4 AFM scanning in water vapor ... 88
4.4 Discussion ... 94
4.5 Conclusions ... 97

5. Examining the surface structure of Influenza A virus in air ... 99
5.1. Introduction ... 100
5.2. Materials and methods ... 101
5.2.1 Materials ... 101
5.2.2 Sample preparation ... 101
5.2.3 Contact angle measurements ... 101
5.2.4 AFM measurements ... 102
5.3. Results ... 102
5.3.1. LAIV adsorbed on flat substrates ... 102
5.3.2. IAV envelope morphology ... 106
5.4. Discussion ... 107
5.5. Conclusions ... 109

6. Conclusions and outlook ... 110

Acknowledgements ... 113

List of Publications **114**

References **115**

Chapter 1

Introduction

Almost 25 years ago, Albert Lehninger wrote a famous science book called *Principles of Biochemistry* [1] which has served to me and also to most students in the field as the first encounter with biochemistry and biophysics. In this quarter century, the world of life sciences has enormously changed and despite the torrent of new information and discoveries, water has always been considered as one of the most incredible phenomena on Earth. In this text, water is referred as a determining factor of evolution: "*The first living organisms on Earth doubtless arose in an aqueous environment, and the course of evolution has been shaped by the properties of the aqueous medium in which life began*". Water is the natural medium for most biomolecules and has a significant influence on their dynamics, stability, and function. Water is life and is science. In agreement with Leonardo da Vinci, there are no doubts this thesis is inspired by "*the driving force of nature*".

Considering living organisms, the survival mechanisms and transmission rates of pathogens in different environments are influenced by water. For instance, respiratory viral diseases are not only transmitted by direct or indirect contact between the infected host and the susceptible host but also through droplets. This includes respiratory droplets in the micrometer range and aerosols that are smaller in size [2]. Among several factors – as human behavior or host defense, that are not in the scope of this investigation – seasonal environmental conditions modulate and affect these transmission routes. With special focus in aerosols – which contain few water layers – the viruses inside these droplets must survive in the environment to cause infection in new hosts. Therefore, seasonal fluctuations in i.e. temperature, humidity or sunlight will affect the survival and viability of the viruses [2] [3].

Influenza A virus (IAV), with its seasonal epidemics, is one of the remarkable cases in which the link to humid air – not only with liquid water – is indeed proven [4] [5]. Both virus survival and transmission are heavily dependent on humidity. For instance, in cold weather, where the humidity is low, the survival of the virus is favored, while in the humid tropical regions outbreaks follow no seasonal pattern. The virus must be able to maintain its integrity in quite variable conditions, but possible structural changes of the virus surface are not known. The connection between the virus structure and water (i.e. in aerosols) is not a trivial task, and requires to be addressed from a biophysical point of view.

IAV possesses various challenges, such as its seasonal nature, its extreme spread, and its high absolute number of fatalities. Governments worldwide have struggled with support measures, specifically vaccination campaigns, but a basic understanding of IAV transmission mechanisms was not in the focus. Even basics such as the presumed contact transmission, are still debated and even doubted [3]. The nature of the usually proposed infective aerosols is unknown, except that virus material must be present in some form [6].

In order to battle virus pandemics by curbing transmission pathways, a solid scientific base is highly desirable, but it does not yet exist, not even for well-known viruses. Hence, there is a huge need for understanding transmission based on physics, not replacing, but complementing the very detailed biochemical information, which is based on structural biology methods. Regarding seasonality, the detailed influence of environmental factors on virus biophysics requires to be further addressed. Low temperature should, in general, preserve the virus better, but the detailed interactions between water and the molecular components of the enveloped virus (specifically, in the case of low water amounts, as encountered in winter in temperate climates) are still beyond our understanding. This is also limited by the available techniques to study the adsorption of water at the nanoscale.

In this thesis, the structure of IAV surface envelope is studied in different hydration scenarios by using various model systems, from simple approaches to more complex compositions. Among others, the preferred technique is Atomic Force Microscopy (AFM), providing detailed information of the surface structure of the model systems at the air interface.

1.1 THE SCIENCE OF HYDRATION

Studying the interplay between bio-systems and water has answered several fundamental questions in life sciences from multidisciplinary approaches as physics, chemistry, and biology. For instance, it is now commonly accepted that hydrophobic interactions are involved in protein folding [7], or that water mediates the transmission of information into the cell [8] [9]. However, most questions involving in what way the dynamics of biomolecules are influenced by water, or how many water layers are necessary for structuring the molecules of life are still beyond our understanding.

In aqueous environments, biomolecules are in contact with bulk water, and their structure (usually only their conformation) is influenced by the adsorption of a few water layers on the external surface, known as hydration layer or shell. In bulk water, structural fluctuations and molecular excitations occur on femto- to picoseconds, while processes associated with the hydration layer require larger time scales, stretching from micro- to femtoseconds [10] [11]. The most relevant interactions are the short-range hydrogen bonds, but also the long-range Coulomb forces can play a role, as also the hydrophobic effect and Van der Waals forces.

Water in hydration layers provides a hydration structure with a network of hydrogen bonds covering the biomolecule's surface. Because most of the ordered water molecules are found to interact with the biomolecules (i.e. proteins) [12], the spatial arrangement of water in the first hydration layer is different from the bulk. The resolution of structural methods is aimed at the range of nanometers, for the thickness of the layers, but also for their lateral extension. Moving from the first water layer to larger distances from the biomolecular surface, the hydration shell gradually assumes the bulk water structure. The length scale is controversial, but usually between 2 and more than 10 water layers are involved. Considering the thickness of a hydration layer (~ 0.6 nm) [13] [14], this represents between 1.2 nm and 6 nm water layer thickness. Below this threshold, water is usually considered as part of hydration layer.

In this regard, the hydration layer of objects, specifically of biological structures, is generally associated with liquid environments. However, since several hundred million years, the interface with air on i.e. membranes and more complex systems, such as skin, is decisive for life on earth. So water plays an important role also when an object is dry, or when its hydration layer is in contact with (humid) air.

Air contains water vapor ranging from 0 % to 100 %, relevant to saturation (at 100 %), given by the temperature-dependent saturation vapor pressure of water. At relative humidity above 100 %, water condensates on any surface, and at 0 % the situation is that of completely dry (dehydrated) environments. Although the regime in between is often neglected, depending on the exact atmospheric conditions (driven by e.g. temperature and humidity) many states of hydration exist on external biological surfaces. For instance, humidity is one of the factors that determine the efficacy of airborne spreading of IAV [15] and, along with evaporation (and other factors as well) influence the size of a droplet and its decrease of diameter in dry air [16]. In this sense, the interface of a virus-containing droplet with air determines a successful transmission (together with the survival time).

Currently, the properties of hydration layers at the interface of solids with air are little known. This is also true for complex "biosurfaces", such as protein layers or lipid bilayers. There is practically no date on more complex surfaces, e.g. of curved geometry (virus particles), or of composite nature (all real biosurfaces). This is due, in part, to the lack of suitable methods for its investigation in varying humidity conditions. Therefore, it is essential to have study models that allow the adequate characterization of hydration layers in biological systems and, in turn, work with techniques that encompass spatial resolutions in the nanometer range. The analysis, in this case, allows to elucidate not only the thickness of the confined water layers, but also their lateral extension. Thus, the nanoscale properties provide new insights on the effects of water on the macroscopic scale.

1.2 INFLUENZA VIRUS

"*Viruses are viruses*" is one the simplest but paradoxical ways A. Lwoff used in 1957 to define the complex but amazing nature of viruses [17]. These masterpiece biological assemblies are generally defined as "*replicators that encode structural proteins encasing their own genomes*" [18]. This recently introduced definition by E.V. Koonin et al., extends to much larger volumes of the "virosphere", e.g. viruses that infect viruses.

Viruses are robust enough to protect the viral genome outside the cell, but some are poised to undergo structural changes and execute mechanochemical actions required for infection of other cells [19]. Viruses are abundant (recent studies found huge numbers and a large number of species in sea water), ubiquitous (in plants, animals, bacteria, archaea, in dry climates, in the tropics, even inside sea ice), and played a prominent role in the evolution of life [18].

From a structural point of view, virions (infective virus particles) include a nucleic acid genome and many copies of one or more proteins. According to the molecular composition, they can be classified in non-enveloped viruses and enveloped viruses.

Non-enveloped viruses do not possess an outer lipid layer but a protein shell, the capsid. Inside the capsid, the viral genome is confined, as well as – usually – other proteins or macromolecules. Although the composition and the arrangement of the capsid can be complex and dynamic, only few types of capsid symmetry are frequent, namely helical (tubular), or icosahedral (nearly spherical) architectures [20]. This minimalistic and highly symmetric architectures might be essential for genome protection, viral infection and replication [21].

In enveloped viruses, the capsid and/or other internal structures are surrounded by an outer lipid bilayer, or envelope, in which the proteins are embedded. Contrary to the well-ordered arrangement of the capsids, most enveloped viruses lack regular organization in the membrane [19]. Strictly speaking, all enveloped viruses are pleomorphic (each virion has a unique shape); more practically, the overall shape can be nearly spherical and almost identical for each virion, but also very irregular.

Influenza virus is a type of enveloped virus that belongs to the *Orthomyxoviridae* family. This family of viruses have negative-sense, single stranded ribonucleic acid (RNA). The genome is segmented into RNA strands, and is bound to nucleoproteins, arranged in helical symmetry, thus forming the ribonucleoprotein (RNP) complex. The inner surface of the envelope is lined with the matrix protein M1. The envelope itself is derived from lipids of the membrane of the cell, in which the virus was synthesized. It also incorporates furthermore virus surface proteins.

Lipids in the virion envelope constitute about 18 – 37 % of the particle weight, while carbohydrates in the form of glycolipids and N-glycosidic side chains of glycoproteins constitute about 5% of the particle weight [22]. The remainder is distributed between proteins, RNA, and water.

The family *Orthomyxoviridae* contains Influenza virus genera A; B (IBV), and C (ICV). IAV and IBV share similarities on the virus structure and genome, while ICV exhibits substantial differences that will not be further detailed. In non-aqueous environments, the natural transmission of IAV, IBV and ICV is by aerosols [23], but also droplet transmission [24]. Contact transmission (i.e. through fomites) is to date, less evident (**section 1.2.2**)

IAV infects humans and a range of mammalians (pigs and horses) as well as avian species. IBV and ICV are restricted to humans, although ICV may also infect pigs. Despite that only types A and B cause human diseases of high concern, IAVs are the main cause of large epidemics and pandemics with high mortality. According to the World Health Organization (WHO): *"Worldwide, these annual epidemics are estimated to result in about 3 to 5 million cases of severe illness, and about 290 000 to 650 000 respiratory deaths"* [25].

1.2.1 *Influenza virus structure*

Influenza virions are pleomorphic. During transmission, they are roughly spherical, 80–120 nm in diameter. They can also be found in filamentous forms, sometimes up to several micrometers in length, e.g., on lung tissue, just before infection. The lipid envelope is derived from the plasma membrane of the cell in which the virus replicates and is acquired by a budding process as one of the last steps of virus assembly [22].

The virus genomes on IAV and IBV types comprise eight negative-sense, single-stranded viral RNA segments. Segments four and six encode two major virus surface glycoproteins, the trimeric hemagglutinin (HA), and the tetrameric neuraminidase (NA). Both HA and NA extend radially from the membrane with an average center-to-center spacing of 11 nm. They are anchored on the membrane by a stem that terminates in a globular domain. The projection of HA from the membrane is lower than NA, 14 nm versus 16 nm, respectively. The shape also varies, being the first referred as a "peanut-like" shape while the second to a "mushroom-like" shape [26]. The HA is a homotrimer, built from non-covalently linked protein subunits anchored in the viral membrane. The mature state of each subunit consists of two proteins, named as HA1 and HA2 that interact through disulfide bonds. HA1 is known to form the globular domain while HA2 builds the stem domain [27]. To date, 18 structural variants of HA and 11 variants of NA have been identified on IAV [28]. Thus, IAV subtypes are described by HA and NA designations and labeled with numbers, e.g., H1N1 or H5N7.

The surface glycans of HA and NA are important for modulating recognition of glycoproteins by the adaptive immune system and interact with the innate immune response. For instance, terminal mannose residues are features of Influenza virus HA and NA, but are not typically found on human glycoproteins [28]. Glycosylation is also important for the folding and stability, and provides viral fitness [29]. HA and NA can contain a mixture of high-mannose (branched structures terminating in the glycan mannose), complex (branched structures terminating in galactose and/or N-acetyl-

galactosamine (GalNAc) or hybrid-type oligosaccharides [30]. In general, human HAs exhibit significant oligomannose-type glycans with minimal processing [33].

Surface glycans in HA are related to antigen recognition and receptor binding. HA1 subunits recognize sialylated sequences of the host cell and bind to specific receptors that possess terminal N-acetylneuraminic acid (Neu5Ac or sialic acid, SA), particularly on epithelial cells and mucins of human respiratory tracts [28]. The acquisition of N-glycans within the globular domain, can mask or modify antigenic sites recognized by neutralizing antibodies. The HA2 subunits are responsible for mediating pH-dependent fusion process for internalization into the cell. They exhibit extensive processing of glycans from a high-mannose to complex-type, which are critical for folding and conformation of the HA molecule. As with HA, also NA has specificity for terminal SA. NA has a receptor-destroying and cleavage activity; it prevents virus agglomeration and enables their release from the infected cells [27] [30] [31] [32].

The patterns of glycosylation are temporal and dynamic. For instance, HA exhibits highly conserved glycans in the stem domain, but undergoes dramatic glycosylation modifications in the globular domain, resulting in the loss or gain of surface glycans.

The glycan composition also depends on the HA subtype. Highly branched glycans have been reported for H1, while simpler glycans have been connected to H3. The maximum glycan mass added to the H1 globular domain is ~ 16.5 kDa, and for H3 ~ 17.5 kDa per monomer (~ 75 kDa). This represents four glycans for H1 and five glycans for H3 [30].

The viral envelope of IAV is also associated with a matrix protein 2 channel (M2) that after infection forms tetrameric ion channels that traverse the lipid envelope [31]. M2 acts as a proton channel activated by acidic pH and its functions are related to genome unpacking during virus entry, virus morphology, production of infectious virus particles, and membrane scission. In terms of numbers, the virus envelope contains around 300 - 400 copies of HA, 50 copies of NA and approximately 16 - 20 M2 molecules [32] (**Figure 1.1**). The organization of the IBV is similar, with four envelope proteins: HA, NA, and, instead of M2,NB and BM2 [31]. In contrast with IAVs, IBVs do not have subtypes of HA and NA.

Inside the lipid envelope, the virion core is protected by the matrix protein 1 (M1), which is the most abundant protein in virus particles. M1 stabilizes the virion structure and is considered to be a determinant of viral morphology [33]. The M1 matrix encloses the nuclear export protein (NEP) and the RNP complex. The RNP complex includes the viral RNA segments coated with nucleoprotein (NP) and the heterotrimeric RNA-dependent RNA polymerase. The subunits in the polymerase consist of two "polymerase basic" and one "polymerase acidic" subunits (PB1, PB2, and PA). From now on, any details of the core will be deliberately neglected, the focus will be solely on the external virion surface.

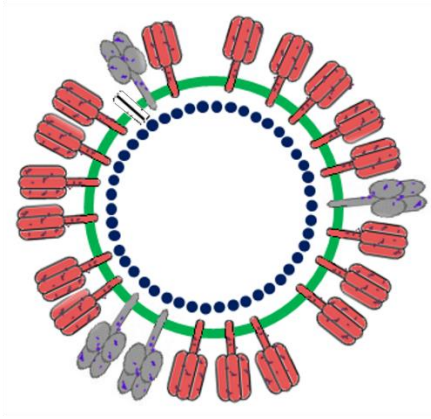

Figure 1.1. Influenza A virus (IAV) external structure. Representative scheme of the main components of IAV envelope. From inside to outside: The dark blue circles represent the matrix protein 1 (M1), the big green circle represents the lipid membrane, the white barrel-like structure represents the matrix protein 2 channel (M2), the grey mushroom-like structures represent neuraminidase (NA), the red peanut-like shape structures represent the hemagglutinin (HA). Note that empty spaces on the membrane indicate some disorder on the envelope. Small circles on HA and NA represent glycosylation sites. For simplicity, the components of the virus genome are not shown.

As mentioned above, virus infection starts by the attachment of the HA protein on the host cell. After binding, the virus enters by endocytosis. The acidity of the endosomal compartment induces a conformational change in HA and enables the M2 channel to provide internal acidification to the virion. As a consequence, RNPs are released from the viral matrix into the cellular cytoplasm. Further steps include RNA replication and synthesis of viral proteins; full genome RNA packing and finally virus budding and release, which involves NA activity [34] [35]. In all these processes, the viruses are completely immersed in aqueous media (body fluids). From a physical interpretation, water is in the liquid state, and the humidity at any surface in the system is 100 %.

1.2.2 *Influenza A virus (IAV) transmission and seasonality*

IAV transmission is generally classified in three main mechanisms: aerosol transmission, droplet transmission and contact transmission [3].

In aerosol transmission, small droplet particles (diameter < 5 μm) are capable of reaching the lower respiratory tract as well as depositing on the upper respiratory tract of the susceptible host after being inhaled. The small size of these droplets may confer

biophysical advantages during airborne transmission. Indeed, there is growing evidence on aerosols as the preferred route of transmission of IAV [3].

In droplet transmission, large respiratory droplets (diameter > 10 μm) deposit on the mucous surfaces of the upper respiratory tract (e.g. mouth and nose) but are not capable of reaching the lungs. These droplets evaporate rather slowly, fall to the ground rapidly, and hence cannot form aerosols sufficiently fast. Although droplet transmission is accepted as a transmission pathway, the constraining factors previously mentioned have led to consider it as a rare event [3].

In contact transmission, the particles are directly or indirectly transferred to the mucous membranes of the upper respiratory tract. This includes fomites (surfaces that preserve infective virus particles) or direct contact from the infected host and the susceptible host. Contact might be considered as a potential mechanism of transmission; yet, no direct evidence has shown, so far, that this actually occurs [3].

Transmission routes are influenced by the stability of the IAV outside the host cell under environmental stress. This is, the composition and structure of the envelope, capsid, internal proteins and genomes as well as the formation of viral aggregates influence the success on virus transmission [24]. Also, one of the main characteristics of IAV infections is their seasonality, i.e. outbreaks follow largely predictable seasonal patterns [2]. According to the WHO: "*In temperate climates, seasonal epidemics occur mainly during winter, while in tropical regions, influenza may occur throughout the year, causing outbreaks more irregularly*" [25]. However, the data show that the non-seasonal area extends also to the Northern subtropical regions; the Southern hemisphere has a less clear seasonal pattern than the Northern hemisphere [4].

The seasonality can have various origins: Epidemics are very much dependent on human behavior, such as indoors crowding in winter, but in addition there are purely physical effects that determine transmission. In terms of environmental stress, IAV transmission has been associated with environmental factors as temperature, ultraviolet light (UV) or humidity [36] [37] [4], all of which affect the composition and stability of the virions. Rather obvious is the temperature – virions survive better at lower temperature. This must be based on generally lower chemical reaction rates at low temperatures. Another obvious effect is the decreased survival in UV light [38]. In contrast, the link between humidity and virus transmission has been experimentally poorly developed.

The first attempts to understand the connection between humidity and IAV seasonality date to the nineteen seventies. G.J. Harper originally studied the relative humidity (RH) as a determining factor on the viability of IAV. His research provided remarkable evidence on IAV viabilities after spraying of aerosols, based on the ratio of virus titration to radioactive count, in suspension and cloud samples. The main findings pointed to ~ 10-fold higher viability of the virus below 35 % RH with respect to RH above 50 % after e.g., 6 hours of aerosol spraying, at controlled temperatures (21 - 24 °C) [36].

Back to the nineties, direct evidence on the size distribution of respiratory droplets was achieved by R.S. Papineni and F.S Rosenthal. Using an Analytical Transmission Electron Microscope, respiratory aerosols in the range of 0.6 μm were resolved in detail after dehydration. Although this research was only performed with healthy patients, the heterogeneous composition of the aerosols after dehydration resulted in one of the first attempts to understand – by microscopy observation – the airborne transmission of viruses from a biophysical approach [6].

During the last two decades, molecular knowledge on virus survival and stability has been bolstered. A progressive ordering with decreasing temperature for IAV lipids was found by Nuclear Magnetic Resonance [39] and molecular simulations on the IAV envelope concluded that the presence of the Forssman glycolipid – the most abundant sphingolipid in the virus – is likely to confer physical robustness to changes in environmental conditions [40]. Both investigations offer new evidence on the biophysical advantages of the IAV envelope in harsh conditions, though the effect of humidity on the virus stability has been surprisingly neglected.

Great contributions on the physicochemical characteristics of respiratory droplets at various RH have been performed by L.C. Marr et al., [41] [5] [42] [43]. Of note, studies on Φ6 viruses as analogous systems of IAVs have proven the virus stability and homogenous distribution on model respiratory droplets upon dehydration stress. Although the authors suggest that the droplet components may inactivate the virus upon dehydration (i.e. due to the increased concentration of salts), the results provide a novel assessment on the physicochemical characteristics of respiratory droplets at different RH and thus, the potential connection to virus transmission [5]. A follow-up from this investigation has proven that the infectivity of IAVs is retained in a wide range of RH, thus suggesting that dehydration may not inactivate the virus [42]. From these data, one could assume that inside the infected host, the respiratory droplets are at complete hydration where the RH is 100 %. During transmission the hydration state of the droplets changes substantially, even though IAVs might be still viable and stable (**Figure 1.2**). Yet, the molecular mechanisms involved in these processes are far beyond our understanding.

Nowadays, research is oriented to address whether absolute humidity (AH) rather than RH modulates the virus survival and transmission [44]. Although great progress has been achieved in the field of big data and computational modeling analysis [45] [46] [47] [48], biophysical studies based on experimental approaches are still limited. In this context, despite that humidity is proposed to be one of the origins of the seasonal nature of IAV – i.e. by providing advantageous dry conditions during the winter – the physicochemical reason or mechanism remains unclear and controversial. This is equally true for most other viruses, and motivates a biophysics-based approach to IAV transmission.

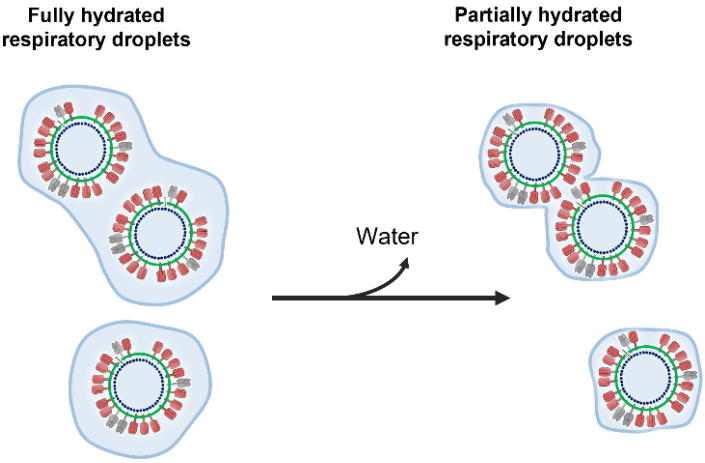

Figure 1.2. Possible structural changes of respiratory droplets during IAV transmission. Inside the body, immediately after their formation, the respiratory droplets are fully hydrated. During transmission the relative humidity (RH) may change the external structure of the droplets, possibly also the structure of the IAV, although they might be still viable and stable.

1.3 MODEL SYSTEMS

Model systems are attractive tools to gain more knowledge on processes that are central to life. Although we are unlikely to ever know everything about any organism we can design appropriate model systems to answer critical questions about their development in life. The general idea is to split complex processes or complex objects into smaller or simplified parts, whose investigation gives faster or easily interpretable results.

Regarding IAV transmission, understanding the seasonality from a biophysical interpretation requires consideration of virion (surface) chemistry, virion geometry, air temperature and air humidity, ideally varying all of them independently. The advantages of using model systems for chemistry and geometry lie in the simple handling. Prerequisites are size and composition that are comparable to the virion. Here, the focus is on the application of three model systems to study IAV envelope at various hydration scenarios. To this aim, different approaches were developed, from simplistic compositions to more complex structures.

1.3.1 *Dimannoside-coated gold nanoparticles adsorbed on modified surfaces*

This investigation starts with the use of dimannoside-coated gold nanoparticles (*Dimanno*-AuNPs) – a type of glyconanoparticles (GNPs) – as model systems of the surface

glycoprotein HA, which is highly covered in high-mannose residues, complex-type glycans as well as oligomannose-type molecules (**section 1.2.1**).

GNPs are water-soluble gold nanoclusters with a 3-dimensional carbohydrate display that are produced in solution and can be further adsorbed to different substrates [49]. The dimannosides emulate the mannose residues of HA and are covalently linked to the small gold cores. In this way, the particles mimic the size and also the surface composition of HA, but not the shape. The advantages remain in their uniform nanometric size, in the ability to generate relatively ordered and homogeneous surfaces, and in the possibility of characterization and comparison to other well-established GNPs systems.

In this model system the particles are adsorbed on modified flat substrates. Hence, the surfaces used here play a prominent role in understanding the molecular interactions between water and the model systems. A large number of strategies for modifying surfaces can be developed. Of interest, molecular self-assembly methods provide a simple and controlled route to modify surfaces from the nanoscale to macroscopic dimensions, by self-organization of the molecules in a straightforward manner [50] [51].

For the substrate surfaces, Self-Assembled Monolayers (SAMs) were used to build well-ordered monolayers, based on the interaction of the adsorbed molecules with the substrate, and on intermolecular interactions between the molecules [52]. In general, the molecules consist of a head group with specific affinity and selectivity to the surface; the linker chains exhibit intermolecular interactions (mainly of Van der Waals type), and the terminal functional groups determine the reactivity and hydrophilicity. By choosing particular functional groups, the properties at the air/film interface can be finely tuned.

Surface modification with SAMs not only provides specific functionalities and selectivity but also allows controlling the degradation processes induced by the high humidity environments. Indeed, organosilanes have attracted significant attention due to their capability to tailor surface properties, wetting or biocompatibility on many hydroxyl-covered surfaces (e.g. glass, oxidized silicon, inorganic oxides). In particular, monolayers made of long aliphatic chains present high stability and resistance to external perturbing conditions. Silanes have a hydrolysable group that reacts with surface hydroxyl groups resulting in Si-O-Si bonds with the surface. By capping with different terminal groups, the surface can be engineered to attract or repel water and the wetting behavior can be investigated from the nanoscale to the microscale (**Figure 1.3**).

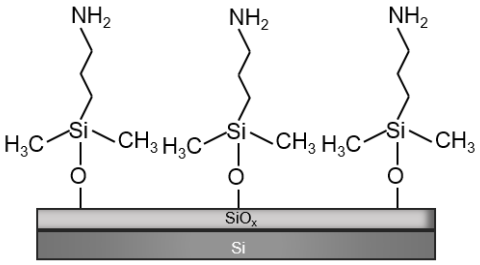

Figure 1.3. Self-Assembled Monolayers (SAMs) on silicon substrates. Representative scheme of a silane (3-(ethoxydimethylsilyl) propylamine, APDMES) adsorbed on oxidized silicon (SiO_2) by forming Si-O-Si bonds.

Our first model system consisted of *Dimanno*-AuNPs adsorbed on modified silicon surfaces by using organosilanes. The surface properties of silicon were changed by means of charge and hydrophilicity, allowing to create hydrophobic and hydrophilic air-stable substrates (**Figure 1.4**). The combined results allow to distinguish water adsorption on the GNPs from water adsorption on the substrate.

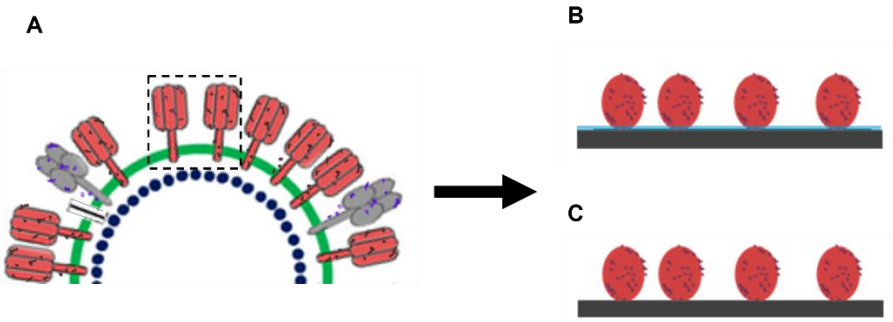

Figure 1.4. Dimannoside-coated gold nanoparticles (*Dimanno*-AuNPs) adsorbed on modified surfaces as flat model systems of the IAV envelope. (A) IAV envelope structure. (B) *Dimanno*-AuNPs adsorbed on a hydrophilic silicon substrate. (C) *Dimanno*-AuNPs adsorbed on a hydrophobic silicon substrate. In (A) the dark blue circles represent the M1 protein, the big green semi-circle represents the lipid membrane, the white barrel-like structure represents M2 channel, the grey mushroom-like structures represent NA, the red peanut-like shape structures represent the HA. In (B) and (C) the red spheres represent the AuNPs, the dark red small circles represent the dimannose residues and the grey rectangles represent the modified silicon substrates. Note that in (A-C) both HA and *Dimanno*-AuNPs have similar size and are glycosylated. In (B) the substrate is covered by a thin layer of water.

1.3.2 *Supported lipid bilayers (SLBs) with incorporated hemagglutinin (HA)*

The second model are self-assembled SLBs with densely packed HA. This is an attractive alternative strategy to study the effects of humidity on the structure and dynamics of the complex IAV envelope from a more realistic approach, again in a convenient flat geometry.

SLBs consist of a lipid bilayer made of phospholipids adsorbed on the surface of a solid substrate, such as glass or mica. Due to the amphiphilic nature of the phospholipids, in aqueous solutions, the hydrophilic, polar head groups of the molecules interact with the environment while the hydrophobic core of alkyl chains is protected mainly through the hydrophobic and intermolecular Van der Waals interactions [53] [54]. The formation of a bilayer provides self-organized, adaptable and structured membranes in liquids [50] [51]. The synthesis involves the creation of an inner leaflet in which the head groups are in close contact with the support by a thin layer of water in between (< 2 nm). Here, the lipids are not fixed but mobile, allowing lateral mobilities comparable to the upper leaflet, which is the one exposed to the aqueous environment [55] [56].

The production of SLBs can be achieved by Langmuir-Blodgett technique, vesicle fusion (VF) or a combination of both. In this thesis, we used the VF method due to the high reproducibility, simple handling and high compatibility to protein incorporation. The strategy is based on the use of small unilamellar vesicles (SUVs) that are produced by the extrusion of multilamellar vesicles (MLVs) by ultrasonication of aqueous lipid suspensions. When the SUVs are exposed to the hydrophilic support, the vesicles from the bulk start to be adsorbed onto the substrate. Initially, the SUVs fuse with one each other and eventually rupture and spread to build a planar membrane. The process can be accelerated by the presence of divalent cations such Ca^{2+} and Mg^{2+}.

Proteins, nanoparticles and other species can be later incorporated inside the SLB or at its surface [53]. In this work, proteins were attached to the SLB surface by non-covalent Nickel (Ni^{2+})/hexahistidine-Tag interactions. This type of protein binding (complex formation) is comparatively weak (Kd ~ 10^{-6} M) [57] compared to other non-covalent interactions (i.e. biotin-avidin Kd ~ 10^{-15} M [58]), but the high density packing of the protein added with the high sensitivity and selectivity of the Ni/His-tag binding, allows to develop an ordered and stable IAV envelope model system in solution and in air (**Figure 1.5**).

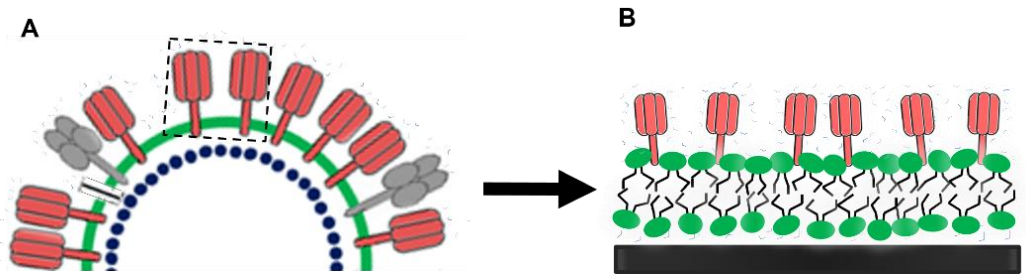

Figure 1.5. Supported lipid bilayer (SLB) with HA incorporated as model system of the IAV envelope. (A) IAV envelope structure. (B) SLB with HA at high density packing adsorbed to a solid substrate. In (A) the dark blue circles represent the M1 protein, the big green semi-circle represents the lipid membrane, the white barrel-like structure represents M2 channel, the grey mushroom-like structures represent NA, the red peanut-like shape structures represent the HA. In (B) the red peanut-like shape structures represent HA (without the transmembrane domain), the green circles with black lines represent the lipid bilayer (displayed as the head of the lipid linked to the alkyl tails), the grey rectangle represents the glass substrate. Note that in (A) and (B) the light blue "v" shape structures represent water molecules in solution. In (B) the lipid bilayer is not scaled and is enlarged with respect to the HA proteins. For simplicity, the glycosylation sites are not displayed.

1.3.3 *Live attenuated Influenza vaccines (LAIVs)*

The last strategy to mimic the IAV envelope and emulate the hydration taking place on its surface is by studying live attenuated Influenza vaccines (LAIVs). LAIVs refer to weakened viruses with respect to the wild type, which rely on limited replication by the introduction of temperature sensitive and point mutations in internal protein gene segments [59]. By keeping the surface structure and stability of the virus, they can activate the immune system of the host, but safely avoid any symptoms associated with influenza disease.

LAIVs, in analogy to all other Influenza virus vaccines, are annually updated. This is required due to the ability of the viruses to mutate, but especially to reassort the RNA strands (i.e. exchanging complete RNA strands between different viruses), and hence to escape the immune defense mechanisms. The vaccines contain different virus strains within the same formulation to cover a whole range of virus subtypes. Most common are trivalent or quadrivalent compositions. While trivalent compositions consist of two IAV subtypes and one IBV lineage, quadrivalent vaccines contain two IAV subtypes and two IBV lineages. The latter have become standard because of increased and co-circulation of the lineages B/Yamagata and B/Victoria [60]. The general route of LAIVs administration is nasal; thus the formulation is in aqueous media [59].

In this research, harmless monovalent LAIV is presented as a conventional candidate to perform biophysical studies on the IAV envelope (**Figure 1.6**). The main

advantages are related to the preservation of the virus morphology, aqueous formulation and safety in manipulation. Here, the samples were adsorbed on flat substrates and the surface morphology of the virus was evaluated by AFM at ambient humidity (i.e. "medium humidity", (50 ± 5) % of RH). In terms of methodology, these novel aspects are related to virus immobilization and imaging after sample dehydration. AFM studies on viruses are not new, but complete IAV have very rarely been scanned in air.

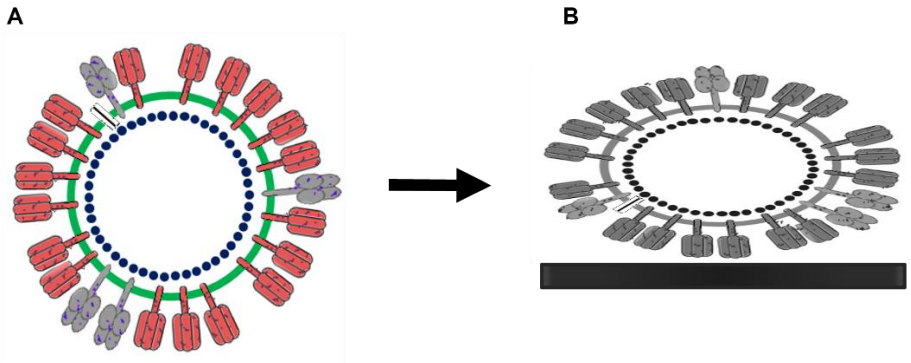

Figure 1.6. Live attenuated Influenza vaccine (LAIV) as a model system of the IAV envelope. (A) IAV envelope structure. (B) LAIV adsorbed to a solid substrate. In (A) the dark blue circles represent the M1 protein, the big green semi-circle represents the lipid membrane, the white barrel-like structure represents M2 channel, the grey mushroom-like structures represent NA, the red peanut-like shape structures represent the HA. In (B) the same structures are displayed but the change in color points towards IAV attenuation. The elliptic structure represents possible strong interactions between the sample and the substrate that may affect the virus morphology.

1.4 OBJECTIVES

The goal of this research is to provide scientific information on the hydration mechanisms of IAV by studying the effect of RH on models of IAV envelope. A purely physical interpretation in terms of virus morphology and (humidity-dependent) hydration is tested as a hypothesis to investigate if and how hydration layers can preserve IAV in an active form. This certainly will allow elucidating the IAV transmission mechanisms from a biophysical interpretation.

In **Chapter 2**, all techniques are described, namely contact angle measurement, Dynamic Light Scattering (DLS), Zeta Potential (ZP), protein Electrophoresis, Vibrational Sum Frequency Generation Spectroscopy (VSFG), Fourier Transform Infrared Spectroscopy (FT-IR), Electron Microscopy, Confocal Fluorescence Microscopy, Raster

Image Correlation Spectroscopy (RICS), Line-Scan Fluorescence Correlation Spectroscopy (LSFCS) and AFM.

In **Chapter 3** *Dimanno*-AuNPs are presented as model systems of the IAV surface glycoprotein HA. The stability and hydration water of the particles are provided in solution and after dehydration. The study culminates with the analysis on the water adsorption of the particles at different RH. To this aim, DLS, ZP, VSFG, FT-IR, Electron Microscopy and AFM are applied as complementary approaches.

In **Chapter 4**, SLBs are introduced as flat geometry models of the IAV envelope. Here, an SLB containing the HA at very high density is studied in complete cycles of hydration, dehydration and rehydration and the membrane performance is evaluated in terms of structure and dynamics based on Confocal Fluorescence Microscopy, RICS, LSFCS and AFM.

In **Chapter 5**, a monovalent LAIV is studied as model system of the complete IAV envelope and the virus morphology is resolved by AFM at ambient RH.

Finally, **Chapter 6** encloses the main findings and outlook of the present investigation.

Chapter 2

Methodology

The results of this thesis have been obtained by using different experimental techniques which are described in this chapter. Contact angle, Dynamic Light Scattering, Zeta Potential, Vibrational Sum Frequency Generation Spectroscopy, Fourier Transform Infrared Spectroscopy and Electron Microscopy were applied for the research presented in Chapter 3, while Sodium Dodecyl Sulfate Polyacrylamide Gel Electrophoresis, Fluorescence Microscopy, Line-Scan Fluorescence Correlation Spectroscopy and Raster Image Correlation Spectroscopy are the basis of Chapter 4. Atomic Force Microscopy was the transversal technique in this investigation, being applied in Chapters 3, 4 and 5.

2.1 CONTACT ANGLE

Contact angle measurements are essential for understanding the wetting or de-wetting properties of solid surfaces and the inter-facial phenomena taking place between a drop and a surface at the microscale. The term refers to the tangent drawn at the triple point (solid, liquid and vapor phases) of a sessile drop in contact with a substrate surface, when a liquid is deposited on it (**Figure 2.1**) [61].

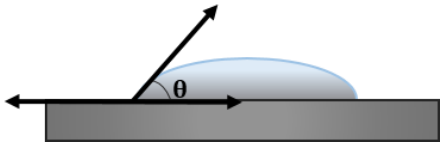

Figure 2.1. Sessile drop on a solid substrate.

Surface /Coating	Water contact angle (°)	Type of surface
TEOS	< 5	Super-hydrophilic
Mica	< 5	Super-hydrophilic
SiO_2	24	Hydrophilic
APDMES SiO_2	60	Hydrophilic
HDMSO	96	Hydrophobic
TCFS	106	Hydrophobic
HDMSO*	154	Super-hydrophobic
TCFS*	156	Super-hydrophobic

Table 2.1. Water contact angle of tetraethoxysilane siloxane (TEOS), Mica, oxidized silicon (SiO_2); 3-(ethoxydimethylsilyl) propylamine on silicon (APDMES SiO_2), hexamethyldisiloxane (HMDSO) and fluorinated siloxane coatings (TCFS). Note that * refers to conditions used to achieve super-hydrophobic wetting properties. Adapted from [62].

Contact angles can be obtained easily by goniometry. In this technique, the contact angle is measured by an image captured from the profile of a drop that is adsorbed on the specimen's surface. The resulting value is a semi-quantitative indication of the degree of wetting of a surface. The liquid is considered as wetting the surface of a solid when the contact angle is less than 90°. On the other hand, if the contact angle is greater than 90°, the liquid is considered as non-wetting. Hence, for water a large contact angle is indicative of hydrophobic surfaces (non-wetting) while low contact angles are associated with

hydrophilic surfaces (wetting). Usually, water contact angles of < 5° indicate completely hydrophilic surfaces (super-hydrophilic), above 90° the surfaces are nicely hydrophobic, while contact angles > 150° correspond to super-hydrophobic surfaces (**Table 2.1**).

2.2 DYNAMIC LIGHT SCATTERING (DLS)

DLS, also known as photon correlation spectroscopy or quasi-elastic light scattering, is a non-invasive technique commonly used for the determination of the size distribution of particles in the diameter range of 1 - 2 nm to 3 - 5 μm [63]. It primarily measures the Brownian motion of particles in solution that arises as a consequence of the random collision of the particles with the molecules of the liquid. Such motion is slower for large particles, where the diffusion results in small changes of the position at different time points, compared to small particles, where the faster movement does not allow to remain in the vicinity of a certain position [64]. The continuously mobile particles cause constructive and destructive interferences and hence, the intensity of scattered light fluctuates over time. This fluctuation of intensity (I) in scattered light is correlated against short decay intervals (τ) and the intensity autocorrelation function (ACF) $G_{DLS}(\tau)$ is obtained through **Equation 2.1**:

$$G_{DLS}(\tau) = \langle I(t).I(t+\tau)\rangle$$

Equation 2.1. Autocorrelation function (ACF) used in DLS measurements.

For a large number of monodisperse particles in Brownian motion, the correlation function G_{DLS} is an exponential decaying function of the correlator time delay τ (**Equation 2.2**):

$$G_{DLS}(\tau) = A[1 + Bexp(-2D_{trans}q^2\tau)]$$

Equation 2.2. ACF for a monodisperse sample.

where A is the baseline of the correlation function, B the intercept of the correlation function, and q is defined by:
$q = \left(\frac{4\,\pi\,n}{\lambda o}\right)\sin\left(\frac{\theta}{2}\right)$, where n = refractive index of dispersant, λo the wavelength of the laser, and θ the scattering angle (all known and constant). Fitting $G_{DLS}(\tau)$ logarithmically to the time delay τ gives $-2D_{trans}q^2\tau$ and hence D_{trans}, the 3-dimensional translational diffusion coefficient.

The D_{trans} can be related to the (hydrodynamic) size of the particle by the Stokes-Einstein equation (**Equation 2.3**), which corresponds to the diameter of a sphere that has the same D_{trans} as the particle:

$$d_H = \frac{k_B T}{3\pi\eta D_{trans}}$$

Equation 2.3. Stokes-Einstein equation used for the determination of particle hydrodynamic diameter.

where d_H is the hydrodynamic diameter, k_B is the Boltzmann constant, T the absolute temperature and η the viscosity [65].

The hydrodynamic diameter (d_H) obtained by DLS is a hypothetical measurement as such hard spheres hardly exist in colloidal dispersions. In reality, the dispersed particles are hydrated or solvated and a part of the hydration layer contributes to d_H. Overall, the hydrated surface is dynamic. It fluctuates over time, depending on ionic strength, interaction with other molecules in the suspension and types of solvents. Therefore, DLS provides only an indicative size of the colloid [66].

In practice, the correlograms obtained from the autocorrelation curves compare one intensity signal with itself at short time intervals. From this, the value d_H can be extracted as "size average". In a monodisperse sample, if the particles are large the signal will be changing slowly and the correlation will persist for a long time (**Figure 2.2 A**, blue line). In contrast, if the particles are small and moving rapidly, the correlation will decrease more quickly (**Figure 2.2 A**, pink line).

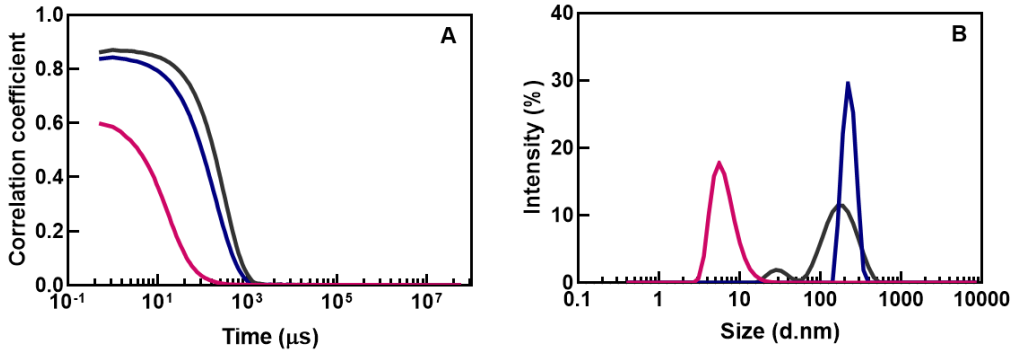

Figure 2.2. Correlograms and hydrodynamic diameters experimentally obtained for gold nanoparticles (AuNPs) and polystyrene (PS) beads. (A) Correlograms of the scattered intensity of the colloidal system obtained by the correlation coefficient as function of decay times. (B) Calculated particle size distributions. The pink line corresponds to 6 nm AuNPs, the blue line corresponds to 207 nm PS beads and the grey line corresponds to 75:25 6 nm AuNPs and 207 nm PS. Note that in (B) the intensity for a polydisperse sample (grey line) is not representative of the sample components.

Additionally, a more complex fit procedure provides not a single size but a size distribution of the particles. A suspension from a mixture of the abovementioned particles provides a more complex correlogram (**Figure 2.2 A**, grey line).

From this, the size distribution is a plot of the relative intensity of light scattered by particles in various size classes (**Figure 2.2 B**, grey line). But, because the measurement is based on intensity, in polydisperse samples scattering from large aggregate species results in strong signals, which are not representative of the number of particles in solution (**Figure 2.2 B**, pink and blue lines). This effect can be corrected by converting the data into number distributions. However, the peaks of the size distribution do not fit very well.

The polydispersity index (PDI) can also be extracted from the correlation data. This index is dimensionless and varies between 0 and 1. Values around 0.05 are generally obtained in highly monodisperse standards while values greater than 0.7 indicate that the sample has a very broad size distribution.

2.3 ZETA POTENTIAL (ZP)

The ZP, also termed as electrokinetic potential, is a physical property which is exhibited by any particle or material surface in suspension. When a colloidal particle is dispersed in an electrolyte (solvent plus ionic salt), the liquid layer surrounding the particle exists as two parts; an inner region – named as the Stern layer – and an outer diffusive layer. In the Stern layer, the ions are generally of opposite charge of the particle and thus, are tightly bound. In the diffusive layer, cations and anions are less firmly associated, as the electrostatic effects due to the surface charge of the particles decrease. Also, a gradient in concentration of ions outward the particle is formed until it matches the bulk. Within this layer there is a notional boundary, inside which the ions and particles form a stable entity, called the slipping plane [66].

When a particle moves, ions within the boundary travel with the particle while the ions beyond the boundary stay with the bulk dispersant. The electrical potential that exists at the slipping plane is referred as the ZP.

In practical terms, the ZP can be determined by measuring the electrophoretic mobility of a particle with the DLS equipment. Once the size distribution is obtained, an electric potential is applied, and the particles move toward the electrode of opposite charge. This movement is slowed down by the viscous drag on the particle, such that the particle travels with constant velocity [67]. Its mobility is called electrophoretic mobility, and can be defined by the by the Henry equation (**Equation 2.4**):

$$\mu_e = \frac{2\varepsilon\zeta f(Ka)}{3\eta}$$

Equation 2.4. Henry's equation used for the determination of particle Zeta Potential.

where μ_e is the electrophoretic mobility and ζ is the ZP. The other parameters are known: ε is the dielectric constant of the electrolyte, η the viscosity of the electrolyte and $f(Ka)$ is the Henry function [65].

ZP is indicative of the stability of the colloidal system. A dividing line between stable and unstable aqueous dispersions is generally taken at + 30 mV, or – 30 mV, as above these values the particles have sufficient ZP to repel each other and enable a high dispersion stability [67].

2.4 SODIUM DODECYL SULFATE POLYACRYLAMIDE GEL ELECTROPHORESIS (SDS-PAGE)

SDS-PAGE is a very common method used to estimate the molecular weight (MW) and concentration of proteins [63]. The working principle is the electrophoresis, referred to the movement of charged molecules in response to an electric field, resulting in separation. When electrophoresis is performed in a highly cross-linked gel formed by the reaction of acrylamide and bis-acrylamide (N,N′-methylenebisacrylamide), the gel –a porous network of narrow channels- serves as a molecular sieve in which proteins move slowly in response to the applied electric field. In this method, SDS detergent and denaturing agents are used to disrupt the mainly noncovalent interactions that provide a defined 3-dimensional shape to a protein. The negatively charged SDS now binds to the proteins by non-covalent interactions, providing an overall negative charge and a rod-like shape (**Figure 2.3**) [68]. Most important, the charge is supposed to be proportional to the rod length.

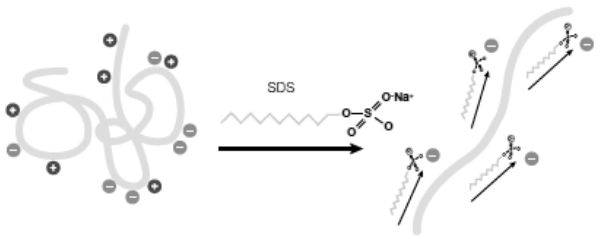

Figure 2.3. Effect of sodium dodecyl sulfate (SDS) on the conformation and charge of a protein. Extracted from [68].

By denaturing the proteins and giving them a uniform negative charge, it is possible to estimate the MW of a protein (sample) by comparing its electrophoretic mobility with respect to standard proteins (M) of known MW (**Figure 2.4**).

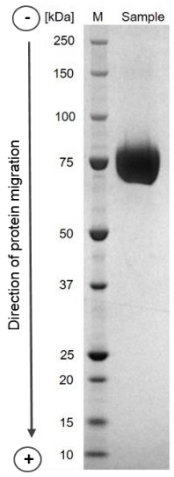

Figure 2.4. H1N1 hemagglutinin (HA) molecular weight (MW) estimation by electrophoresis in a polyacrylamide gel. The electrophoretic mobility of HA on an SDS-PAGE is related to its MW. Standard proteins ("M" in the Figure) of known MW are subjected to electrophoresis. These marker proteins can be used to estimate the MW of HA ("Sample" in the Figure). Adapted from [69]

2.5 FOURIER TRANSFORM INFRARED SPECTROSCOPY (FT-IR)

FT-IR is a non-invasive photon in/photon out technique commonly used to characterize organic and inorganic samples by the absorption (or transmission) of light at the infrared (IR) region of the electromagnetic spectrum. The IR absorption produces molecular vibrations (i.e. bending, stretching) of the molecular bonds of the material, resulting in a unique fingerprint IR spectrum [9], which can be described by **Equation 2.5**:

$$P^{(1)}(\omega_1) = \mu^{(1)} : E_1(\omega_1)$$

Equation 2.5. Working principle in infrared (IR) spectroscopy.

where $P^{(1)}$ is the input photon with IR frequency ω_1, $\mu^{(1)}$ is the transition dipole moment and E_1 the input electrical field (usually only the electric dipole is considered).

As a general rule, the electric dipole moment of the molecule must change to show IR absorption. So highly symmetric molecules such as nitrogen and oxygen are IR-inactive, while water in all phases has three IR-active vibrations. Gas phase (vapor) absorption bands are very narrow. Metals and simple ionic compounds (salts) show often only very broad non-characteristic absorption.

An FT-IR spectrum is generated by an incident IR beam that passes through an interferometer, in which the beam path length is continuously increased and decreased, resulting in an interference pattern. A fast software routine calculates the FT of the pattern into a IR representation of intensity as a function of wavenumber, being this a direct indication to its energy and frequency, the background spectrum. The maximum intensity is usually around 1500 cm^{-1}. Water vapor and CO_2 dominate the absorption, though they are present in very small concentrations. There are no absorption bands above 4000 cm^{-1}, and below 400 cm^{-1} optical elements absorb all intensity. When the sample is placed in the spectrometer, the beam excites vibrational transitions (absorption) [10], the interferogram changes, and its transform is now the desired IR spectrum. However, when the sample is very thin background and spectrum almost overlap (**Figure 2.5 A**).

The final absorption spectrum of the sample is then obtained after the background is subtracted. This gives principally a flat curve without signals from the gas phase [11]. All absorption bands can now be used to chemically characterize the sample material (**Figure 2.5 B**). In complex compounds, the molecular vibrations taking place sometimes are hard to interpret as the fingerprint region (400 cm^{-1} to 1800 cm^{-1}) exhibits a "forest" of absorption peaks. The high frequencies (1800 cm^{-1} to 4000 cm^{-1}) contain only a few bands from typical bond stretching vibrations of light elements.

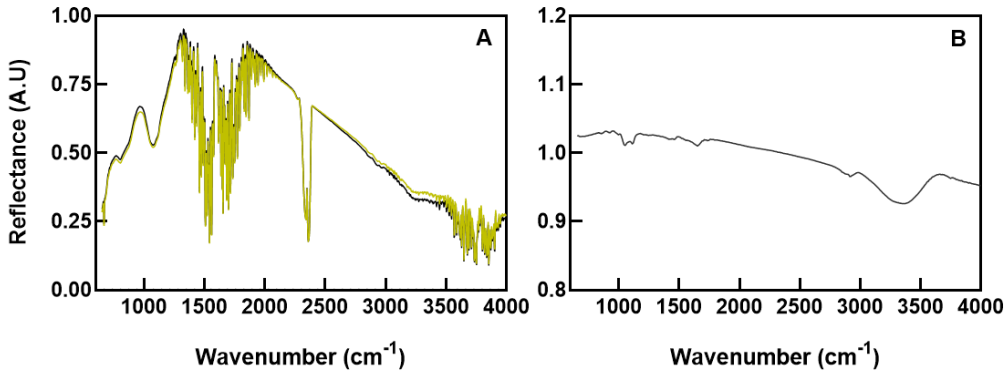

Figure 2.5. Fourier Transform Infrared Spectroscopy (FT-IR) spectra of dimannoside AuNPs (*Dimanno*-AuNPs) on gold obtained with a grazing incidence (GIR) objective in the fingerprint region. (A) The yellow line displays the spectra from the background and the black line displays the spectra from the sample. All narrow negative peaks are absorptions from gas phase water (1300 to 2100 cm^{-1} and above 3300 cm^{-1}) and CO_2 (double peak around 2350 cm^{-1}). (B) FT-IR of the sample obtained after subtraction of the background signal, effects from the gas phase are eliminated, and the background is flat.

Our samples were examined in reflection geometry under grazing incidence (GIR). In these conditions, the ultrathin samples on gold surfaces interact with the p-polarized

fraction of light (beam polarized normal to the surface), but not with the s-polarized one (parallel to the surface).

2.6 VIBRATIONAL SUM FREQUENCY GENERATION SPECTROSCOPY (VSFG)

VSFG is a nonlinear laser spectroscopy used for the characterization of fast surface molecular dynamics, specially taking place at heterogeneous interfaces. This second order non-linear optical process converts two intense input photons into a new photon, with a frequency that is the sum of the input frequencies. The two electromagnetic waves with frequencies ω_1 and ω_2 interact at the interface and induce a non-linear polarization, which can be described by **Equation 2.6**:

$$P^{(2)}(\omega_s = \omega_1 + \omega_2) = \chi^{(2)} : E_1(\omega_1)E_2(\omega_2)$$

Equation 2.6. Non-linear polarization induced by two electromagnetic waves in a medium.

where $\chi^{(2)}$ is the nonlinear susceptibility of the medium, and E_1 and E_2 are the input optical fields [70]. Under the electric dipole approximation, $\chi^{(2)}$ is non-zero only if the sample has no inversion symmetry.

In a centrosymmetric or disordered medium (liquids, gases, gold or silicon) the VSFG process is inactive, and only interfaces contribute signals. Hence, the technique is often used to selectively observe an interface between two centrosymmetric bulk media, as the inversion symmetry is broken at the interface.

The VSFG process can, in a simplistic way, be understood as a combination of IR absorption (**Figure 2.6**, green arrow) and anti-stokes Raman scattering (**Figure 2.6** blue and violet arrows). Though SFG is not a sequential absorption, but a synchronous process involving three photons, this view can help to determine the selection rules of VSFG: for a vibrational mode to be VSFG active, it must be both Raman and IR active [10]. While in FT-IR some signals come from the interface and other from the bulk surface, in VSFG the signal is strictly related to interface phenomena where the symmetry is broken.

In a typical VSFG setup, two pulsed laser beams, one at IR frequency (ω1) and the other at visible frequency (ω2), spatially and temporally overlap at an interface and generate an output beam with a frequency equal to the sum of the two input frequencies, traveling in a direction given by the sum of the wave vectors of incident beams [71]. The sum frequency signal is then collected in e.g. reflection at ppp and ssp polarization of light. These configurations, in particular the ssp, usually give good signals of thin molecular layers at the solid-gases interfaces.

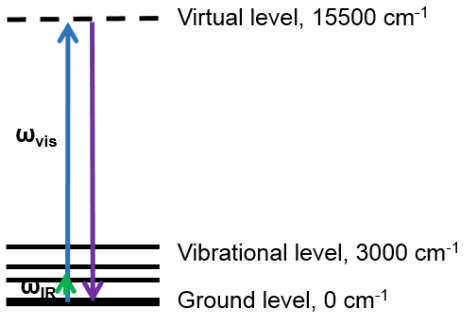

Figure 2.6. Energy diagrams of Vibrational Sum Frequency Generation Spectroscopy (VSFG). Example for a vibrational level at 3000 cm^{-1} (IR laser tuned to this energy) and a visible laser at 12500 cm^{-1} (corresponding to 800 nm wavelength). The sum frequency emission is then at 15500 cm^{-1}, again in the visible range (~ 645 nm, orange). Note that the green arrow shows IR absorption, the blue arrow indicates visible absorption and the violet arrow indicates VSFG emission.

To enable sufficient signal for detection, two main spectrometers can be used, scanning systems and broadband systems. Among both, the results obtained in this thesis have been performed by using broadband spectrometers. In this setup, one picosecond laser beam (typically the visible laser) is kept at a fixed narrow wavelength, and the other femtosecond laser beam (the IR laser) produces a spectrally broad beam. The beam overlap at the interface being studied, covers a wide range of frequencies. The delay time between pulses allows system relaxation after heating and thus fast, real-time, and interface-sensitive measurements with negligible beam damage.

2.7 SCANNING ELECTRON MICROSCOPY (SEM)

SEM is a versatile advanced instrument which is largely employed to observe the surface of materials. The sample is scanned with a high energy electron beam, and the emitted electrons are detected for each position.

The SEM instrument is based on the scanning principle: The primary electrons are confined to a monochromatic beam in the nanometer range by electric or magnetic field lenses and "raster scanned" across the sample surface. Depending on their energy, they penetrate the material to a certain depth, and interact in different ways. These interactions generate different signals (electrons and photons) which can be collected and detected. Most important is that electrons of the specimen can be released as so-called secondary electrons. By scanning simultaneously in two perpendicular directions, a rectangular area of the specimen can be analysed, and an image can be obtained by collecting the secondary electrons from each point of the specimen [72].

To produce a sub-nanometer dimension probe, a field-emission source is used, in which electrons are released from a very sharp tungsten/zirconium dioxide tip [72]. The primary electrons emitted from this electron "gun" are accelerated by a strong electrical field in the range of 1 − 40 keV [73]. To achieve high resolution images, SEM operates at high vacuum to avoid interactions of electrons with gas molecules.

Scanning transmission electron microcopy (STEM) results from combining the advantages of transmission electron microcopy and SEM, thus collecting a transmission image by the scanning method [74]. The SEM microscope setup can operate in STEM mode by focusing the beam to a fine probe and scanning across a thin sample specimen. Now, only electrons that emerge from the opposite site ("below") of the specimen are detected. For this, an annular detector placed below the sample detects electrons that are scattered, usually by heavy atoms. This method is called "dark field". Non-scattered electrons (i.e. the attenuated primary beam) are detected by a disk in the centre of the ring ("bright field"). Other detectors, e.g. for the low energy secondary electrons, can additionally be placed elsewhere, e.g. above the sample, in the same way as for standard SEM.

2.8 FLUORESCENCE MICROSCOPY

Since its development in 1950s, Confocal Fluorescence Microscopy allows selective examination of a particular component of a complex biomolecular assembly (i.e. cells or tissue) by the exploitation of light. The technique is again photon in/photon out, but based on fluorescence, which refers to the luminescent emission that results from the absorption of photons by molecules, known as fluorophores.

The principle of fluorescence can be understood by **Figure 2.7**. When a fluorophore absorbs light, it is promoted to an excited electronic state, and in there to a high vibrational level (**Figure 2.7 A**, continuous light blue line). Now de-excitation takes place, first by a decay of the vibrational energy level. This is usually radiation-less (without photon emission), and known as Stokes shift (**Figure 2.7 A**, continuous pink line), which is very fast (10^{-12} s) [75]. Further energy dissipation can result in the emission of a photon within nanoseconds (10^{-9} s), this fluorescence is observed at a longer wavelength (lower energy) than the absorbed photon (**Figure 2.7 A**, continuous green line; **Figure 2.7 B**). .

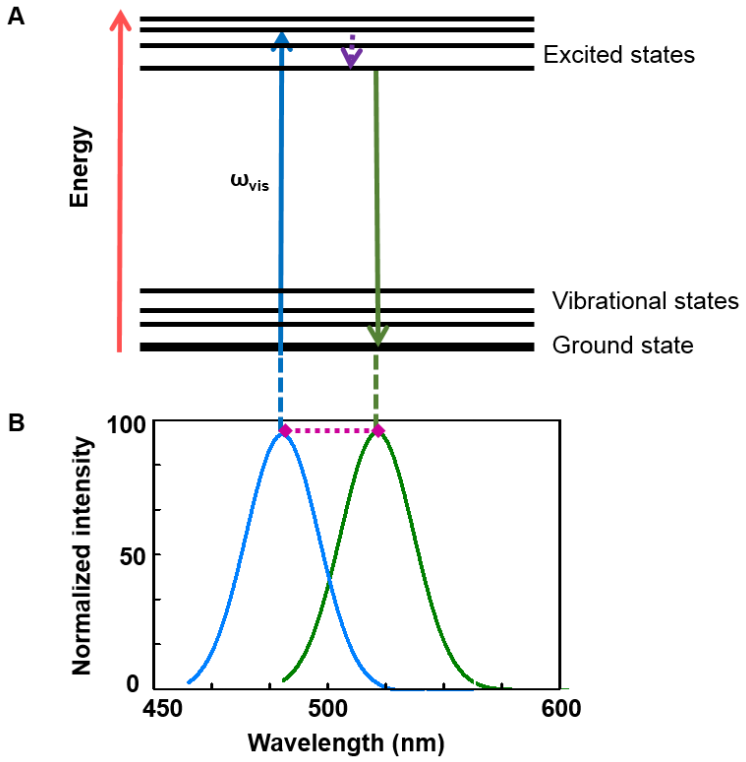

Figure 2.7. Basic principles of fluorescence. (A) Representative diagram illustrating the absorption of a photon and fluorescence emission at a longer wavelength. (B) Excitation and emission spectra of GFP typically obtained in Confocal Fluorescence Microscopy measurements. Note that the light blue line represents energy absorption; the green line exhibits energy emission; the violet line represents non-radiative energy dissipation and the pink line represents the Stokes shift.

In Confocal Fluorescence Microscopy the physical principles of fluorescence are used to observe sample specimens. As each fluorophore exhibits its own absorption (excitation) and emission spectra, samples can be observed in a wide range of wavelengths, and a combination of several fluorophores within a single sample is also possible. The working principle stands for a specimen labeled with fluorescent dye(s) – or an autofluorescence specimen (e.g jelly fish *Aequorea Victoria*) – that is illuminated with light of the absorption wavelength. This excitation can be from a laser at a well-defined color (**Figure 2.7**), but also from a broadband ("white") source, such as a UV lamp. The emitted fluorescence is viewed using a barrier filter that is opaque to the absorbing wavelength but transmits the longer wavelength of the emitted light. As a result, the structures marked

with the fluorescent dye light up, while the unlabeled molecules remain dark (**Figure 2.8**) [76].

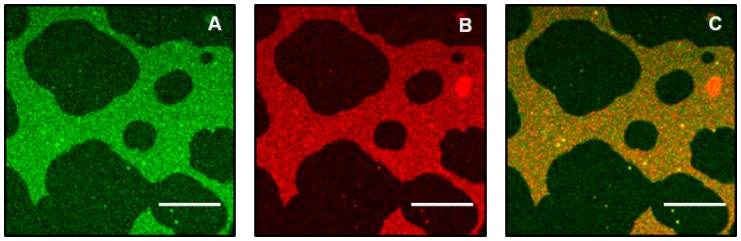

Figure 2.8. Confocal Fluorescence Microscopy images of carbon monoxide dehydrogenase bound to a supported lipid bilayer (SLB) in solution. (A) Fluorescent dye lighting up from the SLB. (B) Fluorescent dye bound to the protein. (C) Overlapped images (A and B). Note than the fluorescently labeled structures light up while the unlabeled molecules remain dark. The result from the overlapped images exhibits protein bound to the SLB. Scale bars correspond to 20 μm.

2.8.1 *Advanced quantitative Fluorescence Microscopy*

Because of the continuous advances of the basic confocal fluorescence microscope, nowadays not only is possible to observe a large array of biological samples including live cells, but also to characterize and quantify cellular processes like diffusion or transport. Among the wide number of developed techniques, fluorescence correlation spectroscopy (FCS) has gained increasing interest for studying lipid and protein diffusion coefficients, chemical rate constants, molecular concentrations, and other molecular parameters from confocal images, thus providing a bridge between classical ensemble and single-particle measurements [77].

FCS measures in short time scales small fluctuations of the signal coming from fluorescently labeled molecules that diffuse in a defined femtoliter observation volume. Similar to DLS methods (**section 2.2**), the temporal correlation of the individual molecules with themselves is calculated into an ACF, which provides information on the average number of molecules and the diffusion time in the observation volume [78].

Typically, the small detection volumes can be provided by a confocal laser scanning microscope, where a laser is focused to a diffraction limited spot by the objective and where a pinhole in the emission channel provides tight axial confinement. The fluorescence signal in the detection volume can vary both because the fluorophores move into and out of the detection volume, as a consequence of diffusion or transport, and because of photophysical or photochemical reactions (i.e. photobleaching) which cause fluctuations in the detected emission. This fluctuating fluorescence signal is recorded as a fluorescence intensity trace and analyzed by calculating the ACF, which measures the self-similarity of the signal in

time, relating the fluorescence signal with itself at different lag times [79]. In this sense, the temporal ACF is given by **Equation 2.7**:

$$G_{FCS}(\tau) = \frac{\langle \delta F(t).\, \delta F(t+\tau) \rangle}{\langle \delta F(t) \rangle^2}$$

Equation 2.7. **ACF used in fluorescence correlation spectroscopy (FCS) methods.**

where $G_{FCS}(\tau)$ is the normalized temporal ACF; δF is the fluorescence intensity fluctuation with respect to the average, τ is the delay time between successive sampling of the fluorescence signal and the angled brackets ⟨ ⟩ indicate time averages.

To derive expressions from **Equation 2.7**, novel FCS techniques have developed ACF with defined spatial sampling.

In Line-Scan FCS (LSFCS), the laser beam is scanned over the sample in a linear fashion. The detection volume is moved with respect to the sample, and the residence time of the fluorophores in the detection area is highly reduced. The ACF is determined by the assumption that a line is scanned repeatedly over the sample with a constant velocity ν (**Figure 2.9 A).**

The intensity traces of the line scans i can be arranged vertically to form a "pseudo-image", which is defined as $F(x, t_i)$, and is acquired at the time $t_i + x/v$. In this pseudo image, the horizontal axis exhibits the position in the sample and the vertical axis the time $t_i = i$ T, which is an integer multiple of the scanning period T (**Figure 2.9 B**). The ACF is then defined as:

$$G(\xi, \tau_i) = \frac{\langle \delta F(x, t_i).\, \delta F(x+\xi, t_i+\tau_i) \rangle}{\langle F(x, t_i) \rangle^2}$$

Equation 2.8. Spatiotemporal ACF developed for Line-Scan FCS (LSFCS).

where $G(\xi, \tau_i)$ is the spatiotemporal ACF and $\delta F(x, t_i) = F(x, t_i) - \langle F(x, t_i) \rangle$. The value ξ is the spatial lag variable and the $\tau_i = i$ T is the discrete lag time.

With the assumption that the diffusion of the molecules is not influenced by the scanning laser beam and that the spatial pixel size S is much smaller than the waist w_0 of a Gaussian detection area, the spatiotemporal correlation function for one diffusing species can be defined in a 2-dimensional flow-diffusion model by **Equation 2.9**:

$$G(\xi,\tau_i)=\left(\frac{1}{C\pi w_0^2}\right)\exp\left[-\frac{\xi^2}{w_0^2+4D\,(\tau_i+\frac{\xi}{v})}\right]\times\left(1+\frac{4D}{w_0^2}\left(\tau_i+\frac{\xi}{v}\right)\right)^{-1}$$

Equation 2.9. Spatiotemporal ACF developed for LSFCS assuming a 2-dimensional flow-diffusion model and a Gaussian detection area.

where C stands for the concentration (number per area) of fluorophores and D the diffusion coefficient. Note that while in DLS D_{trans} is 3-dimensional, in LSFCS D is 2-dimensional.

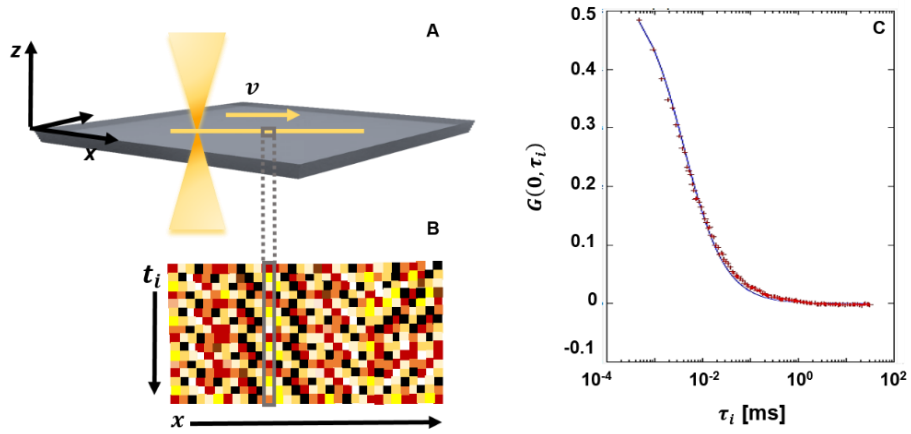

Figure 2.9. Principle of LSFCS. (A) A line is scanned repeatedly over the sample with a constant velocity ν. (B) Line scans can be arranged vertically to form a pseudo-image where the vertical axis represents the time. (C) Typical experimental temporal correlation curve $G(0,\tau_i)$ obtained from the pseudo image (red crosses) and fitted to a 2-dimensional flow-diffusion model (blue line). Note that one pixel is compared to the rest of the pixels in the same line and in the other lines as well. This results in spatiotemporal correlation curves $G(\xi,\tau_i)$.

Experimentally, the intensities of every pair of pixels in each line are correlated to detect characteristic decay times corresponding to dynamical processes. By fitting the experimental correlation curve to **Equation 2.9**, information on dynamics as C, D and w_0 can be extracted (**Figure 2.9 C**) [80].

In Raster Image Correlation Spectroscopy (RICS), molecular kinetics are explored by measuring many focal points within the scan. Both temporal and spatial fluorescence intensity fluctuations are recorded by scanning a laser beam over a sample. Hence, information on dynamics is obtained from successive lines and frames; between adjacent pixels in the x-direction adjacent pixels in the y-direction (**Figure 2.10**) and by comparing successive images.

The ACF used in LSFCS can be further extended to spatial coordinates acquired in the horizontal and vertical positions. In this investigation, single frames were obtained in a 2-dimensional diffusion model given by **Equation 2.10** [81] [82].

$$G(\xi,\psi) = \left(\frac{1}{N}\right)\exp\left[-\frac{(S\xi)^2+(S\psi)^2}{w_0^2+4D\left(|\tau_p\xi+\tau_i\psi|\right)}\right]\times\left(1+\frac{4D}{w_0^2}\left(|\tau_p\xi+\tau_i\psi|\right)\right)^{-1}$$

Equation 2.10. Spatiotemporal ACF developed for Raster Image Correlation Spectroscopy (RICS) assuming a 2-dimensional flow-diffusion model and a Gaussian detection area.

where ξ and ψ and refer to the spatial coordinates acquired at different time points τ_p and τ_i respectively, N is the average number of particles in the observation volume and S refers to the pixel size. Note that the equation is given for single frames hence there is no explicit time coordinate between successive images. Similar to DLS and LSFCS, by fitting $G(\xi,\psi)$, the 2-dimensional D can be extracted.

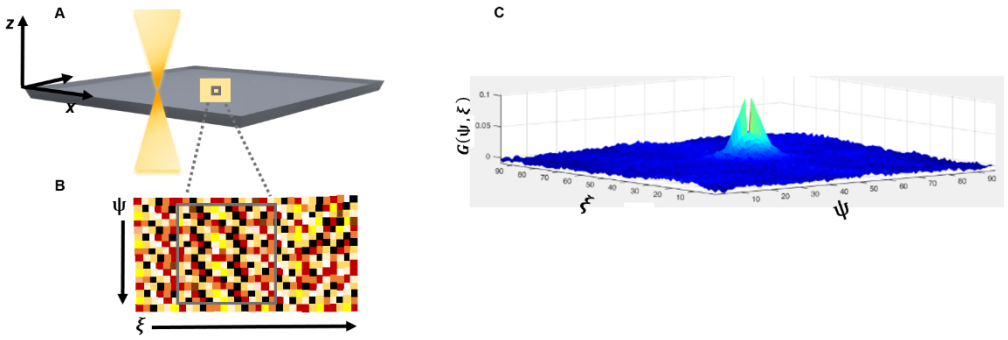

Figure 2.10. Principle of RICS. (A) A single frame is taken in 2-dimensions. (B) Pixel scans can be arranged in 2-dimensions to form a pseudo-image. (C) Experimental correlation curve G(ψ, ξ) obtained from the pseudo image and fitted to a 2-dimensional flow-diffusion model.

2.9 ATOMIC FORCE MICROSCOPY (AFM)

AFM is a type of Scanning Probe Microscopy (SPM) developed for investigating the properties of a sample, at or near the sample surface. SPM instruments in principle present a sharp probe (tip) that is in near, intermittent, or continuous contact with the sample. The tip performs a "raster scanning" across the sample surface and the interactions (usually mechanical ones) are detected and mapped. For this, high resolution actuators usually made of piezoelectric materials, move the probe across the sample and back over each line

of the image area. For each pixel position (X/Y), the interaction of the tip and sample is recorded as one data point. The collection of data points is then synthesized into a high resolution image, in which a map of the surface is displayed [83].

In AFM, the sharp tip is located at the free end of a cantilever – the "probe" – and is brought into close contact with the sample surface. A laser spot is reflected from the cantilever onto a position-sensitive photodiode detector and the bending of the cantilever produces a change in the position of the laser spot. A piezoelectric element scans the tip across the sample in X and Y (or vice versa) and keeps the cantilever bending constant by controlling the Z position. The controller input value is the deflection signal from the detector and the output Z – the topography – is obtained as a function of X and Y **(Figure 2.11**) [83]. The topographic data are usually plotted with a greyscale or with colors that are assigned to Z values (**Figure 2.12**).

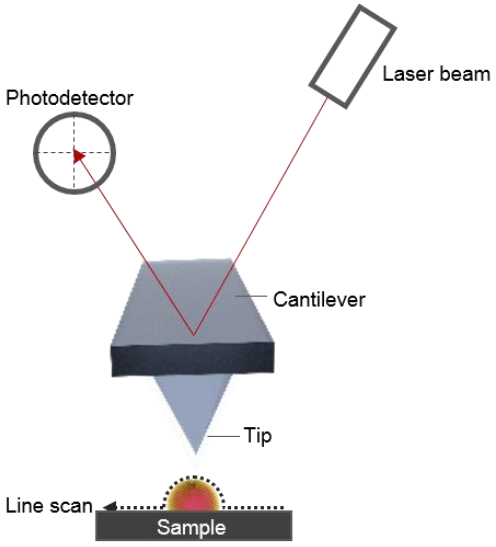

Figure 2.11. Atomic Force Microscopy (AFM) basic components. The tip and the sample surface constitute the sensor and the detection system is formed by the photodetector and the laser beam. Note that the tip movement across the sample is controlled by a piezoelectric material.

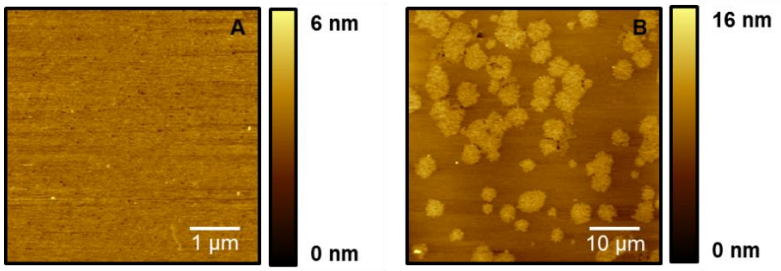

Figure 2.12. AFM topography image of a SLB in solution. (A) SLB deposited on mica where slight nanometric variations in signal are detected and converted into a color mapping. (B) SLB after the addition of HA where variations in signal intensity are evident. Note that differences in intensity colors suggest in (A) a homogenous and flat SLB on mica (light brown image) and in (B) a flat mica surface (dark brown) with HA bound to SLB patches (light brown structures).

From the topography images, height histograms and height profiles can be obtained. Also, the surface roughness can be extracted to evaluate the morphology and weight-average surface characteristics of the sample. This scale-dependent parameter can be expressed by the root mean square roughness (RMS roughness) which refers to the RMS average of the profile height deviations from the mean line, recorded within the evaluation length (**Equation 2.11**):

$$rms = \sqrt{\frac{\sum_{i,j}(a_{i,j} - < a >)^2}{N}}$$

Equation 2.11. AFM root mean square roughness (RMS roughness).

where $< a >$ refers to the mean height of the interval $< a >= \frac{\sum_{i,j} a_{i,j}}{N}$

The RMS roughness is calculated by the AFM equipment software. Generally flat and homogenous surfaces present low values of RMS roughness, while surfaces with adsorbed specimens tend to increase the RMS roughness (Table 2.2).

AFM images can achieve unprecedented vertical resolutions due to the small thermal vibrations and relatively high stiffness of the cantilevers. The vertical resolution (Δz) of a rectangular cantilever is determined by **Equation 2.12**:

$$\Delta z = \sqrt{\frac{4k_B T}{3k}}$$

Equation 2.12. AFM vertical resolution (Δz) of a rectangular cantilever.

where k_B is the Boltzmann's constant, k is the spring constant of the cantilever, and T the absolute temperature, considered as 298 K in ambient conditions. For a typical value of k = 1 N/m, the vertical resolution is 0.074 nm.

Surface	Area (μm^2)	RMS roughness (nm)	Reference
Mica	4x4	0.03	[84]
SiO_2	2x2	0.18	[85]
Gold	4x4	0.45	[84]
Glass	2x2	0.38	[85]
APDMES SiO_2	2x2	0.29	[84]

Table 2.2. AFM RMS surface roughness of mica, SiO_2, gold, glass and APDMES on SiO_2 in air.

Among the different ways to operate an AFM, the results from this thesis have been measured in contact mode and intermittent contact mode (AC mode or tapping mode). Both modes are used for high resolution imaging, but present differences based on the tip-sample interaction forces. These forces can be identified by considering the separation distance between the tip and the sample. Large separation distances of several nanometers lead to weak or medium-strong attractive forces: van der Waals forces, capillary forces, and electrostatic interactions. It is, however, quasi impossible to achieve stable and high resolution scanning in this regime. When decreasing the distance between the tip and the sample, the attractive forces notably increase till reaching a working distance – usually below 0.5 nm – in which a repulsive regime is caused by the interaction of the electron clouds from both tip and sample (**Figure 2.13**) [86]. Electrostatic or capillary forces can very much change the typically observed behavior. In extreme cases, the potential can be purely repulsive.

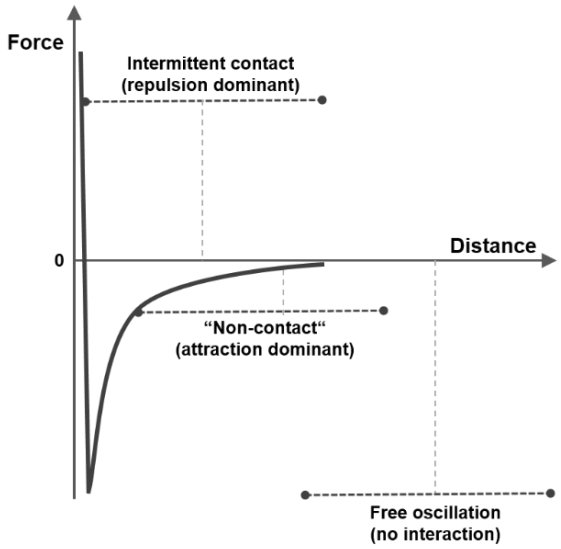

Figure 2.13. AFM interaction force versus separation distance.

Here, in contact mode, the scanning probe operates in the repulsive regime, with the tip being in direct physical contact with the surface. The total force applied during scanning is between 1 – 100 nN. In order to access also the attractive regime, the AC mode is used: The vertically oscillating tip moves through an interaction potential in either net repulsive forces (intermittent contact) or net attractive interactions (non-contact). In this mode, the cantilever is driven to oscillate, at or near one of its resonance frequencies. The forces involved in the tip-sample interactions cause changes in the amplitude, phase and resonance frequency of the oscillating cantilever. A feedback system is employed to maintain the oscillation amplitude at a setpoint value, resulting in an error signal that is used as the input to the feedback system. Under these conditions, the AC mode enables to reduce the total force applied to below 0.1 nN, providing minimum surface damage. Generally, hard surfaces can be scanned in contact mode or in AC mode, while soft surfaces as biological membranes, proteins or virus are probed in AC mode only.

AFM provides high resolution and 3-dimensional information of almost any kind of sample: the properties of conductive, non-conductive, hard or soft materials can be obtained in environments as variable as liquids, gases or vacuum. Among the vast number of applications provided by AFM, the adsorption of water surfaces in ambient conditions has gained increasing attention from a wide range of fields. Processes such as oxidation, catalysis, cell nutrition, magnetic recording, and sensing are just a few examples [87]. Specifically, AFM can be carried out in different humidity conditions, and the water adsorption by the sample can be correlated with the degree of hydration of the system [88].

On the one hand, the varying humidity may lead to a thin film of water that usually covers both tip and sample. If both specimens are sufficiently hydrophilic, a capillary neck is formed (**Figure 2.14 A**) and the measured "apparent height" can be up to four times higher than the so-called "true height" (in dry conditions) [89]. In AC, phase and amplitude change considerably (see below). Also, water films are extremely soft and easily detachable, so the force exerted by the tip may affect the reproducibility of the measurement. This might be enhanced by the working setpoint as the higher the setpoint is, the longer is the contact time with the sample. On the other hand, water perturbations can be straightforwardly controlled.

The AFM instrument can be used in such modes that true height measurements are achieved. Several approaches such as electrostatic AFM [90], dynamic AFM [87] and, more recently, amplitude modulated-frequency modulated (AM-FM) AFM [89] [91] have been proposed.

In a more robust fashion, one way to quantitatively achieve true height measurements and avoid damage by tip indentation is by recording amplitude-distance curves at a certain setpoint. Here, the amplitude signal of the oscillating cantilever is determined as a function of the distance between the cantilever and the sample [92]. From these curves, one can detect interaction regimes, i.e. attractive or repulsive forces.

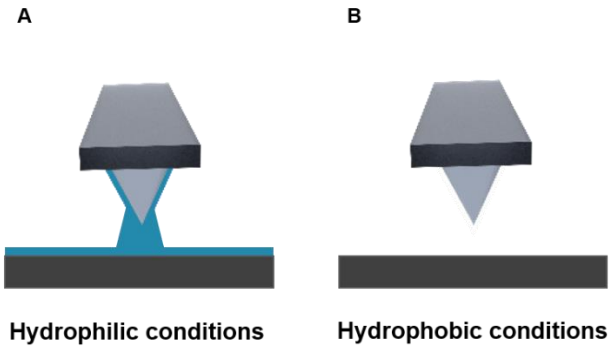

Figure 2.14. AFM measurements in intermittent contact mode (AC mode) under different conditions. (A) AFM performed with a hydrophilic tip and a hydrophilic sample, where a capillary neck is formed. (B) AFM performed with a hydrophobic tip and a hydrophobic sample, where no capillary neck is formed.

The amplitude versus distance curves are normally well-behaved (**Figure 2.15**); for this case, the amplitude is exclusively controlled by long-range attractive forces (**Figure 2.15 A**). Initially, the amplitude is insensitive to tip-sample distance variations. While decreasing the distance, the amplitude decreases as well – almost linearly – till reaching zero. A complex case is a local maximum following a discontinuity (**Figure 2.15 B**). This

can be step-like (**Figure 2.15 B**, red square) or smooth (**Figure 2.15 B**, blue square), and reflects a transition between attractive and repulsive interactions, being the largest separation at which indentation can occur. From this, the attractive regime generally is the best option to achieve true height images of soft samples, as tip-sample forces are usually smaller than in the repulsive regime [93].

Complementary to this, true height measurements can be experimentally obtained at different humidity by avoiding the formation of the capillary neck between the tip and the sample. For this, employing hydrophobic substrates and tips is preferred (**Figure 2.14 B**).

In this thesis, AFM measurements in ambient conditions in air were always performed in AC mode to achieve minimal surface damage. From the instrument insights, height measurements were performed at setpoint ranges and working distances where only the attractive regime was accessed. Finally, the use of hydrophilic and hydrophobic systems was assessed in-depth.

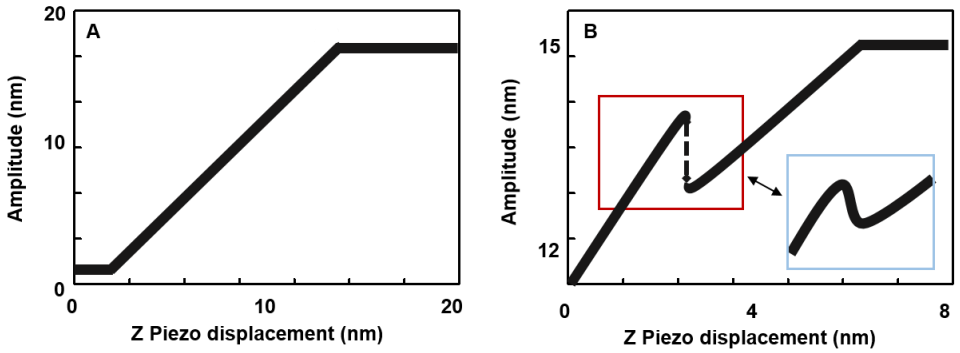

Figure 2.15. Amplitude versus z-piezo displacement curves typically obtained by AFM. (A) The amplitude is controlled by long-range attractive forces. (B) The amplitude exhibits a local maximum due to the competition of long-range attractive and short-range repulsive forces. Note that the local maximum can be step-like (red square) or smooth (blue square)

Chapter 3

Humidity effects on glycosylated gold nanoparticles

In this chapter, the effect of humidity on dimannoside-coated gold nanoparticles is investigated. Dimannoside gold nanoparticles were characterized in solution – by Dynamic Light Scattering – and in air adsorbed on solid surfaces – by Vibrational Sum-Frequency Generation, Fourier Transform Infrared Spectroscopy, Electron Microscopy and Atomic Force Microscopy – and compared against the particle precursors, polyethylene glycol-coated gold nanoparticles. The samples were further studied by Atomic Force Microscopy under hydrophobic and hydrophilic conditions at low, medium and high relative humidity. The hydration ability was evaluated by analyzing differences in maximum heights obtained from the topography images. Regardless of the hydrophobic or hydrophilic condition, the dimannoside gold nanoparticles show water adsorption when increasing the relative humidity. Contrarily, the water adsorption on the particle precursors depends on the nature of the tested condition. This reveals new information of the structural changes taking place on dimannoside-coated gold nanoparticles and offers novel insights into the hydration properties of mannosides in air, from dehydrated state to high humidity.

3.1 INTRODUCTION

Gold nanoparticles (AuNPs) have attracted great interest in biomedical applications due to their ease of synthesis, chemical stability, and unique optical properties [94]. The extreme dependence of the properties on particle size and shape have been demonstrated by working regimes between 10 nm and 100 nm on biological interfaces [95]. However, the limited biocompatibility and high tendency to aggregate in solution inspired new mechanisms of particle bio-functionalization either with proteins, lipids or carbohydrates. Among these, carbohydrate coupling to AuNPs not only results in particle stability and biocompatibility but also allows to study carbohydrate-mediated interactions and the design of novel carbohydrate-based antiviral agents [96] [97]. From a molecular description, glyconanoparticles (GNPs) are water-soluble gold nanoclusters with a 3-dimensional carbohydrate display, small core size, globular shape, chemically well-defined composition, and biological function [49]. Proof of concept studies have demonstrated the great potential of GNPs in glyconanotechnology in solution. However, the behavior of "glycoclusters" in humid environments is poorly known. The importance of such effects is obvious when comparing humidity effects on the transmission of encapsulated viruses as seasonal Influenza [24] or Ebola [98], which share the expression of nanometer surface glycoproteins responsible for virus attachment and fusion to the host cells [99]. Their glycosylation mainly with mannosides should confer also biophysical advantages during transmission. In this direction, GNPs can be regarded as a simple mimic of viral surface glycoproteins – like influenza hemagglutinin (HA) – due to the surface composition, size and controlled orientation on flat surfaces to study locally the effect of humidity on the surface glycans.

Here, a detailed study of individual AuNPs covalently linked to dimannoside residues was performed and compared against AuNPs coated with alkyl-polyethylene glycol (with a carboxylate terminus). Initially the particles were characterized by Dynamic Light Scattering (DLS), Zeta Potential (ZP), Vibrational Sum Frequency Generation Spectroscopy (VSFG), Fourier Transform Infrared Spectroscopy (FT-IR), Scanning Electron Microscopy (SEM), Scanning Transmission Electron Microscopy (STEM) and Atomic Force Microscopy (AFM). The samples were adsorbed on flat inorganic substrates and the water adsorption was measured by AFM under various conditions of relative humidity (RH).

DLS and ZP were carried out to test the particle size and stability in solution, in terms of hydrodynamic diameter and surface charge, respectively. Spectroscopy techniques were used for analysing locally the chemical composition of the organic ligands. FT-IR was tested in the molecular fingerprint infrared (IR) region to find the characteristic peaks of the organic layers whereas VSFG was applied to obtain data on water and hydrogen bonds. SEM was used to measure the particle size, shape and observe the aggregation tendency when adsorbed on inorganic substrates of different hydrophilicity, while staining and STEM enabled to distinguish the organic shell from the gold core.

The main method, however, is AFM. Its advantage is a very detailed image of surface topography, i.e. a height image. This includes also adsorbed water layers on the sample, which differ from the adsorption on the substrate, such that height variations taking place only on the sample are correlated with air humidity [88].

Thin water layers are extremely delicate, and there is a risk to over-interpret AFM height information. Indeed, experiments with soft matter in ambient humidity usually create a thin film of water covering both tip and sample. In hydrophilic systems, if the AFM cantilever approaches the sample surface closely, a mechanical contact occurs between the water films (termed as capillary neck), resulting in apparent heights measurements up to four times larger than actual true heights [89]. Experimentally, this issue can be reverted by different approaches. The height measurements can be achieved at setpoints ranges and working distances where only attractive regimes are accessed in the amplitude-distance curves (**section 2.9**). Finally, the use of surfaces and tips with different hydrophilicity allows to complement topographic information with an accurate height determination. For this, Self-Assembled Monolayers (SAMs) of silanes are excellent model surfaces to assess the water layers contribution on AFM measurements [100]. They form stable and well-defined organic layers on silicon and the surface charge and hydrophilicity can be controlled by selecting the appropriate end groups (**section 1.3.1**).

Here, by performing AFM at different RH, single dimannoside-coated AuNPs (*Dimanno*-AuNPs) were investigated and compared against the particle precursors, alkyl-polyethylene glycol AuNPs (PEG-AuNPs). The particles were tested in hydrophilic and hydrophobic conditions obtained by SAMs of silanes and by using hydrophobic and hydrophilic AFM tips. Specific care was taken for height measurements, as demonstrated by amplitude-distance curves and by statistical analysis (t-tests) while experiments with deuterated water (D_2O) were designed to unveil the mechanism of possible AFM height changes. These methods have the great power to verify claims concerning heights and reproducibility, which are too often merely implicitly assumed. Application of the methods was inspired by a collaboration with the Verdaguer group at Autonomous University of Barcelona [88] and by the biophysical methods employed by the Tong group (Fritz Haber Institute of the Max Planck Society, now Duisburg University) and the Chiantia group (Cell Membrane Biophysics Group at University of Potsdam, see **Chapter 4**).

3.2 MATERIALS AND METHODS

3.2.1 *Materials*

Acetone (99.5 %), 3-(Ethoxydimethylsilyl)propylamine (APDMES, 97 %), and anhydrous solutions of toluene, chloroform, octadecyltrichlorosilane (OTS), and decalin (cis+trans) were purchased from Sigma-Aldrich (Steinheim, Germany). 2-propanol (99.5 %) was obtained from Acros (Geel, Belgium) and absolute ethanol (99 %) from Panreac

(Castellar del Vallès, Spain). Deionized, filtered water (referred as "Milli-Q", specific resistance 18.2 MΩcm^{-1}, TOC (total organic content) < 10 ppb) was obtained by an Advantage System Millipore (Burlington, USA). *Dimanno*-AuNPs and PEG-AuNPs aqueous solutions were kindly provided by the Bio Nano Plasmonics Lab at CIC-biomaGUNE (San Sebastian, Spain) and used as received. The *Dimanno*-AuNPs are thiol-functionalized AuNPs with two ligands, a dimannose targeting ligand (covakently linked to a PEG spacer with a thiol end group), and the unmodified PEG spacer (with its thiol end) as stabilizing component. The PEG-AuNPs bear only the PEGylated component for stabilization of the AuNP core. They are the precursor compound of the *Dimanno*-AuNPs, and used as negative control.

3.2.2 *Synthesis of nanoparticles*

AuNPs were synthesized by the Bio Nano Plasmonics Lab at CIC-biomaGUNE according to [49]. Briefly, both PEG-AuNPs and *Dimanno*-AuNPs were obtained by reduction of Au(III) with $NaBH_4$ in the presence of the target ligands. For the PEG-AuNPs, a carboxylic acid-containing ligand was used, while for obtaining the *Dimanno*-AuNPs 50 % dimannose (Manα1-2Man) ligand was mixed with 50 % of the carboxylic acid-containing ligand. The dimannose and carboxylated linkers are thiol-terminated for binding to the gold nanoparticles (**Figure 3.1**).

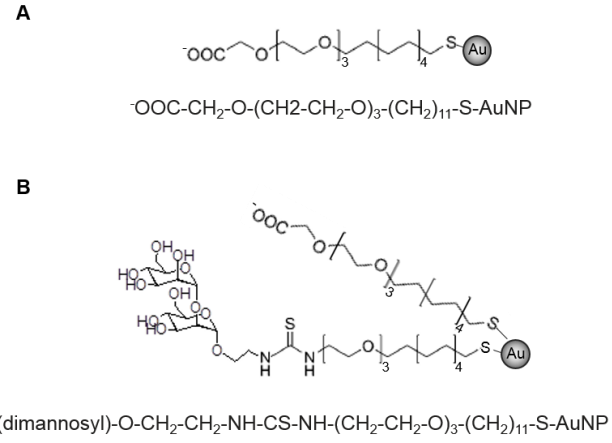

$^{-}$OOC-CH_2-O-(CH2-CH_2-O)$_3$-(CH_2)$_{11}$-S-AuNP

(dimannosyl)-O-CH_2-CH_2-NH-CS-NH-(CH_2-CH_2-O)$_3$-(CH_2)$_{11}$-S-AuNP

Figure 3.1. Structures of gold nanoparticles (AuNPs) used in this work. (A) alkyl-polyethylene glycol AuNPs (PEG-AuNPs) are coated with a carboxyl linker. (B) Dimannoside-coated AuNPs (*Dimanno*-AuNPs) are covered with 50 % of a dimannose-PEG conjugate and 50 % of the carboxyl linker. Note that in (A) and (B) the linear structure of the particles is displayed below the structural scheme. In (B) only the dimannosyl conjugate is displayed.

3.2.3 *DLS and ZP measurements*

DLS was used to determine the hydrodynamic diameter and ZP was applied to estimate the surface charge of the particles in solution with a Zetasizer Nano-ZS (Malvern Panalytical Ltd., Malvern, United Kingdom) equipment. For DLS measurements, 70 μL of the sample (1.0×10^{12} particles/mL) was loaded in a Milli-Q washed micro-cuvette at 25 °C and a detection angle of 173°. For ZP, 700 μL of sample was loaded in a dip-cell cuvette. Three runs were performed in three replicates, resulting in nine measurements per sample. The hydrodynamic diameter (expressed as z average) and the surface charge (expressed as ZP) were calculated with the equipment software (v.7.12, Malvern Instruments Ltd., Malvern, United Kingdom) without any further data processing, hence assuming spherical shapes. For ZP, $f(Ka)$ was considered as 1.5, and the Smoluchowski approximation was used (**section 2.3**).

3.2.4 *Preparation of hydrophilic and hydrophobic substrates*

Dimanno-AuNPs and PEG-AuNPs were adsorbed on silicon wafers previously functionalized with APDMES or with OTS (**Figure 3.2**), referred to as "hydrophilic" or "hydrophobic" functionalization, respectively. The silicon wafers were initially chemically cleaned by successive serial sonication steps of 5 minutes each using acetone, 2-propanol and absolute ethanol, and then dried with a nitrogen stream. Later, oxygen plasma etching (Diener PICO Plasma System, Bielefeld, Germany) was carried out for 8 minutes with 100 W of nominal power, in 1 mbar of oxygen, flow rate 10 sccm, which creates an ultrathin layer (several nm) of hydrophilic silicon oxide (SiO_2).

For the hydrophilic functionalization, the substrates were subsequently immersed in 2 mL of APDMES in toluene (1:100 v/v) and heated to 60 °C for 30 minutes. To avoid the hydrolyzation of the APDMES, the procedure was achieved in a nitrogen-filled glove box. After functionalization, the substrates were rinsed in toluene and dried with a nitrogen stream.

The hydrophobic functionalization was performed as reported in [100]. Silicon wafers were washed first in methanol, then in a 1:1 v/v mixture of methanol and chloroform, and finally in chloroform under 5-minute sonication at every step. Afterwards, the substrates were immersed in a 7:2:1 v/v mixture of decalin (cis+trans)/toluene/chloroform with 0.1 % v/v OTS. The procedure was done at ambient temperature inside a nitrogen-filled glove box. After 12 hours of incubation, the substrates were rinsed with chloroform, then with a 1:1 v/v mixture of chloroform and methanol, and finally with methanol. The process was finished by drying the substrates with a stream of nitrogen.

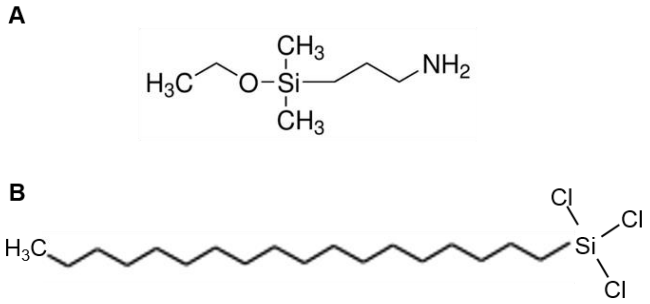

Figure 3.2. Molecular structures of the silanes. (A) 3-(Ethoxydimethylsilyl)propylamine (APDMES). (B) Octadecyltrichlorosilane (OTS).

3.2.5 *Contact angle measurements*

For static contact angle measurements, sessile-drop experiments were performed in triplicates at ambient temperature (23 - 25 °C) with a standard contact angle measurement system (G10 goniometer, Krüss, Germany). A droplet of deionized, filtered Milli-Q water of volume 4 µL was placed onto the functionalized silicon substrates, and contact angles from the drop profile were measured.

3.2.6 *Adsorption of nanoparticles*

Dimanno-AuNPs and PEG-AuNPs were incubated for 5 minutes (1.0×10^{12} particles/mL) on the hydrophilic functionalized silicon substrates. After incubation, the samples were washed with Milli-Q water and dried with a nitrogen stream. The adsorption on the hydrophobic substrates was achieved by drop-casting method. For this, *Dimanno*-AuNPs or PEG-AuNPs were deposited on the substrate and then dried under ambient conditions.

3.2.7 *FT-IR measurements*

FT-IR measurements were achieved with a Hyperion 2000 microscope (Bruker, Madison, USA) with a grazing incidence (GIR) objective lens/mirror system. For this, a concentrated solution of particles (1.9×10^{13} particles/mL) was cast on the surface of a carefully cleaned gold substrate and evaporated under ambient conditions. The measurements were achieved by recording 2000 scans, from 650 to 4000 cm^{-1} and a resolution of 4 cm^{-1}, by triplicate measurements. Background spectra were recorded on gold areas outside the evaporated droplet. The FT-IR spectra were obtained with the

equipment software OPUS v.6.5 (Bruker, Madison, USA) without any further data processing.

3.2.8 *VSFG measurements*

VSFG spectra of *Dimanno*-AuNPs and PEG-AuNPs was recorded on a broadband VSFG system at Fritz Haber Institute of the Max Planck Society in Berlin, Germany. Gold thin films (200 nm on 10 nm Cr on glass) were used as substrates. Previously to sample deposition, the substrates were cleaned with ethanol, and Milli-Q water under sonication for 10 minutes. UV/ozone cleaning was applied to remove any possible hydrocarbon contamination, and the VSFG spectra of the washed gold was used as reference to normalize the non-flat IR power distribution, similar to FT-IR recording. About 10 μL of the sample was drop-cast on the substrate and evaporated under nitrogen flow. The VSFG experiments were achieved under dry air flushing at ambient temperature (24 °C) with four different center frequencies to measure the complete CH and OH stretching region in the broad band IR. The tunable IR laser produced femtosecond pulses of ~ 5.5 mW (at 3300 cm^{-1}). Its focus length was 30 cm and the incident angle 45°. The visible picosecond pulses were at a fixed frequency of 800 nm (12500 cm^{-1}), and of 10 mW power. Their focus length was 100 cm and the incident angle 65°. The sum frequency signal was collected in reflection, accumulated for 1 min for ppp polarization (all beams polarized in the incident plane) and 2 min for ssp (laser beams polarized perpendicular to the surface and sum frequency emission polarized in the incident plane).

3.2.9 *Electron Microscopy imaging*

SEM and STEM images were obtained in a Helios NanoLab 450S dual beam microscope (FEI Systems, Columbia, USA). SEM images were recorded from adsorbed *Dimanno*-AuNPs and PEG-AuNPs at 5 kV with 50 pA current in high vacuum mode. The core diameter of single particles was manually counted with ImageJ [101]. The number of particles was expressed as "n" and the data were displayed as the mean ± standard deviation (SD). A total of 378 particles were counted for the *Dimanno*-AuNPs and 491 for the PEG-AuNPs.

STEM acquisition was achieved in high vacuum at 30 keV on negatively stained *Dimanno*-AuNPs samples. For the negative staining, 0.35 μL of *Dimanno*-AuNPs (1.9×10^{13} particles/mL) were deposited on glow discharged carbon grids (air flow, 20 mA, 4 minutes). Then, 0.35 μL uranyl acetate (0.5 % w/w) was deposited and dried on the sample.

3.2.10 *AFM measurements*

AFM topography images were achieved by using an Agilent 5500 AFM (Keysight, Santa Clara, USA). Images were recorded in air in tapping mode at 24 °C, at speed rates between 0.8 and 1.2 lines per second. The scanning was performed in at least six replicates for the PEG-AuNPs and nine replicates for the *Dimanno*-AuNPs at each examined substrate and humidity condition.

Silicon cantilevers (Multi-75, Budget Sensors, Sofia, Bulgaria) with spring constants (k) of 3 N/m, resonance frequencies (f) of 75 kHz and nominal radii of < 10 nm were used for the experiments on the hydrophilic substrates. These conditions are referred to as "hydrophilic conditions". Prior to taking topography images, amplitude versus distance curves were obtained as a function of the free amplitude (A_0 = 4 V) at setpoint 2.2 V and drive amplitude 1.2 % at (15 ± 5) % of RH and at setpoint 1.9 V and drive amplitude 6 % (90 ± 5) % of RH. Measurements were achieved by triplicate at 3.7 μm/second rate.

The visualization of particles on hydrophobic substrates was achieved by employing gold-coated silicon probes with a 1 nm carbon spike (k = 5 N/m, f = 160 kHz, Hi'Res-C14 /Cr-Au, MikroMasch, Sofia, Bulgaria). These conditions are referred to as "hydrophobic conditions".

The samples were incubated in the hydrophilic or hydrophobic substrates, and AFM topography images were taken under humidity-controlled atmospheres at (15 ± 5) %, (50 ± 5) % and (90 ± 5) % of RH. These humidity conditions are referred to as "low humidity", "medium humidity" and "high humidity", respectively. For this, an environmental isolation chamber (Keysight, Santa Clara, USA) was mounted to the AFM, thus providing a completely sealed and isolated environment. The RH of (15 ± 5) % was achieved by pumping nitrogen into the isolation chamber. The RH of (50 ± 5) % was reached by controlling the mixing ratio between a dry and a wet (water-saturated) stream of nitrogen. The RH of (90 ± 5) % was prepared as in the previous case, but the sample was allowed to equilibrate overnight in the water-saturated chamber.

The images were examined by using picoView 1.14 software (Keysight, Santa Clara, USA). AFM images were analyzed after scanning with WSxM 5.0 Develop software version 8.4 [102] for obtaining the maximum height of the particles and height profiles. For this, the images were processed by levelling the plane of the image and applying parabolic flattening. Around 500 individual particles were processed in the hydrophilic conditions and 250 in the hydrophobic conditions at each examined humidity condition. The particles were manually selected by applying a criteria of single particle observation with a full width at half maximum (FWHM) below 30 nm and 40 nm for the hydrophilic and hydrophobic conditions, respectively. Gwyddion software version 2.47 (Gwyddion, Brno, Czech Republic) was used for displaying the topography images. The images were first levelled by mean plane subtraction, aligned by height median, and occasionally z-excursions (outliers) were manually removed by e.g. correction of the scan line artefacts in the x-axis or misaligned segments within a single row. The height distribution histograms

were performed with Origin(Pro) 8.0 software (OriginLab Corporation, Northampton, USA) and height profiles were obtained with GraphPad Prism version 8.0.1 for Windows (GraphPad Software, San Diego, USA). The number of particles was expressed as "n" and the data were displayed as the mean ± SD.

3.2.11 *Statistical analysis*

Statistical analysis was performed using GraphPad Prism version 8.0.1 for Windows. Data sets were analyzed by unpaired t-tests (Mann-Whitney test) for comparing the same particles on different substrates at the same humidity. In all the cases two tailed P-values were reported, with a confidence level of 0.05 – 0.01.

3.3 RESULTS

3.3.1 *Analysis of the chemical groups*

Initially, the nature of the coating layer of the functionalized AuNPs, namely PEG-AuNPs and *Dimanno*-AuNPs was characterized by FT-IR and VSFG.

From the FT-IR spectra (**Figure 3.3**) the PEG-AuNPs showed the characteristic absorption bands of the PEG polymer [103][104]; they can also be very well compared to EG chains of the same length, triethylene glycol, for which we chose the dimethyl ether, for its similarity with the PEG-AuNPs shell.

The band at 950 cm^{-1} (origin unknown) is well resolved, while the strongest band at 1110 cm^{-1}, based on asymmetric C-O-C stretching, appears only as a shoulder. The band at 1260 cm^{-1} can be assigned to the very strong signal from C-O stretching in COOH (protonated carboxylate) [105], although there are rather few COOH groups in the particle, compared to other functional groups. The remainder of the fingerprint region is masked by H_2O (apparent as "noise" from 1350 to 2150 cm^{-1}) and CO_2 (2350 cm^{-1}) in the gas phase. The second strongest band at 2880 cm^{-1} is based on C-H stretching in the CH_2 groups. This band has a sub-structure, based on symmetric and asymmetric stretching, which is usually not resolved in EGs. Signals at higher energy are again apparent noise from H_2O vapor. There is no trace of OH groups, which are sometimes present due to unwanted hydrolysis (O-H stretching at ~ 3500 cm^{-1}), or from adsorbed water (H-O-H bending at 1625 cm^{-1}). These bands are found in liquid water, but also in impure or not completely dried compounds. A good example is triethylene glycol dimethyl ether (also known as 1,2-bis (2-methoxyethoxy) ethane) from the National Institute of Advanced Industrial Science and Technology (AIST) spectral library [106].

The *Dimanno*-AuNPs showed a very different spectrum. Although the same alkyl-PEG derivate chains should contribute, the alkyl-PEG-thiourea-dimannosyl shell totally dominates, as explained in the following: The band at 1050 cm^{-1} cannot easily be assigned,

while 1120 cm^{-1} is again from C-O-C stretching [107]. This low-energy fingerprint region is thus based on PEG and alkyl chains, present everywhere on the nanoparticle surface. 1650 cm^{-1}, however, is assigned to H-O-H bending from adsorbed or absorbed water. Because we can exclude this on the pure alkyl-PEG shell (see above), we assign these water molecules to the dimannose residues. Indeed, sugars are very difficult to dry completely, such that this band is easily found in many carbohydrates [108]. The spectrum shows again a band from CO_2 in the gas phase. The C-H stretching region is rather different, though, with two bands at 2850 cm^{-1} (symmetric C-H) and 2920 cm^{-1} (asymmetric C-H). These positions are typical for alkyl chains, but are also found in carbohydrates [109] [110] [111].

The main feature of the spectrum is a very broad and extremely intense feature of two overlapping bands at 3250 cm^{-1} and 3400 cm^{-1}, O-H stretching in hydrogen bonds. While adsorbed or absorbed water can also contribute here, this feature is safely assigned to the dimannoside OH groups. Finally, the band at 3700 cm^{-1} is also from O-H stretches, but from free (not hydrogen-bonded) OH groups. It is furthermore noteworthy that the thiourea group does not result in any strong bands (expected at 1500 cm^{-1} and 1550 cm^{-1}) as deduced from dialkyl thiourea spectra in the AIST database [106].

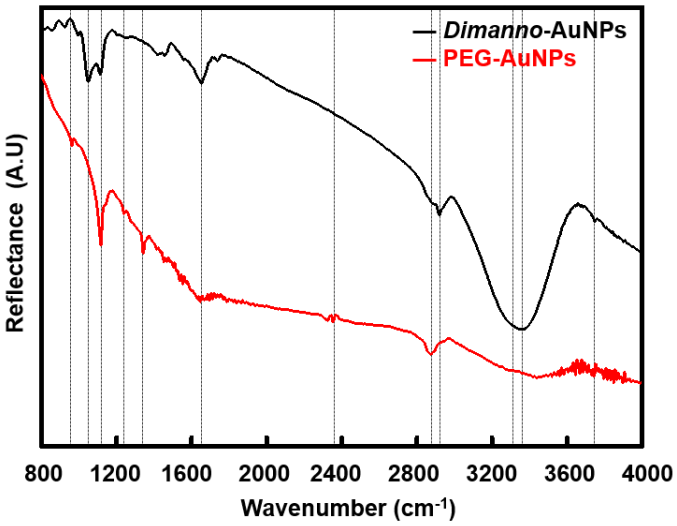

Figure 3.3. Infrared (IR) spectra of *Dimanno*-AuNPs and PEG-AuNPs recorded by Fourier Transform Infrared Spectroscopy (FT-IR) in grazing incidence (GIR) mode on gold substrates. The black line represents the IR spectra of *Dimanno*-AuNPs, the red line represents the IR spectra of PEG-AuNPs. Note that the vertical lines indicate the characteristic IR peaks at 950 cm^{-1}, 1050 cm^{-1}, 1110 cm^{-1}, 1260 cm^{-1}, 1350 cm^{-1}, 1650 cm^{-1}, 2350 cm^{-1}, 2850 cm^{-1}, 2920 cm^{-1}, 3250 cm^{-1}, 3400 cm^{-1} and 3700 cm^{-1}.

For the VSFG, the ssp-polarized spectra were obtained by adding a droplet of H_2O or D_2O on the dried samples and subsequent evaporation (**Figure 3.4 A** and **B**). The VSFG spectra focus on the high frequency region only. The vibrational bands are superimposed on a very broad signal from bulk gold, which is quasi constant after normalization (similar to FT-IR). In contrast to FT-IR, the bands stem only from vibrations at interfaces, i.e. gold/air interfaces, hence from the surface of the AuNPs. Additionally, highly symmetric vibrations are forbidden (have very low or zero intensities). **Figure 3.4 A** compares both PEG-AuNPs and *Dimanno*-AuNPs, recorded in dry air.

The PEG signals correspond, as expected, quite well to the IR spectrum, with a strong peak at 2880 cm^{-1}. This feature points to asymmetry, which should be based on disorder of the PEG chain (ordered alkyl chains, for example, yield no VSFG signal from CH_2). Moreover, the peak is unusually broad, possibly due to the complex shape of the disordered PEG-alkyl chain. However, the disorder is only present in each chain; altogether the C-H stretching vibrations must have a preferred orientation with respect to the gold substrate. In other words, the nanoparticle has a non-symmetric environment, which can simply be the presence of the gold substrate. The noise-like feature around 3400 cm^{-1} is assigned to liquid water, as features above 3600 cm^{-1} should indicate water vapor traces. This is a proof that water is adsorbed on the PEG-AuNPs. A quantification is not possible; however, it cannot be more than very few (mono)layers, else the band would totally dominate the spectrum. This is also in agreement with the absence of the band in FT-IR. Hence, the hydrophilic PEG chain binds water, but can easily be dried, while the last traces remain. This is quite similar to the idea of a strongly bound water (mono)layer on biomolecules.

The *Dimanno*-AuNPs, under exactly the same conditions, exhibit a very different spectrum: The C-H stretching bands at 2850 cm^{-1} and 2920 cm^{-1} (see also FT-IR) are "negative", the C-H vibrational signal is destructively interference with the background signal of the gold substrate [112]. The frequency is only little shifted from those of CH_2 groups in alkyl and PEG chains, so the contribution of the CH groups in the dimannose residues is rather weak. By the symmetry rules, and by the ssp-polarization, one can deduce that the CH_2 groups are again oriented, but different from those in the PEG-AuNPs. This shows directly that the dimannoside exerts a strong effect on the PEG and alkyl chain conformation. Based on the rather narrow bands, we can exclude disorder, and propose a stretched-out geometry. The dimannose must be covered by water, and indeed again a peak assigned to liquid water is present. Water on the dimmanoside can adsorb in a multitude of orientations. Their average means high symmetry and low signal. **Figure 3.4 C** provides a sketch of the principal ideas.

VSFG experiments were repeated after exposure to D_2O. Working with D_2O usually assess the exchange capability of the hydroxyl groups in IR frequencies between 3100 and 3700 cm^{-1}. Also, the slower structural dynamics at the air/D_2O interface allow visualizing

better signals related to the air/H_2O interface on the particles [13] and enable finding whether there are ordered water molecules at the sample surface.

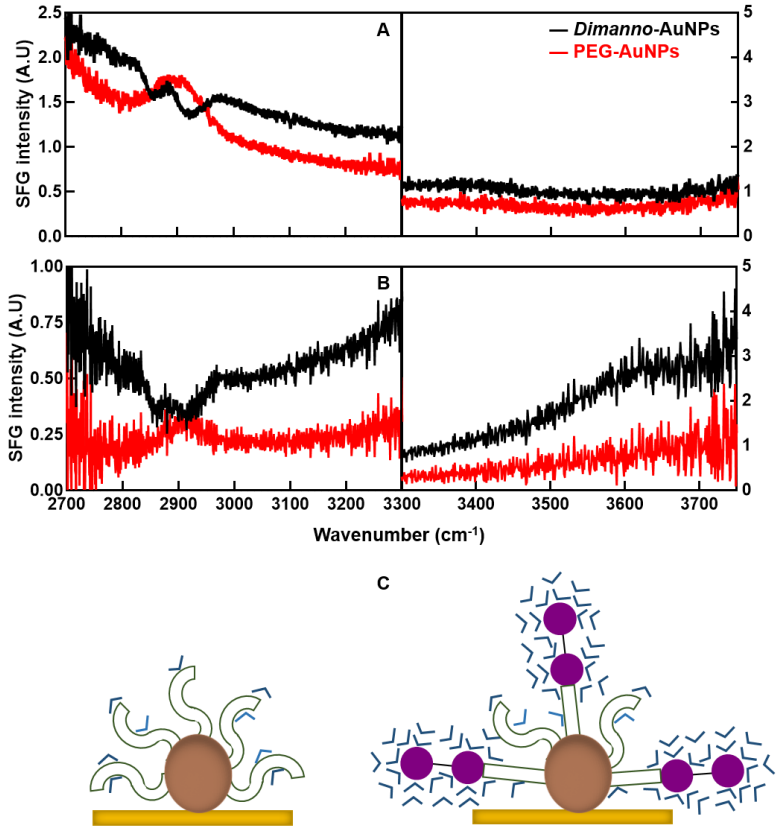

Figure 3.4. Normalized Vibrational Sum Frequency Generation Spectroscopy (VSFG) spectra in CH and OH region of *Dimanno*-AuNPs and PEG-AuNPs on gold substrate, ssp (s-VSFG, s-vis, p-IR) polarization combinations. (A) VSFG spectra after exposure to H_2O. (B) VSFG spectra after exposure to D_2O. The black line represents the VSFG spectra of *Dimanno*-AuNPs, the red line represents the VSFG spectra of PEG-AuNPs. Note the different y-axis scale. (C) Model of the proposed conformations of *Dimanno*-AuNPs and PEG-AuNPs. PEG-AuNPs (left) show a low-ordered geometry of the PEG chains. *Dimanno*-AuNPs (right) show a stretched-out geometry provided by the dimannose residues. The brown circles represent the gold core, the flexible S-like green structures represent the PEG ligand, the rigid green lines represent the PEG ligand ordered by the presence of dimmanose residues, the violet circles represent the dimmanose residues and the V-like blue lines the adsorbed water. Note that the organic layers are not scaled and are enlarged with respect to the gold cores.

In this experiment, the D_2O exposure time of 30 minutes is not sufficient to exchange the H in the dimannose OH groups [113]. But it should replace, due its large excess, the thin layers of adsorbed water. **Figure 3.4 B** shows that this is indeed the case, the CH region is practically unchanged, while the 3400 cm^{-1} signals are barely present. Note that the O-D stretch in liquid D_2O is shifted to 3500 cm^{-1}. In this way, the model of thin adsorbed water layers is bolstered, also showing the strongly hydrophilic nature of both PEG-AuNPs and *Dimanno*-AuNPs.

3.3.2 *Particle size and shape*

The particle size and the stability in aqueous solution was characterized by DLS and ZP, while the size and morphology in completely dry conditions was measured by Electron Microscopy.

The size distribution obtained by the hydrodynamic diameter (**Figure 3.5**) of the PEG-AuNPs was 67.7 ± 9.4 nm (z average) with a major peak at 41.1 ± 4.2 nm and a polydispersity index (PDI) of 0.35. These results indicated that the sample was slightly polydisperse in nature. Contrarily, the z average of the *Dimanno*-AuNPs was 30.4 ± 1.1 nm with a major peak of 16.8 ± 0.9 nm. The peak value – which represents more accurately the particle size [114] – was in coherence with the hydrodynamic diameter of the individual particles in solution (PDI 0.29), thus indicating that the dimannose coating provided less nanoparticle aggregation. In both cases, an additional weak peak with a maximum around 5000 nm was noticed, which was more pronounced on the PEG-AuNPs. This was possibly due to large aggregate species [114], which diminished by adding dimannose residues. The presence of nanobubbles [115] or external contamination may also explain this peak, as scattering from large aggregate species may lead to data over interpretation. In this direction, since the scattered intensity is not proportional to the number of particles but to the volume, extremely low concentration of micrometer size particles can result in a size distribution peak in the micrometer range (**section 2.2**).

The surface charge of the particles in water at pH ~ 7 was in both cases around - 20 mV. These values agree well with data from similar particles [104]. The isoelectric point of carboxylate-PEG-capped particles is ~ 2.5, so around pH 7 they should exhibit a negative ZP. This is also compatible with a low content of carboxylate, as citrate-capped AuNPs (with a higher concentration of carboxylate) exhibit at the same pH a lower ZP (~ - 45 mV) [116].

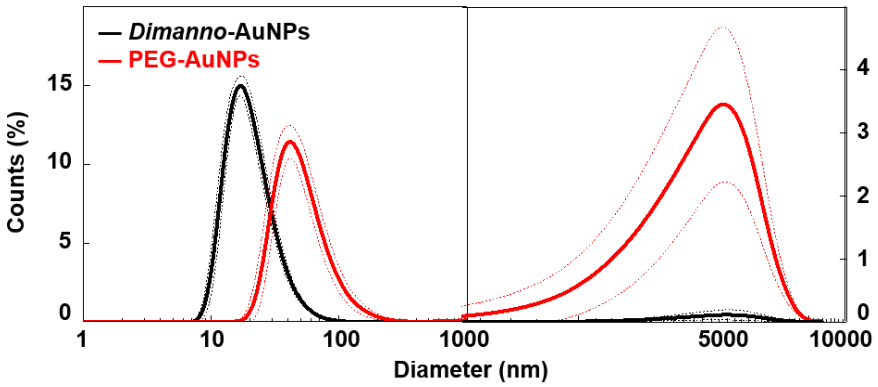

Figure 3.5. **Hydrodynamic diameter distributions of *Dimanno*-AuNPs and PEG-AuNPs obtained by Dynamic Light Scattering (DLS).** The black line represents the size distribution of *Dimanno*-AuNPs, the red line represents the size distribution of PEG-AuNPs. Continuous line indicates the mean, dashed lines indicate the standard deviation (SD). Note the different y-axis scale.

SEM was applied to evaluate the particle size and morphology in high vacuum (completely dried samples). The technique is useful for achieving a detailed visual image of the particles with high quality and spatial resolution in the nanometer range. Although usually it cannot measure thickness or heights of the sample specimens, it can provide detailed information about the morphology, composition and structure of the materials with great precision. In this work, > 3 kV acceleration voltage, together with standard detection of secondary electrons (low energy, << 1 kV) detects only electrons from the surface region of the sample (i.e. wafer and NPs). At the same time, the sensitivity for the organic layer is very low, such that only the gold particle cores are visualized. By adjusting a Gaussian fitting to the size histograms (**Figure 3.6**), the average diameter of the particle cores adsorbed on APDMES on silicon was estimated. The *Dimanno*-AuNPs exhibited a mean size of 14.8 ± 1.6 nm (**Figure 3.6 A** and **C**) and the size of the PEG-AuNPs was 14.3 ± 1.5 nm (**Figure 3.6 B** and **D**).

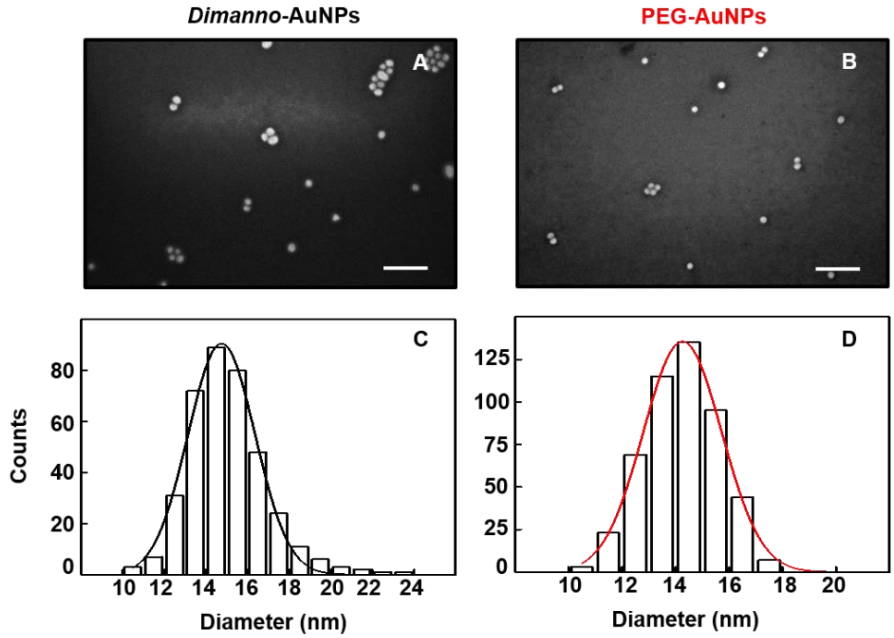

Figure 3.6. Representative Scanning Electron Microscopy (SEM) images of *Dimanno*-AuNPs and PEG-AuNPs adsorbed to a hydrophilic substrate. (A) *Dimanno*-AuNPs. (B) PEG-AuNPs. (C and D) Particle size histograms (diameter) from (A and B) respectively. Scale bars correspond to 100 nm.

As the organic layers from PEG and dimannose are transparent to electrons in SEM (only the gold cores were observed as bright features), images were also recorded from negatively stained *Dimanno*-AuNPs. Essentially, in negative staining methods, a soluble heavy metal salt is used to surround, support and permeate any aqueous or hydrophilic part of the organic coating. After drying, a thin film of stain embeds the material, and renders also the organic coating electron-dense [117]. This effect is quite clear in transmission (bright field, primary beam collected on centered disk in STEM), but ideally used with scattering (dark field, scattered electrons counted on the STEM ring detector). In this investigation, the *Dimanno*-AuNPs deposited on a carbon grid were negatively stained with uranyl acetate and were imaged in bright field and dark field modes. Our data is in agreement with similar research by del Pino et al., on uranyl acetate stained PEG-AuNPs and observed by Transmission Electron Microscopy (TEM) in bright field mode: "*The heavily electron-scattering uranium acts as a negative staining contrast agent by mainly adsorbing everywhere on the sample-supporting carbon film, except in places which already became occupied by protruding matter. Ideally it deposits as a monolayer on the unoccupied carbon film surface and slightly accumulates along topographical edges of the sample. It thus in the TEM image would render the formerly by sample unoccupied area grayish and line topographical edges of the sample*

darker" [118]. In analogy to this interpretation, in the bright field STEM images presented here, the gold cores of the nanoparticles appear nearly black. Due to the organic nature of the dimannose shells, they appear contrasted against the grey background of the carbon grid, as a bright thin rim around the particle cores. In this way, both core and shell of the particles are distinguished from the supporting carbon film. The same is detected in dark field images, where the color of the observed features is the opposite. From the images, the estimated organic layer thickness is 1.5 nm (**Figure 3.7**). This was obtained by subtraction of the total radius of the negatively stained particles and the radius of the gold cores [118].

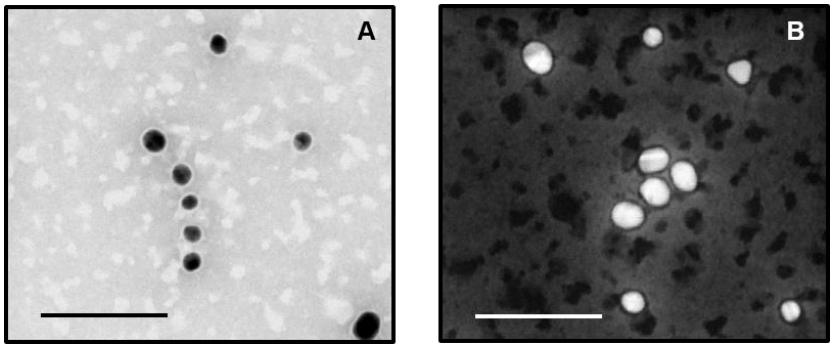

Figure 3.7. Scanning Transmission Electron Microscopy (STEM) images on negative stained *Dimanno*-AuNPs adsorbed to a holey carbon grid. (A) Image acquired in bright field mode. (B) Image acquired in dark field mode. Note that the inhomogeneous background corresponds to the interaction between the uranyl acetate and a holey carbon grid. Scale bars correspond to 100 nm.

3.3.3 *Adsorption on hydrophilic and hydrophobic substrates*

After particle characterization in solution and in dehydrated conditions, the aggregation tendency of the samples was assessed by SEM and AFM and detailed information on the spatial distribution of the samples (lateral and vertical) was extracted.

Silane-coupling agents APDMES and OTS were used to modify the silicon substrates before sample adsorption (**section 3.2.4**). Prior to sample deposition, the contact angle of Milli-Q water on the APDMES silicon was 66 ± 3° while on the OTS silicon it was 92 ± 2°, indicating a good development of a hydrophilic and a hydrophobic substrate, respectively, at the microscale (**section 2.1**).

In both cases, the silane-coupling agents enabled particle adsorption. Still, the phenomena occurred differently depending on the nature of the substrate (**Figure 3.8**) as also reported in analogous investigations with tobacco mosaic virus [84] and surface-layered proteins [100].

The *Dimanno*-AuNPs showed a homogenous distribution of individual particles on the hydrophilic substrates, with few particle clusters (**Figure 3.8 A-C**). SEM images at the microscale were uniform and exhibited no differences in contrast (**Figure 3.8 A**). At a smaller scale, the images presented a homogenous dispersion of the particles which correlated well with the observations at the microscale (**Figure 3.8 B**). This was also supported by AFM topography images at the nanoscale. The local surface characterization and height measurements showed uniformly dispersed particles and 2-dimensional adsorption (**Figure 3.8 C**). Contrarily, PEG-AuNPs were not well dispersed and in general, more agglomerates were found (**Figure 3.8 G-I**). The electron micrographs at the microscale showed differences in contrast, which could be assigned to inhomogeneous particle adsorption. Brighter features may be related to particle clusters forming micrometer size islands (**Figure 3.8 G**). At a smaller scale, the images agree with this principle, as some areas show highly concentrated particles, while others only the background from the substrate (**Figure 3.8 H**). In AFM the same trend is observed: The particles tend to agglomerate in ordered structures rather than disperse homogeneously on the substrate surface (**Figure 3.8 I**).

On the hydrophobic substrates (**Figure 3.8 D-F** and **J-L**), the drop-casting method applied for particle deposition resulted in a "coffee ring effect". The phenomenon refers to the drying of a liquid droplet with suspended particles on a solid surface, which leaves a ring-shaped structure along the droplet perimeter [119]. In this direction, both AuNPs were highly concentrated on the rim of the dried droplet and local inhomogeneities were found inside and outside the droplet (**Figure 3.8 D** and **J**). From SEM and AFM images outside the droplet, more negligible adsorption and higher particle agglomeration was observed (**Figure 3.8 E, F, K** and **L**) with respect to the hydrophilic conditions. Still, sample deposition of PEG-AuNPs was even less uniform than for *Dimanno*-AuNPs.

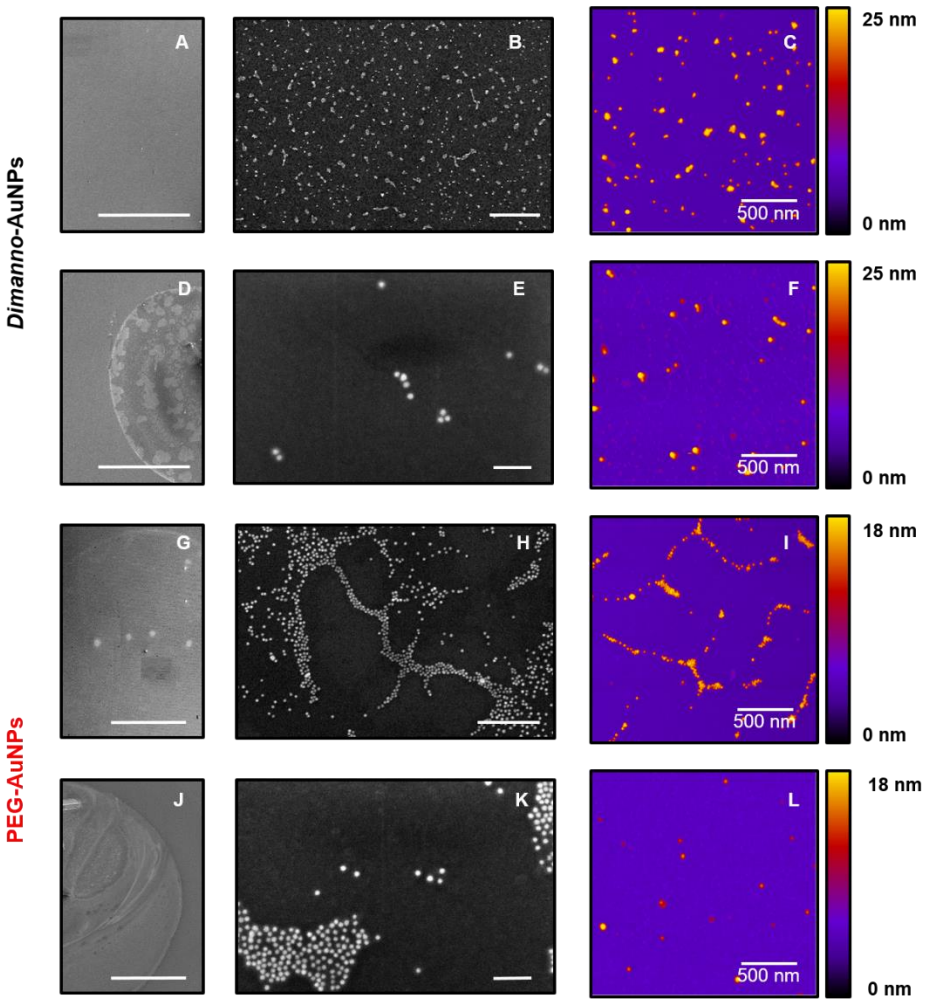

Figure 3.8. SEM and Atomic Force Microscopy (AFM) images of *Dimanno*-AuNPs and PEG-AuNPs on hydrophilic and hydrophobic substrates. (A, B, D, E, G, H, J and K) SEM images. (C, F, I and L) AFM images. (A-C) *Dimanno*-AuNPs adsorbed to a hydrophilic substrate. (D-F) *Dimanno*-AuNPs adsorbed to a hydrophobic substrate. (G-I) PEG-AuNPs adsorbed to the hydrophilic substrate. (J-L) PEG-AuNPs adsorbed to the hydrophobic substrate. (A, D, G and J) Scale bars correspond to 400 μm. (B and H) Scale bars correspond to 500 nm. (E and K) Scale bars correspond to 100 nm. Note that the hydrophilic substrate was obtained by functionalization of a silicon wafer with APDMES. The hydrophobic substrate was obtained by functionalization of a silicon wafer with OTS.

3.3.4 *AFM scanning in water vapor*

Local surface characterization of single particles was performed by AFM under different RH. Topography images were obtained at three different hydration conditions, namely 1) low humidity on dehydrated samples at (15 ± 5) % RH; 2) medium humidity achieved at (50 ± 5) % RH and 3) high humidity obtained on incubated samples overnight at (90 ± 5) % RH. The measurements were performed under hydrophilic as well as hydrophobic conditions (**sections 3.2.4** and **3.2.6**). Under these conditions, topography images were taken at the three different hydration conditions and the maximum height (z_{max}) of individual particles, randomly selected, was obtained.

The experiments on the hydrophilic conditions were achieved by testing the hydrophilic substrates and by performing the AFM tests with a silicon tip. The vertical resolution (Δz) of the cantilever was 0.04 nm and the surface roughness of the APDMES on silicon was on average 0.16 nm estimated on images of 1 x 1 μm^2 (**section 2.9**). This indicated a homogenous and flat SAM before sample deposition. Amplitude versus distance curves (**Figure 3.9**) suggested working regimes controlled by long-range attractive forces (**section 2.9**), both at low (~ 15 % RH) and high humidity (~ 95 % RH). Under these conditions, tip indentation was avoided, and minimum sample damage was assured.

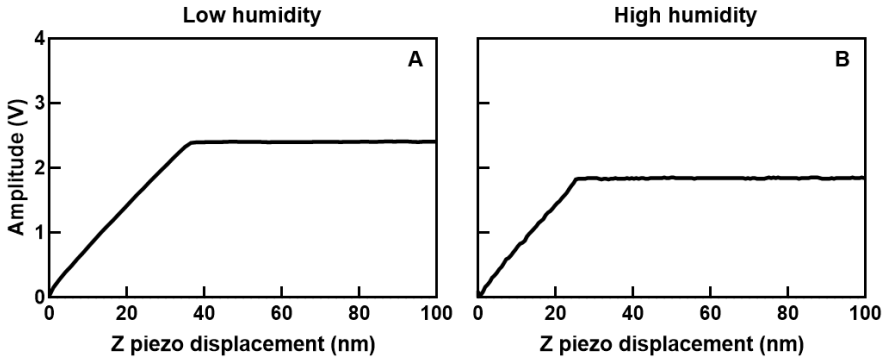

Figure 3.9. Cantilever oscillation amplitude versus z-piezo displacement on hydrophilic conditions obtained by AFM. (A) Representative curve obtained at low humidity (~ 15 % relative humidity, RH). (B) Representative curve obtained at high humidity (~ 95 % RH). Note that in both cases the free amplitude (A_0) was 4 V, which corresponds to the maximum value in the display chart.

Scanning at different humidity resulted in variations in z_{max} of the single particles. This was proved by imaging an individual particle over the three humidity conditions and analyzing the height profile. Due to sample drift and geometrical convolution (or tip dilation) provided by the tip radius (< 10 nm), we only focus on the analysis of height variations and not on diameter changes. Of note, geometrical convolution occurs when the

radius of the tip is comparable to the dimensions of the surface features being imaged, resulting in a significant discrepancy between the true width of the real features and that observed in an AFM image [86].

For the *Dimanno*-AuNPs the z_{max} of the selected single particle at low humidity (~ 15 % RH) was 15.6 nm (**Figure 3.10 A** and **Figure 3.11 A**). By modulating the humidity to ~ 50 % RH, the particle did not significantly increase in z_{max}, with a value of 15.8 nm (**Figure 3.10 C** and **Figure 3.11 C**). More significant differences were found after sample incubation at high humidity (~ 95 % RH) when the height profile of the particle showed a maximum of 17.7 nm (**Figure 3.10 E** and **Figure 3.11 E**). The height difference between high and low humidity was 2.1 nm (**Figure 3.11 G**).

In contrast, when testing single PEG-AuNPs under the same conditions – in this case, two individual particles – the z_{max} decreased upon humidity increment. At low humidity, the particles presented a z_{max} of 13.3 nm and 12.9 nm (**Figure 3.10 B** and **Figure 3.11 B,** left and right respectively), at medium humidity a decrease to 12.4 nm and 11.9 nm was noticed (**Figure 3.10 D** and **Figure 3.11 D**, left and right respectively). In comparison, the z_{max} at high humidity were 12.0 nm and 11.9 nm, respectively (**Figure 3.10 F** and **Figure 3.11 F**). Overall, both particles decreased in height 1.3 nm and 1.0 nm, respectively, upon humidity increment (**Figure 3.11 H**).

To increase the statistical accuracy of the experiment, individual particles randomly selected were tested under the same humidity conditions. About 500 particles were analyzed and the z_{max} were obtained (**Figure 3.12 A** and **C**, **Table 3.1**). The resulting box plots for the hydrophilic conditions correlated well with previous analysis on single particles (**Figure 3.10, Figure 3.11**). At low humidity, the z_{max} of *Dimanno*-AuNPs was 16.7 ± 1.6 nm (n = 504); at medium moisture, an increase of ~ 2.5 % was observed (n = 532), and at high humidity level, the overall increase was ~ 9.0 % (n = 492, **Figure 3.12 A**) concerning the initial value. PEG-AuNPs reflected general reduction with respect to the initial value at low humidity (**Figure 3.12 C**). At this humidity, the particles presented a z_{max} of 13.3 ± 1.0 nm (n = 505); at medium humidity level, the particles decreased ~ 1 % in height (n = 495), and at high humidity ~ 2.5 % relevant to the initial values (n = 499). These results were within the uncertainties of the experiment.

The analysis of the chemical groups (**section 3.3.1**) gave already a good indication for the presence of H_2O on the dimannose ligands, varying with RH, and the data obtained by AFM confirm this. Yet, to prove that the increase in the z_{max} was solely due to the adsorbed water layers on the particles, the same procedure was performed under hydrophobic conditions. From this, one can exclude that the observed phenomena are specific for the type of substrate [120] or come from mechanical contact between the tip and the substrate [89] [92].

Silane-coupling OTS was used for substrate functionalization and AFM images were achieved with a silicon tip with a hydrophobic carbon spike. The Δz for the cantilever in ambient conditions was 0.03 nm and the roughness of the OTS on silicon was on average

0.55 nm estimated from images of 0.2 x 0.2 μm². In this case, it was not possible to follow the same particles along the different humidity steps due to the instability of the measurement, which did not allow to find the same area again (after changing the humidity). However, about 250 measurements of single particles were achieved on random positions (**Figure 3.12 B** and **D, Table 3.1**). The data at different humidity showed comparable results on the *Dimanno*-AuNPs with respect to the hydrophilic conditions. An increase in the z_{max} of ~ 11.0 % was detected from low to high humidity (**Figure 3.12 B**). In contrary, the results of the PEG-AuNPs on hydrophobic conditions were slightly different from the hydrophilic data. When varying humidity from low to high, the particles increased ~ 6.0 % in the z_{max} (**Figure 3.12 D**).

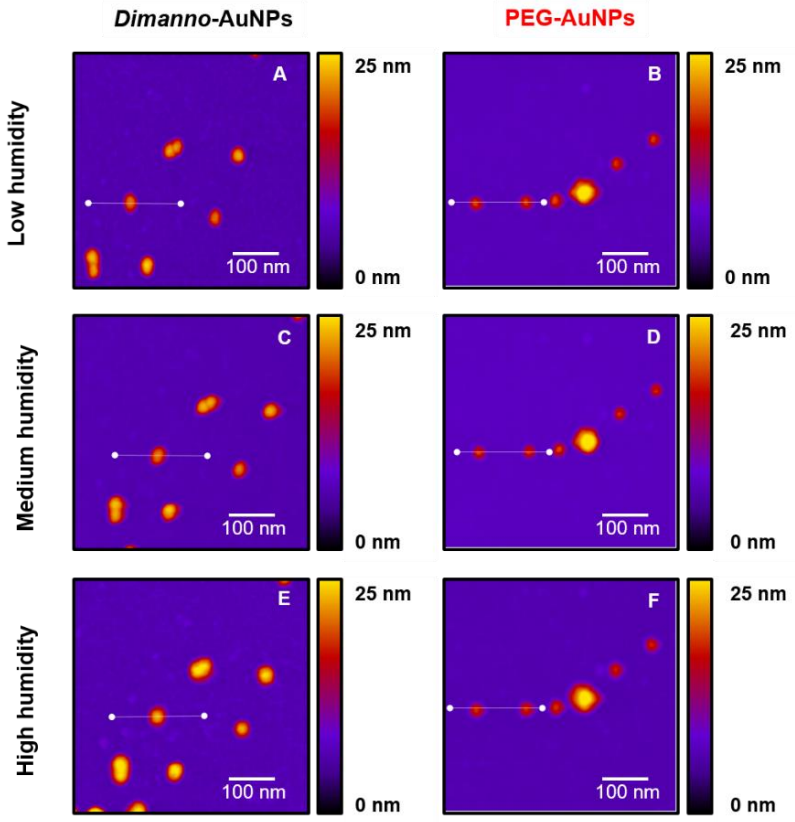

Figure 3.10. Representative AFM topography images and height profiles of *Dimanno*-AuNPs and PEG-AuNPs on hydrophilic conditions obtained at different humidity. (A and B) Particles at low humidity. (C and D) Particles at medium humidity. (E and F) Particles at high humidity. (A, C and E) *Dimanno*-AuNPs; (B, D and F) PEG-AuNPs. Note that low humidity refers to ~ 15 % RH, medium humidity refers to ~ 50 % RH and high humidity refers to ~ 90 % RH.

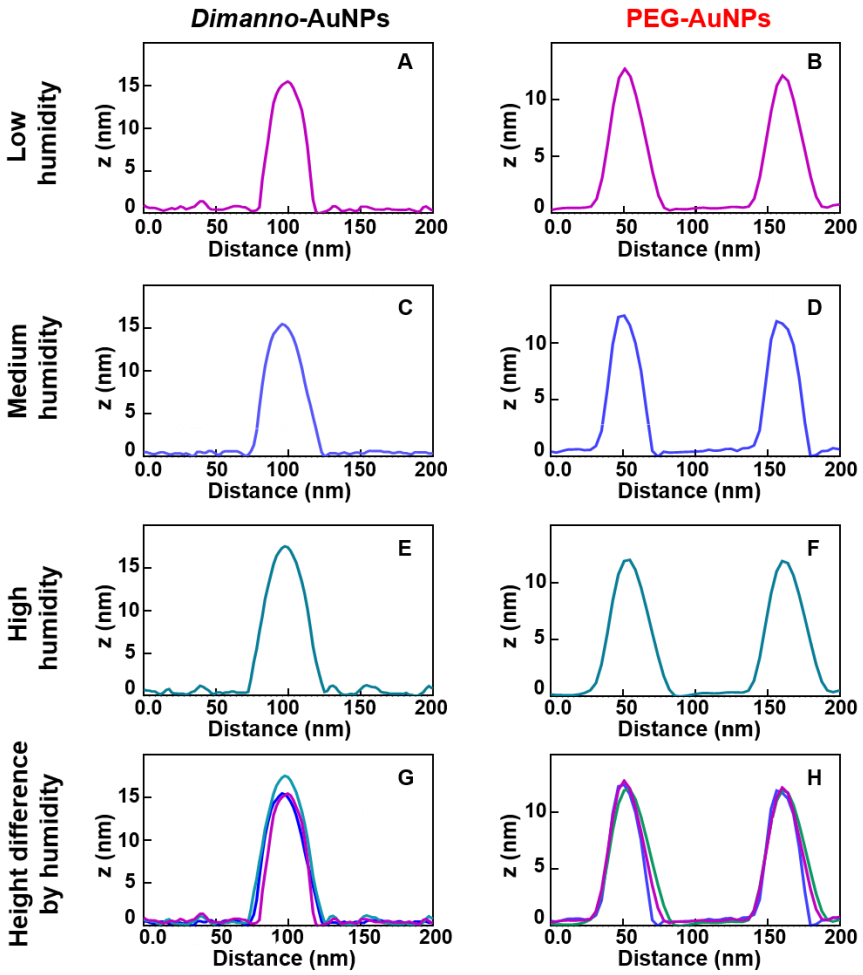

Figure 3.11. Representative AFM topography height profiles of *Dimanno*-AuNPs and PEG-AuNPs on hydrophilic conditions obtained at different humidity. (A and B) Height profiles of the samples at low humidity extracted from the horizontal lines of (A and B) in Figure 3.10, respectively. (C and D) Height profiles of the samples at medium humidity extracted from the horizontal lines of (C and D) in Figure 3.10, respectively. (E and F) Height profiles of the samples at high humidity extracted from the horizontal lines of (E and F) in Figure 3.10, respectively. (G and H) Comparison of the scanned particles at low humidity (magenta) medium humidity (blue) and high humidity (dark cyan). Note that low humidity refers to ~ 15 % RH, medium humidity refers to ~ 50 % RH and high humidity refers to ~ 90 % RH.

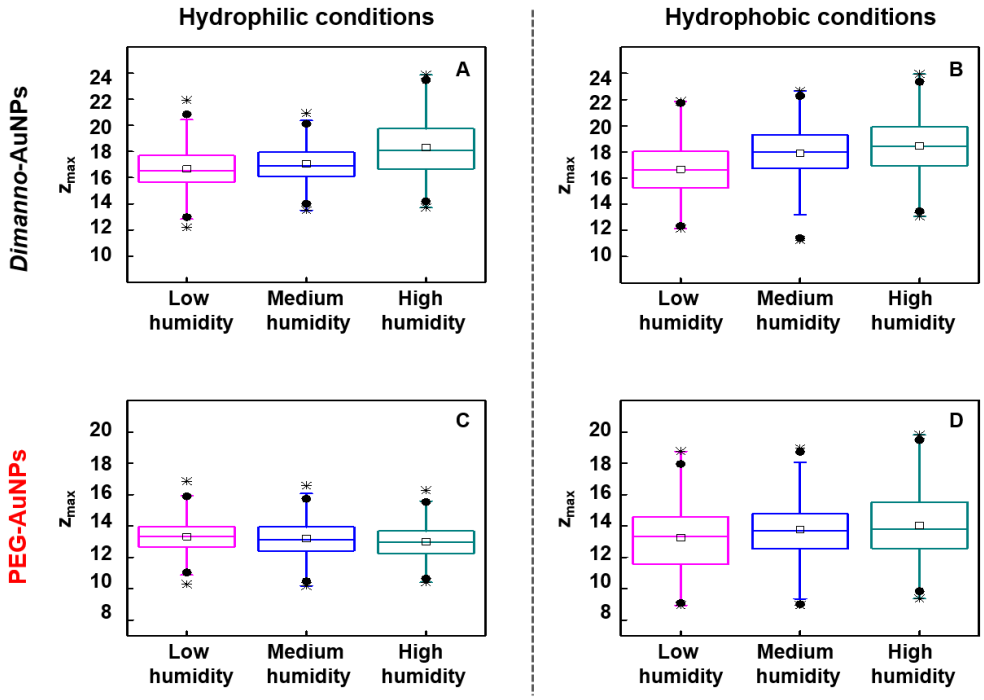

Figure 3.12. Box plots of maximum heights (z_{max}) of *Dimanno*-AuNPs and PEG-AuNPs obtained at different humidity. *Dimanno*-AuNPs on (A) hydrophilic and (B) hydrophobic conditions. PEG-AuNPs on (C) hydrophilic and (D) hydrophobic conditions. Magenta box plots refer to low humidity, blue box plots refer to medium humidity and dark cyan box plots refer to high humidity. Each box plot shows the interquartile range (from 25 % to 75 %). The extreme of the box represents the 5 % and 95 % quartile respectively. Middle line represents the median and the squares the mean value. Black circles are the 1 % and 99 % quartile and black stars are the minimum and maximum value. Note that low humidity refers to ~ 15 % RH, medium humidity refers to ~ 50 % RH and high humidity refers to ~ 90 % RH.

Experiments with D_2O were also performed on *Dimanno*-AuNPs adsorbed to gold substrates (**Figure 3.13**) in order to confirm the geometries for the VSFG experiments in **section 3.3.1**. The AFM measurements were achieved with a silicon tip and the humidity of the system was tuned by using an air stream of D_2O vapor instead of H_2O vapor.

Performing experiments with D_2O enabled to unveil if the increase in the z_{max} of single particles was merely driven by the adsorption of water layers on the dimannose residues or by any other mechanism like swelling of the particles. As in the previous cases, the particles increased in their z_{max} when increasing the RH of the system. This was influenced neither by the substrate nor by the tip used, leading to comparable data with

respect to the hydrophilic and hydrophobic conditions (**Table 3.1**) at low (16.6 ± 1.6 nm, n = 300), medium (17.2 ± 1.5 nm, n = 300) and high humidity (17.9 ± 1.9 nm, n = 300).

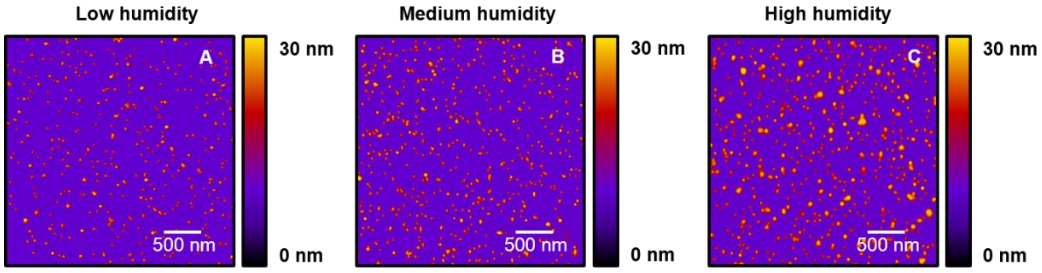

Figure 3.13. Representative AFM topography images of *Dimanno*-AuNPs on gold obtained at different humidity. (A) Particles scanned at low humidity. (B) Particles scanned at medium humidity. (C) Particles scanned at high humidity. Note that the humidity set up at medium and high humidity was achieved by using an air stream of air/D_2O. Low humidity refers to ~ 15 % RH, medium humidity refers to ~ 50 % RH and high humidity refers to ~ 90 % RH.

Particle	Substrate	RH source	z_{max} low humidity (nm)	z_{max} medium humidity (nm)	z_{max} high humidity (nm)
***Dimanno*-AuNPs**	APDMES Silicon	H_2O vapor	16.7 ± 1.6	17.0 ± 1.4	18.3 ± 2.1
	OTS Silicon	H_2O vapor	16.7 ± 2.0	17.7 ± 2.3	18.4 ± 2.2
	Gold	**D_2O** vapor	16.6 ± 1.6	17.2 ± 1.5	17.9 ± 1.9
PEG-AuNPs	APDMES Silicon	H_2O vapor	13.3 ± 1.0	13.2 ± 1.1	13.0 ± 1.0
	OTS Silicon	H_2O vapor	13.2 ± 2.1	13.7 ± 2.0	14.0 ± 2.2

Table 3.1. z_{max} of individual *Dimanno*-AuNPs and PEG-AuNPs measured by AFM at different hydration conditions. Results are expressed as the mean ± SD. Uncertainties were obtained from statistical errors. Note that low humidity refers to ~ 15 % RH, medium humidity refers to ~ 50 % RH and high humidity refers to ~ 90 % RH.

Finally, the particle distribution of z_{max} achieved at low and high humidity was compared (**Figure 3.14**). For this Mann-Whitney test, a nonparametric test, was performed independently for the *Dimanno*-AuNPs and PEG-AuNPs. The statistical analysis for the *Dimanno*-AuNPs on hydrophilic and hydrophobic conditions and experiments with D_2O have shown non-significant differences in sample distribution both at low ($p = 0.46$) and high humidity ($p = 0.06$). In contrast, the z_{max} achieved on PEG-AuNPs depended on the scanning conditions. Non-significant differences in height distribution were found at low

humidity (p = 0.51), but significant differences were found when comparing the hydrophilic and hydrophobic conditions at high humidity (p < 0.0001).

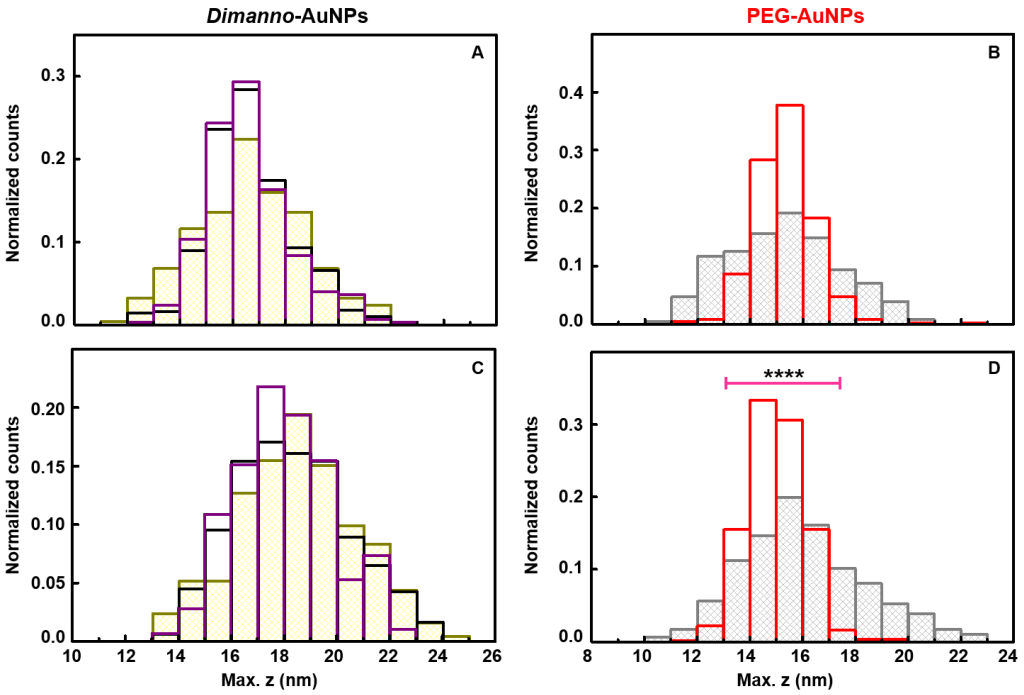

Figure 3.14. z_{max} AFM histograms of individual *Dimanno*-AuNPs and PEG-AuNPs achieved at low and high humidity. (A) *Dimanno*-AuNPs at low humidity. (B) PEG-AuNPs at low humidity. (C) *Dimanno*-AuNPs at high humidity. (D) PEG-AuNPs at high humidity. Yellow bars correspond to measurements performed on gold. Purple and grey bars correspond to measurements performed on hydrophobic conditions. Black and red bars correspond to measurements performed on hydrophilic conditions. The pink horizontal line in (D) exhibits a meaningful increase in the z_{max} of the particles scanned on hydrophobic conditions with respect to the hydrophilic conditions (****p < 0.0001). Note that the counts are normalized. Low humidity refers to ~ 15 % RH, medium humidity refers to ~ 50 % RH and high humidity refers to ~ 90 % RH.

3.4 DISCUSSION

PEG and dimannose coating layers of AuNPs were chemically and physically characterized by VSFG, FT-IR, DLS, ZP, SEM, STEM and AFM.

The chemical composition of the organic layers was confirmed by SFG and FT-IR (**Figure 3.3**, **Figure 3.4**), demonstrating that the dimannose residues are and remain coupled to the PEG chains, and that they provide ordering properties to the shell. In dehydrated conditions, both PEG and dimannose bind water at the interface. However, the higher hydrophilicity of dimannose enables a better interaction with water molecules, which are not desorbed after dehydration (i.e. low humidty). This is also supported by previous research on SAMs on gold substrates, which revealed a more hydrophilic tendency of surfaces functionalized with mannose terminal groups (Mann-C_5-S, contact angle < 5°) with respect to carboxylic-acid terminal groups (COOH-C_{11}-S, contact angle ~ 45°) [121]. Also, the steric hindrance effects on the *Dimanno*-AuNPs may act as water molecular "traps" on the sample surface. As a consequence, higher water adsorption in dry environment is detected. One should note that extremely dry conditions, as achieved in high vacuum for the SEM and STEM experiments, must remove practically all adsorbed water molecules.

The particle size obtained in suspension by DLS (**Figure 3.5**), and after dehydration by AFM (**Table 3.1**), showed major differences according to the type of sample. On the one hand, the estimated size and z_{max} of individual *Dimanno*-AuNPs was found to be identical in DLS (16.8 nm) and in AFM (16.7 nm), respectively. In principle, DLS should provide higher particle size due to hydration/solvation of the sample in solution, and should be merely considered as an indicative size of the colloid, i.e. the nanoparticle plus multiple water layers. The observed similarities in particle size both in solution and in dry conditions suggest that the dimannose ligands are very efficiently packed on the AuNPs. On the other hand, the particle size and z_{max} of PEG-AuNPs was significantly different between DLS measurements (41.1 nm) and AFM (13.3 nm). The DLS diameter is far above any reasonable hydrodynamic diameter of a single AuNP, so particle agglomeration in solution is obvious, which is confirmed by the high PDI. Indeed, previous studies have shown agglomeration of such particles to clusters. This process can be inhibited by covalently linking BSA to the PEG-AuNPs [104]. The addition of dimannose, also covalently bound, also decreases agglomeration. More generally, it is established that a concentrated carbohydrate solution (more than 40 % of the total aqueous volume) provides a macromolecular crowding environment which diminishes particle interaction [122], which can even be used during nanoparticles synthesis. For example, the *Dimanno*-AuNPs used in this research were produced in a solution of ~ 50 % of dimannose targeting ligand, which is sufficient to decrease the agglomeration tendency. The increased stability of *Dimanno*-AuNPs may be associated with the physical constraint provided by the

dimannose linkers during synthesis, as well as strong intramolecular interactions between the dimannoside residues that prevent from particle-particle interactions.

In the same line, particle adsorption differs on hydrophilic APDMES- and on hydrophobic OTS-silanized surfaces (**Figure 3.8**). At the millimeter scale, the coffee ring phenomena is observed on the OTS surface, but not on the APDMES counterpart. This is related to the competition between the time scales of the liquid evaporation and the particle movement. When the liquid evaporates much faster than the particle movement, coffee ring formation may cease [119]. In this research, the deposition protocol may have influenced the observed phenomena. On the hydrophilic substrates, particles were adsorbed from aqueous suspensions which favored particle-substrate interactions with subsequent immobilization. This should be based on multiple hydrogen bonds to the OH groups in the dimannoside. Hence, the evaporation of the droplet was much faster than the particle movement and no coffee ring effect was observed. The drop-casting method used on the hydrophobic substrates allowed a complete evaporation of the droplet. Since the particle-substrate interactions were mainly guided by hydrophobic effects, the (hydrophilic) particles were hardly attached to the surface and particle-particle interactions were favored. As a consequence, particle movement was faster than the water evaporation, resulting in the observed coffee ring phenomena.

The adsorption at the nanoscale complemented the results at the microscale. On APDMES silicon, we can assume that the particle adsorption at neutral pH was guided by electrostatic interactions between the protonated amine groups from the APDMES and the carboxylate residues, possibly also by hydrogen bonds. Hence, a similar dispersion of both *Dimanno*-AuNPs and PEG-AuNPs was expected. The observed differences can be related to the particle dispersion in solution. DLS data revealed that the PEG-AuNPs were agglomerated, but not the *Dimanno*-AuNPs. From the hypothesis that the particles became immobile after adsorption, the incubation time of PEG-AuNPs did not allow a proper dispersion of the particles on the substrate. In contrast, a single *Dimanno*-AuNP could interact more efficiently with the silanized surface, indicating that particle-substrate interactions dominated over particle-particle interactions. This is most likely based on hydrogen bonds between the (multiple) OH groups in the dimannoside and the amine.

On the hydrophobic substrates, *Dimanno*-AuNPs were more dispersed than the particle precursors. FT-IR measurements support this observation: The more hydrophilic nature of the *Dimanno*-AuNPs should have influenced the water evaporation rate. A slower evaporation or a smoother sample dehydration should favor particle-substrate interactions, resulting in a better dispersion of the sample on the substrate. This was also reported in TEM on carbon grids: PEG-AuNPs with short chain or long chain polymers exhibited particle adsorption in clusters [123], while surface-coupled α-1,4-mannobiose on AuNPs presented homogenous particle dispersion [34] [49].

In terms of hydration, the results from this investigation show stronger water adsorption of *Dimanno*-AuNPs with respect to the PEG-AuNPs (**Figure 3.10 – 3.13**), which

is also in agreement with the more hydrophilic nature of the dimannose residues. Although the data are within the uncertainties of the experiment, statistical analysis complements these findings and demonstrates that only the water adsorption on *Dimanno*-AuNPs is independent from the scanning conditions (**Table 3.1**, **Figure 3.14**).

Taking into account the size of a water molecule (~ 0.28 nm) and the typical thickness of a hydration layer (~ 0.6 nm) [13] [124], the absolute values obtained in this report indicate ~ three to four layers of water adsorption (~ 1.5 nm), possibly on the dimannose coating. From STEM measurements in completely dried samples the organic layer on *Dimanno*-AuNPs was ~ 1.5 nm, too (**Figure 3.7).** This suggests that the thickness increase of the organic layer due to water adsorption is about 100 %. The water can be present in a layer, but also in between the various dimannoside groups, which would correspond to a "swelling" of the AuNP organic coating.

PEG-AuNPs have shown increase in the z_{max} corresponding to one water layer on the hydrophobic conditions (~ 0.8 nm). This was not observed on the hydrophilic counterpart. Although the reason remains unclear, one may think in excluded volume interactions, which may cause depletion forces under hydrophilic conditions. In addition, research on hydrophobic samples demonstrated poor reproducibility of the data due to scanning artifacts such as irreversible modification of either the tip or the sample surface, or both [92].

In this regard, wet-STEM and SEM investigations on PEG-AuNPs differ from our data, indicating that particle hydration occurs and is independent of the selected substrate [120] [125]. Yet, these studies were performed on particle clusters in crowded environments. Hence, the reported conclusions may be associated with collective phenomena that are not in our scope but might be relevant for future investigations.

GNPs have been widely investigated for biomedical applications, like biochemical sensing, imaging or drug delivery systems [126]. The success of this platform stems from its good dispersion in water, and from its stability and biocompatibility in fully hydrated states, likewise in biological fluids. Our investigation shows a novel approach to these particles by testing the hydration properties of *Dimanno*-AuNPs in air at various humidity conditions. On the one hand, revealing the water adsorption of mannosides from dehydrated state to high humidity may offer new insights into the molecular role of these surface residues from a biophysical understanding. In particular, the size, surface composition and controlled orientation of the *Dimanno*-AuNPs results in suitable candidates for emulating viral surface glycoproteins – such as Influenza HA – under hydration/dehydration cycles. Indeed, several viral pathogens display a preponderance of mannose residues on their surface [127], particularly in surface glycoproteins. These are responsible for infection and probably provide adaptability to dryness, e.g. in aerosols. On the other hand, the higher water adsorption of *Dimanno*-AuNPs with respect to the very well-studied PEG-AuNPs leads to considering them as potential candidates for gas sensing applications. Sensors are usually kept dry, and then become hydrated in moist air.

Although studies on PEG-AuNPs clusters at the nanoscale have already been reported [120] [125], limited data is available for AuNPs coated with carbohydrates.

3.5 CONCLUSIONS

The diverse properties of *Dimanno*-AuNPs under different conditions were demonstrated. The dimannose coating decreases particle aggregation in solution and favours the dispersion of the particles when adsorbed on flat surfaces. The main finding here is the water adsorption of single *Dimanno*-AuNPs in the humid air. Hydration cycles from dehydration to high humidity in AFM show an increment in particle z_{max} in agreement with the adsorption of a few water layers, which possibly takes place in the organic shell.

From this data, we present *Dimanno*-AuNPs as potential candidates to emulate viral surface glycoproteins in air. The influence of humidity on the surface mannosides can be easily evaluated in a controlled and straightforward approach.

Chapter 4

Investigating the protective effects of Influenza A virus hemagglutinin against dehydration

This chapter focuses on understanding the effect of relative humidity on Influenza A H1N1 virus. Its envelope is based on lipid bilayers, containing the surface glycoprotein hemagglutinin in very high density. A model based on a supported lipid bilayer, with integrated hemagglutinins, was constructed. For complete cycles of hydration, dehydration and rehydration, the membrane performance was evaluated in terms of structure and dynamics, which were assessed by combining Confocal Fluorescence Microscopy, Raster Image Correlation Spectroscopy, Line-Scan Fluorescence Correlation Spectroscopy and Atomic Force Microscopy. The results indicate that the presence of hemagglutinin prevents macroscopic membrane damage after dehydration. Without hemagglutinin, fast membrane disruption is followed by irreversible loss of lipid and protein mobility. Although the developed model is principally limited by the membrane composition, the macroscopic effects of hemagglutinin under dehydration stress reveal new information on the stability of virus particles at low relative humidity.

4.1 INTRODUCTION

Seasonal influenza is an acute respiratory infection caused by Influenza viruses (e.g. Influenza A virus, IAV) circulating throughout the world and causing epidemics of the disease. Every year, up to 5 million cases of severe flu illness and 650000 flu-related deaths are reported [25]. Influenza activity follows largely predictable seasonal patterns, which are related to environmental conditions, such as temperature, ultraviolet light and humidity [36] [37] [4]. Indeed, in temperate climates, the seasonal outbreaks occur mainly in winter, when humidity and temperature are low, while in tropical regions the patterns may be less pronounced. Among these conditions, the link between humidity and virus transmission or survival has been subject of debate. Studies in animal models, e.g. ferrets [128] and guinea pigs [129], have demonstrated that cold temperatures and – independently – also low relative humidity (RH) favor airborne virus transmission. Epidemiological evidence suggests that humidity affects virus transmission by modulating virus survival [4], while other studies have also associated the virus survival, transmission and seasonality with either absolute humidity [45] or RH [48]. Biophysical investigations have demonstrated that, at low humidity, the dehydration of respiratory droplets may affect the virus structure [5]. In stark contrast, recent research revealed the sustained infectivity and stability of IAV contained in human bronchial epithelial aerosols over a wide range of RH [42].

Efforts to resolve the virus structure at the molecular level have been based on the use of high-resolution techniques such as Cryo-Electron Microscopy [130], Cryo-Electron Tomography [26] or super-resolution Fluorescence Microscopy [131]. These studies have been mostly focused on revealing the spatial organization of the genome and proteins from the enveloped virus particle. Studies are usually carried out in ice (frozen buffer) and occasionally in solution. Still, the detailed interactions between water and the molecular components of enveloped virus particles (specifically for the case of low water amounts) have been neglected and are still beyond our understanding.

Here, unprecedented observations of the structural and dynamical changes taking place in models of the IAV H1N1 envelope are reported after a complete cycle of hydration, dehydration and rehydration. For this, a combination of Fluorescence Microscopy imaging, Raster Image Correlation Spectroscopy (RICS), Line-Scan Fluorescence Correlation Spectroscopy (LSFCS) and Atomic Force Microscopy (AFM) was developed.

Solid supported lipid bilayers (SLBs) have been extensively used as model membranes in biophysics due to their high stability and versatility in natural environments. These phospholipid bilayers are supported by solid substrates and can be functionalized with proteins in a well-defined orientation, thus allowing to study the lateral diffusion of membrane components under non-denaturing conditions [132] [133]. In this work, models of the IAV H1N1 virus envelope consisting of SLBs functionalized with hemagglutinin (HA) were studied by combining Fluorescence Microscopy and AFM.

Fluorescence Microscopy and AFM have been widely employed in virus research to perform molecular studies under physiological conditions [134] [135] [136]. The combination of these complementary techniques allows to understand complex membrane systems and characterize protein-protein, lipid-lipid and protein-lipid interactions [137]. In the context of Fluorescence Microscopy, advanced quantitative approaches such as RICS and LSFCS (**section 2.8.1**) provide information on the dynamics of molecules by measuring e.g. local concentrations and diffusion coefficients of proteins and lipids, protein partitioning, or association and dissociation constants [81] [138]. LSFCS in particular minimizes photobleaching effects and provides more reliable results in dehydrated lipid samples, for which molecular diffusion is very slow [80]. The 2-dimensional approach of RICS offers exploration of the dynamics of molecules over a wide temporal and spatial scale, from microseconds between adjacent pixels in the x-direction, milliseconds between adjacent pixels in the y-direction, and seconds between successive images [82]. Finally, AFM provides structural information in native environments, from solution to variable humidity in air, or even vacuum. A detailed topography of the surface can be obtained from a 3-dimensional scan of the surface with nanometric spatial resolution. This includes also adsorbed water layers, so that height variations can be correlated with air humidity. AFM studies on Influenza viruses are not new [139], but have been usually achieved only in liquid environment (solution) [140] [141] [142] or in the desiccated state [143].

By combining all the above-mentioned techniques, SLBs containing the IAV H1N1 surface glycoprotein HA were investigated and compared against protein-free bilayers or bilayers containing a non-viral model protein (i.e. green fluorescent protein, GFP). Detailed information on membrane dynamics and surface morphology at the macro and microscale – in solution and in air – under hydration, dehydration, partial rehydration and full rehydration conditions was obtained.

4.2 MATERIALS AND METHODS

4.2.1 *Materials*

1,2-Dioleoyl-*sn*-glycero-3-phosphocholine (DOPC), 1,2-dioleoyl-sn-glycero-3-[(N-(5-amino-1-carboxypentyl)iminodiacetic acid)succinyl] (nickel salt) (DGS-NTA-Ni), 1-palmitoyl-2-(dipyrromethene boron difluoride)undecanoyl-sn-glycero-3-phosphocholine (TF-PC) and 1,2-dioleoyl-sn-glycero-3-phosphoethanolamine-N-(lissamine rhodamine B sulfonyl) (ammonium salt) (Rho-PE) were purchased from Avanti Polar Lipids (Alabaster, USA) and used without further purification. IAV recombinant HA [A/Puerto Rico/8/1934 (H1N1)] was purchased from The Native Antigen Company (Kidlington, United Kingdom). The protein was produced in mammalian HEK293 cells (≥ 95 % purity determined by SDS-PAGE from the manufacturer), providing the required post-translational modifications (i.e. glycosylation). The ectodomain protein fragment (Asp18-

Gn529) was fused with 8 × Gly-Ser linker and a 6 × His-tag at the C-terminally located transmembrane domain. *Aequorea victoria* GFP was bought from Invitrogen (Carlsbad, USA). The recombinant protein was expressed in *Escherichia coli* (≥ 85 % purity determined by SDS-PAGE from the manufacturer) and was fused with 6 × His-tag at the N-terminus. AlexaFluor® 568 succinimidyl ester (A568), Rhodamine Red (Rho) and the protein ladder PageRuler™ were acquired from Thermo Fischer Scientific (Karlsruhe, Germany). Atto 488 amine fluorescent label, Dulbecco's phosphate buffered saline (DPBS) without Mg^{+2} and Ca^{+2} was purchased from PAN-Biotech (Aidenbach, Germany). Absolute ethanol, acetone and silica gel microspheres were purchased from Sigma-Aldrich (Steinheim, Germany). Deionized, filtered water (referred as "Milli-Q", specific resistance 18.2 $M\Omega cm^{-1}$, TOC (total organic content) < 10 ppb) was obtained by an Advantage System from Millipore (Burlington, USA). The hydrophobic ink was obtained from Electron Microscopy Sciences (Hatfield, USA). Glass dishes (D35-20-0-TOP) were bought from Cellvis (Sunnyvale, USA), electrophoresis gel (Biorad Mini-Protean® Tetra Cell) was obtained from Bio-Rad Laboratories, Inc (Hercules, USA). The glue NOA63 was purchased from Norland (Cranbury, USA).

4.2.2 *SDS-PAGE*

SDS-PAGE was performed for estimating the molecular weight (MW) of IAV HA. Conventional 12 % gel of acrylamide / bis acrylamide was performed using a Biorad Mini-Protean® Tetra Cell with 0.75 mm space plates. Two samples of 335 ng/µL and 167.5 ng/µL were loaded. A protein ladder from 10 to 250 kDa was used and the gel was run at 120 V for 80 minutes.

4.2.3 *Fluorescence labeling*

IAV HA was conjugated with the A568. The protein was incubated overnight at 4 °C in a 1:1:0.1 molar ratio of protein, reactive dye and sodium bicarbonate buffer (1 M $NaHCO_3$, pH 8.3 - 9.0). Free dye was removed by dialysis using a 12000 MWCO mini-dialyzer (Carl Roth GmbH & Co., Karlsruhe, Germany) against DPBS buffer, pH 7.4, overnight at 4 °C. Protein concentration and labeling efficiency were determined by absorbance at 280 nm and 578 nm, respectively. The HA concentration was estimated by using the molar extinction coefficient of the protein monomer (~ 86000 $M^{-1}cm^{-1}$). Protein concentrations were generally between 4.5 and 7.5 µM, while labeling efficiencies were of 1 dye molecule per 4 - 10 monomers.

4.2.4 *Preparation of SLBs*

SLBs were prepared according to the vesicle fusion method [144]. For the formation of multilamellar vesicles (MLVs), 90 mol % DOPC and 10 mol % DGS-NTA-Ni were mixed in absolute ethanol and labeled either with TF-PC or Rho-PE. 0.25 mol % of fluorescent lipid was used for imaging and 0.01 mol % for quantitative fluorescence measurements. After solvent evaporation, the lipid film was rehydrated with DPBS buffer (pH 7.4) to a final concentration of 4.1 mg/mL lipid. The MLV suspension was sonicated for 10 minutes at 40 °C to form small unilamellar vesicles (SUVs) and diluted 10-fold with the same buffer. 100 µL of suspension were deposited on a glass dish (AFM surface root mean square (RMS) roughness (0.26 ± 0.02) nm on 5 x 3 μm^2 images) previously cleaned with absolute ethanol and Milli-Q water. To achieve AFM in solution, the liquid droplet was confined with a hydrophobic pen. For Fluorescence Microscopy and AFM in air, sample confinement was carried out by attaching a plastic cylinder of 7 mm diameter to the glass with a thin layer of NOA63 glue. Vesicle fusion and bilayer formation were induced by addition of 5 mM of calcium chloride ($CaCl_2$), and unfused SUVs were removed by extensive rinsing with DPBS buffer (pH 7.4).

4.2.5 *Protein binding to the SLBs*

Labeled HA was added to the previously prepared SLBs to a final concentration of 2 µM. The proteins were incubated for 50 minutes to achieve high packing density on the SLBs, via Nickel (Ni^{2+})/hexahistidine-Tag (Ni/His-tag) interaction [145]. Incubation time and protein concentration were selected by optimizing protein binding on the SLBs. His-tagged carbon monoxide dehydrogenase (0.25 µM) was used as test protein and incubated for varying amounts of time with a single SLB. After incubation, excess protein was removed by washing with DPBS buffer and the fluorescence signal of the labeled protein was detected. The incubation time was finally selected based on the time needed for the signal to reach a near-equilibrium level. Next, a binding curve using different HA concentrations, ranging from 0 to 1.75 µM was obtained. The maximum (saturation) concentration to be reached already at 1.75 µM was estimated, and 2 µM was selected as working concentration. For the experiments described in this work, the optimized binding parameters were then used to prepare SLBs functionalized with HA ("HA-bilayers") or His-tag GFP ("GFP-bilayers").

4.2.6 *Sample dehydration and rehydration*

After the preparation of samples as described in **4.2.4** and **4.2.5** (referred to as "hydrated samples"), buffer salts were removed by rinsing with Milli-Q water multiple times to avoid membrane defects due to the formation of salt crystals. For sample dehydration, ~ 60 % of the total water volume was removed by pipetting. The remaining

water was removed for 48 h in a chamber with silica gel microspheres at (20 ± 3) % RH. These samples are referred to as "dehydrated samples". Partial rehydration of SLBs was achieved by incubating the samples in a sealed chamber with (95 ± 3) % RH for 24 h. The RH of the chambers was continuously monitored with a mini data logger (174 H Testo, Lenzkirch, Germany). These samples are referred to as "partially rehydrated samples". To achieve full rehydration of the membranes ("fully rehydrated samples"), 150 μL DPBS buffer (pH 7.4) was added directly to partially rehydrated SLBs.

4.2.7 *Fluorescence Microscopy*

Confocal Fluorescence Microscopy imaging, RICS and LSFCS were performed on a LSM 780 Zeiss confocal microscope (Carl Zeiss, Oberkochen, Germany) using a 40 × Plan-Apocromat 1.2 numerical aperture (NA) Korr DIC M27 water immersion objective. Single species measurements were performed using a 488 nm Argon laser (for TF-PC or GFP). Excitation and emission light were split with a 488 nm dichroic mirror. Two-species measurements were performed with an additional excitation line at 561 nm, provided by a laser diode (for the fluorophores Rho-PE, A568). In this case, a 488/561 nm dichroic mirror was used to separate excitation and emission. The fluorophores were excited and detected sequentially for different regions of the spectrum. Fluorescence was detected between 499 and 552 nm (TF-PC or GFP) and between 570 and 695 nm (Rho-PE or A568) in photon counting mode with 32-channel GaAsP detector array. The microscope was calibrated before each experiment with Atto 488 (488 nm) and with Rho (561 nm) fluorescent dyes in solution. Typical counts per molecule were ~ 3.6 kHz for Atto 488 and 4.2 kHz for Rho. The absolute units (A.U.) were comparable between experiments and daily variations were consistently within 10 % of these values.

Images of 512 x 512 pixels were acquired for hydrated samples using the 488 nm laser with ~ 4 to 8 μW (between 10 and 100 μW for 561 nm). For measurements in dehydrated or partially rehydrated samples, SLBs were sealed with a glass dish top and tape immediately after being removed from the incubation chamber. Images were obtained in at least three independent bilayer replicates (~ 3 - 6 images for each hydration condition per replicate). Manual scratching tests were performed on HA-bilayers after dehydration using a sharp metal tweezer, as reported elsewhere [146]. Laser power for measurements in dehydrated or partially rehydrated SLBs varied accordingly to the type of sample, from 4 to 20 μW at 488 nm and from 10 to 100 μW at 561 nm. After full rehydration, 2 μL of 1 mM TF-PC or Rho-PE solution were added directly on the protein-free bilayers and GFP-bilayers to improve imaging quality. This was not necessary for HA-bilayers as the fluorescence intensity remained high throughout the dehydration and rehydration cycle.

All images were acquired with 3.15 μs and 12.61 μs pixel dwell time and processed with ZEN software version 3.0 (Carl Zeiss, Oberkochen, Germany). The surface coverage of the dehydrated protein-free bilayers (number of images, n = 22), and the GFP-bilayers

(n = 16) was obtained with ImageJ [101]. For this, individual images were converted into 8-bit images and adjusted by automatic global threshold (manually carefully corrected). The surface coverage of the binary images (expressed as % area) was automatically measured by the software.

RICS measurements were performed in the framework of arbitrary-region RICS [147] [148] as previously described [81] [149]. Single frames of 256 x 256 pixels and 40 nm pixel size were acquired. Between 9 and 12 measurements were collected per sample per hydration condition in at least three replicates. Data in hydrated samples was acquired at 50.42 μs pixel dwell time and 7.75 s frame time. Measurements in dry or partially rehydrated samples were acquired at the lowest dwell time possible (177.32 μs pixel dwell time and 27.24 s frame time) and the laser power was adjusted to maximize the signal and minimize photobleaching for all species at each condition [82]. For 488 nm excitation, 5 μW (TF-PC) or 0.5 - 1 μW (GFP) excitation power were used in hydrated samples. 5 - 8 μW (TF-PC, GFP) were used for dehydrated and partially rehydrated samples. 5 - 8 μW (TF-PC) or 1 μW (GFP) were used for fully rehydrated samples. The A568 fluorophore used for protein labeling was always excited with ~ 1 μW laser power, while Rho-PE excitation was optimized based on the specific sample (5 - 10 μW excitation power for hydrated samples, 2 μW for dehydrated and partially rehydrated samples, and 2 - 20 μW for fully rehydrated samples). RICS data of images containing photon counts as a function of pixel position were analysed using a custom-written MATLAB code (The MathWorks, Natick, USA) developed by the Chiantia group at University of Potsdam[1]. Diffusion results were plotted with GraphPad Prism version 8.0.1 for Windows (GraphPad Software, San Diego, USA) and the diffusion coefficients were expressed as the mean ± standard deviation (SD).

LSFCS measurements were performed as described in [150]. Briefly, a line scan of 256 x 1 pixels (pixel size 40 nm) was achieved with 0.79 μs pixel scan time and 300000 lines were acquired for each measurement (141.82 s total time). The laser excitation power for 488 nm was 8 μW and the A568 dye used for protein labeling was excited with ~ 5 μW for all the tested conditions. Two samples were examined and at least 3 measurements were taken for each hydration condition per sample. The LSFCS data (one channel per file) were exported as TIFF files, imported and analysed in MATLAB like in [150].

4.2.8 *AFM measurements*

Topography images were obtained on an Agilent 5500 microscope (Keysight, Santa Clara, USA) at 24 °C with speed rates between 0.8 and 1.2 lines per second. At least 6

[1] The code is publicly available on https://www.uni-potsdam.de/de/ibb-physbiochem/downloads-144413-folder

different images of 20 x 20 μm^2 were scanned per hydration condition. In some cases, (i.e. images in hydrated samples) 50 x 50 μm^2 images were obtained in 3 different positions. Each image was subsequently studied in detail by scanning on smaller areas. The measurements were performed in three replicate samples.

The images were examined by using picoView 1.14 software (Keysight, Santa Clara, USA). Images of 256 x 256 pixels were acquired in hydrated samples in contact mode in DPBS buffer (pH 7.4). A DNPS silicon nitride probe < 10 nm nominal radius, 0.12 N/m force constant and a resonant frequency of 34 kHz (Bruker, Madison, USA) was used for scanning. Prior to each measurement, the probe was cleaned with acetone and absolute ethanol. The liquid droplet over the SLBs had a diameter of ~ 20 mm and was confined using a hydrophobic ink. During the scanning, the sample was always covered with DPBS buffer and the set point was continuously adjusted to minimize the applied force.

The hydrated samples were prepared following the protocol described in **section 4.2.4** and **section 4.2.5** and afterwards they were dehydrated as described in **section 4.2.6**. For these samples, the solution was initially confined with a plastic cylinder (**section 4.2.4**) which was eventually carefully removed with tweezers. An environmental isolation chamber (Keysight, Santa Clara, USA) was mounted to the AFM, thus providing a completely sealed and isolated environment. A gentle and continuous stream of nitrogen was blown into this chamber till reaching (20 ± 3) % of RH. Scratch and scan tests were performed on HA-bilayers after dehydration. For this, a small area of the sample was completely removed with the AFM tip by scanning the sample in contact mode at high setpoint (0.75 - 1 V) for three times. Afterwards, the tip was retracted from the surface and a larger area was scanned in intermittent contact mode (tapping mode). For partially rehydrated samples, a RH at (95 ± 3) % was achieved by controlling the mixing ratio between a dry and a wet (water-saturated) stream of nitrogen. The sample was allowed to equilibrate overnight in the saturated chamber. The fully rehydrated samples were finally achieved by adding DPBS buffer to the partially rehydrated samples. Images of 512 x 512 pixels were obtained in tapping mode for dehydrated, partially rehydrated and fully rehydrated samples. A Multi-75 probe (Budget sensors, Sofia, Bulgaria) with a nominal radius of < 10 nm, force constant of 3 N/m and resonance frequency of 75 kHz was used for imaging HA-bilayers and protein-free bilayers. Images on GFP-bilayers were acquired with a high-resolution cantilever C14 Cr/Au, nominal radius of ~ 1 nm, force constant of 5 N/m and resonance frequency of 160 kHz (MikroMasch, Sofia, Bulgaria).

AFM images were analyzed after scanning with Gwyddion software version 2.47 (Gwyddion, Brno, Czech Republic). All the topography images were first levelled by mean plane subtraction, aligned by height median and occasionally the z-excursions outliers were manually removed by e.g. correction of the scan line artefacts in the x-axis or misaligned segments within a single row. Surface roughness, maximum heights of the proteins (z_{max}) in hydrated samples and surface coverage after dehydration were calculated with WSxM 5.0 software version 8.4 [40]. For the surface roughness, the images were

automatically analysed by the software and expressed as RMS roughness. For estimating the z_{max} of the proteins, each individual image of HA-bilayers (number of images, n = 8) and GFP-bilayers (n = 5) was processed by a flooding analysis. Minimum threshold values of 8 nm for HA and 3 nm for GFP were selected. The resulting images displayed each individual protein as a "hill". By manual selection of these objects, the z_{max} of the proteins was calculated by the software. A minimum of 10 proteins were counted per image, resulting in 104 HA proteins and 98 GFP proteins. The analysis of the surface coverage of the protein-free bilayers (n = 13), HA-bilayers (n = 19) and GFP-bilayers (n = 16) after dehydration was also performed with a flooding analysis. Here, due to the heterogeneity of the samples, the minimum threshold values was manually selected and the surface coverage (expressed as the % hills area) was provided by the software. The height distribution histograms and height profiles were plotted with GraphPad Prism version 8.0.1 for Windows and the quantitative data was displayed as the mean ± SD.

4.2.9 *Statistical analysis*

Statistical analysis was performed using GraphPad Prism version 8.0.1 for Windows. Data sets were analysed by unpaired t-test (Mann-Whitney test) for comparing the same sample under different hydration conditions (e.g. partially rehydrated and fully rehydrated bilayers). In all the cases two tailed P-values were reported with a confidence level of 0.01 – 0.05.

4.3 RESULTS

4.3.1 *Fluorescence Microscopy and Raster Image Correlation Spectroscopy (RICS) measurements on SLBs after dehydration-rehydration cycles*

Membrane stability and dynamics in a IAV model system at different hydration conditions were investigated. Fluorescence Microscopy imaging, RICS and LSFCS measurements were performed in four conditions, namely 1) hydrated: in DPBS buffer immediately after preparation; 2) dehydrated: after removal of bulk water and desiccation at ~ 20 % RH; 3) partially rehydrated: achieved at ~ 95 % RH and 4) fully rehydrated: performed in DPBS buffer after 3).

IAV envelope models consisted here of SLBs containing proteins at saturation surface density (**Figure 4.1 A**), to mimic the glycoprotein density found in actual IAV envelopes (~ 8000 HA trimers/μm^2 [26]). Membranes composed of DOPC 90 mol % with 10 mol % DGS-NTA-Ni (a nickel chelating lipid) were prepared with trace amounts of either TF-PC (neutral dye) or Rho-PE (positively charged dye) as fluorescent marker. As a model of IAV glycoproteins, the HA ectodomain (Asp18-Gn529) of the strain H1N1 (A/Puerto Rico/8/1934) fused to a Gly-Ser linker and a His-tag at the C-terminus was chosen. The

latter was used to couple to proteins to the SLBs, via interaction with DGS-NTA-Ni lipids [151]. The MW of the protein estimated by SDS-PAGE was 70 - 80 kDa (**Figure 4.1 B**), in agreement with the manufacturer's data (**section 2.4**).

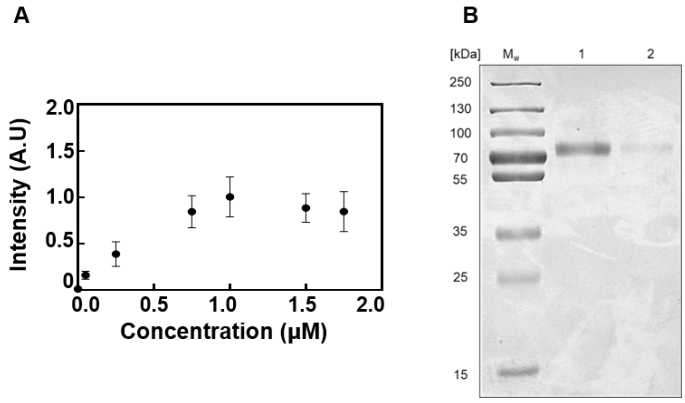

Figure 4.1. Hemagglutinin (HA) characterization and working parameters. (A) Binding curve of His-tagged HA recorded by Fluorescence Microscopy. (B) SDS-PAGE of HA Influenza A virus (IAV) H1N1 (A/Puerto Rico/8/1934/(H1N1)). Note that in (A) individual points represent the mean intensity at each condition and the vertical line the standard deviation (SD) and in (B) (MW) refers to the molecular weight of the protein ladder. (1) Corresponds to HA 335 ng/μL. (2) Corresponds to HA 167.5 ng/μL.

Fluorescence imaging of the SLBs was performed and the final protein concentration was calculated by RICS. HA-bilayers were compared to GFP-bilayers, to assess whether membrane stability was affected by the protein's identity or simply driven by e.g. protein crowding. Protein-free bilayers were used as negative control.

Initially, Fluorescence Microscopy imaging was performed (**Figure 4.2**, **Figure 4.3**) and the diffusion of fluorescent lipids was measured to investigate the overall bilayer integrity and the mobility of the SLB components. Protein-free bilayers either with TF-PC or Rho-PE dyes were examined and consecutively the labeled HA or GFP was added, respectively. **Figure 4.3** shows representative Fluorescence Microscopy images of SLBs labeled with either TF-PC (for protein-free or HA-bilayers, **A** and **B**) or Rho-PE (for GFP-bilayers, **C**). **Figure 4.4** shows the diffusion of fluorescent lipids quantified by RICS for the four tested levels of membrane hydration. As represented in **Figure 4.3 A**, homogenous and highly reproducible protein-free bilayers were obtained after preparation in the hydrated state. These were not influenced by e.g. phase separation or limited fluidity as indeed found in more complex IAV mimicking-bilayers (e.g. with cholesterol, phosphatidylethanolamine (PE), phosphatidylserine (PS) and sphingomyelin (SM), **Figure 4.2**)). After addition of HA (**Figure 4.3 B**) or GFP (**Figure 4.3 C**), the samples did not show macroscopic alterations, defects or aggregates.

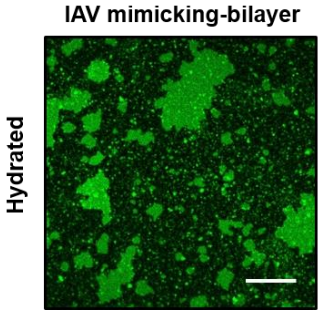

Figure 4.2. Fluorescence image of IAV mimicking-supported lipid bilayers (SLBs) in hydrated state. Representative images of hydrated SLBs in Dulbecco's phosphate buffered saline (DPBS) buffer immediately after preparation. The SLBs consist of 4.1 mg/mL lipid with 45 mol % cholesterol, 20 mol % sphingomyelin (SM), 12.5 mol % phosphatidylethanolamine (PE), 12.5 mol % phosphatidylserine (PS) and 10 mol % and 1,2-dioleoyl-sn-glycero-3-[(N-(5-amino-1-carboxypentyl)iminodiacetic acid)succinyl] (nickel salt) (DGS-NTA-Ni) and labeled with 1-palmitoyl-2-(dipyrrometheneboron difluoride)undecanoyl-sn-glycero-3-phosphocholine (TF-PC) 0.25 mol %. Scale bar corresponds to 20 μm.

The diffusion coefficients (D) of lipids (exemplified by the D of the fluorescent lipid TF-PC) in protein-free bilayers was (0.7 ± 0.3) $\mu m^2/s$ (**Figure 4.4 A** "hydrated"). Once HA was added, the fluidity of the bilayer was reduced by > 60 % ((0.24 ± 0.10) $\mu m^2/s$, **Figure 4.4 B** "hydrated"). Rho-PE in protein-free bilayers shows a similar value, albeit slightly higher ((1.06 ± 0.17) $\mu m^2/s$, **Figure 4.4 A** "hydrated"), compared to TF-PC. After binding of His-tag GFP to the SLBs, lipid mobility decreased by ~ 15 % ((0.9 ± 0.4) $\mu m^2/s$, **Figure 4.4 C** "hydrated").

Upon dehydration, the appearance of protein-free bilayers changed markedly with respect to the hydrated state. The samples showed extensive areas with structural damage indicated by the presence of bare (i.e. devoid of lipids, dark) substrate regions (**Figure 4.3 D*).*** The membrane surface coverage decreased to (26 ± 17) %. On the other hand, HA-bilayers did not show any macroscopic defect and the fluorescence signal remained spatially homogeneous (**Figure 4.3 E**). This finding was further confirmed by a "manual scratching test", for which a sharp steel tweezer was employed to remove the lipids, by applying a constant force within a selected region. The uncovering and the identification of the glass support serves to provide a defined (height or fluorescence signal) reference for further analysis. As presented in **Figure 4.5** (**A** and **B**), within the scratched region only background intensity ((0.13 ± 0.04) A.U.) was observed. Outside this region, the signal intensity was high ((2.41 ± 0.19) A.U.) and comparable to what was previously observed (**Figure 4.3 B** and **E**). The presence of a bilayer in dehydrated samples was further confirmed by AFM imaging (**Figure 4.5 C** and **D**, **section 4.3.4**), showing a dip of (3.8 ± 0.4) nm in the scratched region. Similarly to protein-free bilayers, GFP-bilayers presented

macroscopic membrane disruption and exposure of the glass surface after drying (**Figure 4.3 F**). The surface coverage was reduced to (49 ± 26) %. Both protein-free bilayers and the GFP-bilayers exhibited high sample to sample variability (17 % SD and 26 % SD, respectively).

RICS measurements were performed on random positions of the HA-bilayers. For GFP-bilayers and protein-free bilayers, measurements were performed specifically on non-damaged regions. Irrespective of membrane structure, the lipid mobility was greatly reduced after dehydration. In comparison to hydrated samples, lipids in protein-free bilayers displayed a D reduction of ~ 96 % ((0.030 ± 0.008) $\mu m^2/s$, **Figure 4.4 A** "dehydrated"). Similarly, strongly reduced lipid dynamics were observed for HA-bilayers ((0.015 ± 0.006) $\mu m^2/s$, **Figure 4.4 B** "dehydrated") and GFP-bilayers ((0.011 ± 0.005) $\mu m^2/s$, **Figure 4.4 C** "dehydrated"). Of interest, GFP-bilayers revealed the highest reduction in lipid mobility with respect to the dehydrated protein-free bilayers. This was to be expected as after dehydration, the Rho-PE GFP-bilayers were compared against the dehydrated protein-free bilayers labeled with TF-PC. These could be ascribed to the differences in the net charge of the fluorescent dyes. Still, the variations on the hydrated state were within the same order of magnitude on the differently marked bilayers, providing a good indication of using such comparable data.

After partial rehydration, significant large-scale structural changes on the membranes were not detected by Fluorescence Microscopy. Therefore, RICS measurements were performed as described for the case of dehydrated samples. D within lipid patches in protein-free bilayers increased ~ 30 % ((0.20 ± 0.07) $\mu m^2/s$, **Figure 4.4 A** "partially rehydrated"). In contrast, lipid mobility on SLBs with HA or GFP remained low but exhibited a large data spread: (0.007 ± 0.005) $\mu m^2/s$ (**Figure 4.4 B** "partially rehydrated") and (0.03 ± 0.04) $\mu m^2/s$ (**Figure 4.4 C** "partially rehydrated") respectively.

Stronger differences were found after full rehydration in DPBS buffer (**Figure 4.3 G-I**). Microscopy images indicated an apparent increase in surface coverage for both protein free-bilayers and the GFP-bilayers (**Figure 4.3 G** and **I**, respectively). These layers were very inhomogeneous and bright structures could be found, possibly related to aggregates and lipids in non-bilayer phases. RICS measurements in specific points, where the bilayer was not damaged, indicated a D recovery of ~ 99 % on the protein-free bilayers ((0.7 ± 0.3) $\mu m^2/s$, **Figure 4.4 A** "fully rehydrated") and of ~ 50 % on the GFP samples ((0.44 ± 0.21) $\mu m^2/s$, **Figure 4.4 C** "fully rehydrated"). On the other hand, HA-bilayers appeared macroscopically homogenous, except for the presence of few aggregates (**Figure 4.3 H**). In these samples, the D was of ((0.007 ± 0.007) $\mu m^2/s$, **Figure 4.4 B** "fully rehydrated"). Similar to the case of partially rehydrated samples, measurements exhibited in general a large variability.

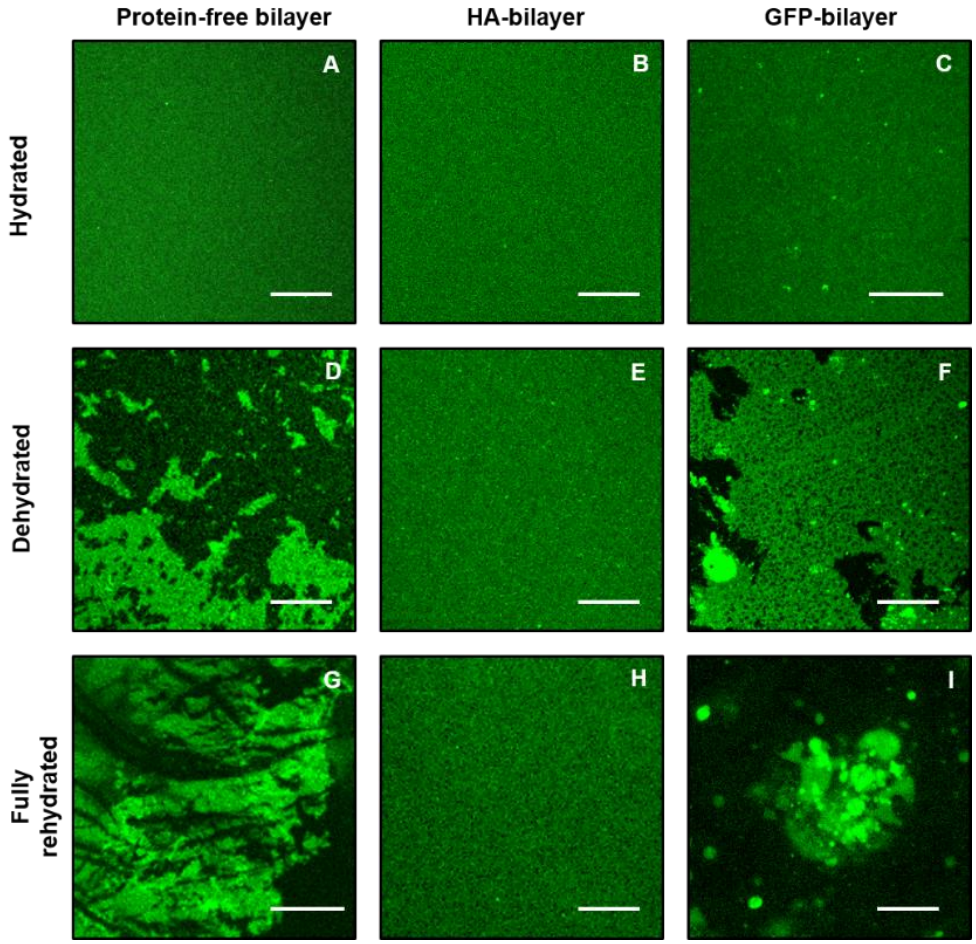

Figure 4.3. Fluorescence images of SLBs at different hydration conditions. (A-C) Representative images of hydrated SLBs DPBS buffer immediately after preparation. (D-F) Representative images of dehydrated SLBs after removal of bulk water and desiccation at 20 % relative humidity (RH). (G-I) Representative images of fully rehydrated SLBs in DPBS buffer. (A, D and G) Protein-free bilayers composed of 1,2-Dioleoyl-sn-glycero-3-phosphocholine (DOPC) 90 mol % and DGS-NTA-Ni 10 mol % and labeled with TF-PC. (B, E and H) TF-PC labeled bilayers composed of DOPC 90 mol % and DGS-NTA-Ni 10 mol % conjugated to HA. (C, F and I) 1,2-dioleoyl-sn-glycero-3-phosphoethanolamine-N-(lissamine rhodamine B sulfonyl) (ammonium salt) (Rho-PE) labeled bilayers composed of DOPC 90 mol % and DGS-NTA-Ni 10 mol % conjugated to green fluorescent protein (GFP). Fluorescence signal on G and I images were enhanced by adding 1 mM TF-PC or Rho-PE, respectively. Images were obtained in at least three independent bilayer replicates (~ 3 - 6 images for each hydration condition per replicate). Scale bars correspond to 20 μm.

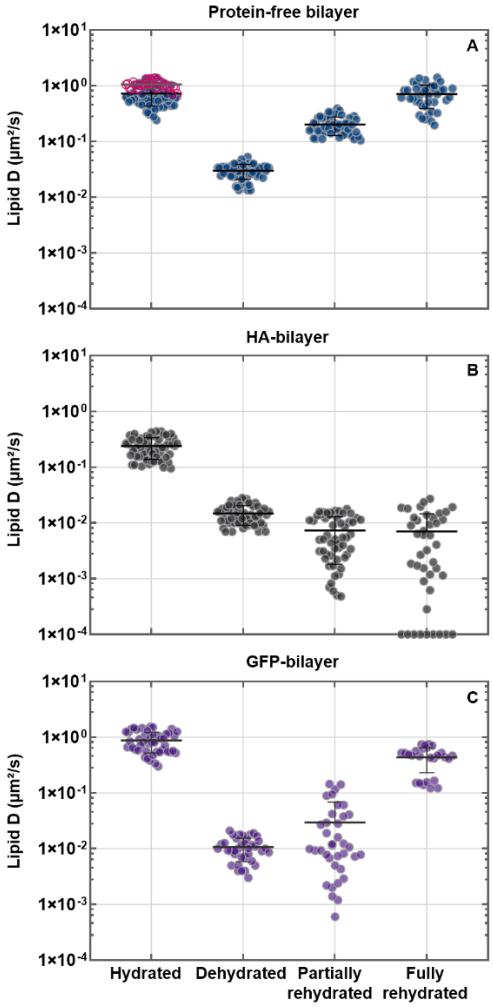

Figure 4.4. Diffusion coefficients (D) of lipids in SLBs measured via Raster Image Correlation Spectroscopy (RICS) at different hydration conditions. All examined SLBs contained DOPC 90 mol % and DGS-NTA-Ni 10 mol % and were labeled with 0.01 mol % TF-PC (A and B) or Rho-PE (C). D measured via RICS are shown for protein-free bilayers (A), bilayers containing HA (B), or bilayers containing GFP (C). Both proteins were anchored to the bilayer via His-tag and DGS-NTA-Ni. Note that the data shown in pink in (A) refer to the D of Rho-PE. Data were obtained in at least three independent bilayer replicates (9 - 12 measurements for each hydration condition per replicate). Individual points represent a single RICS measurement on one of the replicates. The horizontal lines show the mean D and the vertical lines the SD. For better visualization, D values below 1 x 10^{-4} μm²/s were set as constant and equal to this minimum threshold.

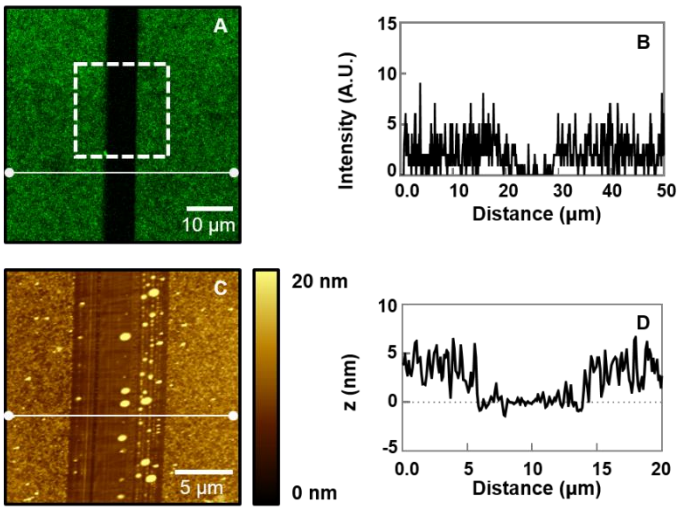

Figure 4.5. Manual scratching test performed on HA-bilayers after dehydration. (A) Representative fluorescence image of a scratched position on the DOPC 90 mol % and DGS-NTA-Ni 10 mol % SLBs labeled with 0.25 mol % TF-PC and containing HA in the dehydrated condition (comparable to Figure 4.3 E). (B) Fluorescence intensity profile extracted from the horizontal line in (A). (C) Representative Atomic Force Microscopy (AFM) topography image of the scratched sample (white square from (A)). (D) Height profile extracted from the horizontal line in (C).

4.3.2 *Fluorescence Microscopy and RICS measurements of proteins on SLBs after dehydration-rehydration cycles*

In order to obtain a more complete picture of the biophysical properties of the viral envelope models, Fluorescence Microscopy imaging was performed (**Figure 4.6**) and the diffusion dynamics of proteins (i.e. membrane-anchored HA or GFP) within the examined SLBs were analysed (**Figure 4.7**). To this aim, a small fraction of proteins was labeled as described in **section 4.2.3** and observed by Fluorescence Microscopy. RICS measurements were then performed to quantify the concentration and dynamics of the labeled proteins. The Fluorescence Microscopy images in the hydrated condition indicated homogenous protein adsorption on the SLBs both for HA and GFP (**Figure 4.6 A** and **D**). Taking into account the labeling efficiency, we could obtain the average total HA protein density on the bilayers. For this, the protein concentration in HA-bilayers was calculated by the concentration of the protein given by RICS over the labeling efficiencies of the monomer (**section 4.2.3**). We estimated ~ 1.5 x 10^3 HA monomers/µm^2 or ~ 500 HA trimers/µm^2. Similar experiments were also performed for GFP-bilayers. Assuming that ~ 60 % of the

anchored GFP is fluorescent [152][153], RICS experiments indicated an average density of ~ 1.0 x 10^3 GFP monomers/μm² in the tested samples. Finally, D were obtained for HA ((0.045 ± 0.027) μm²/s, **Figure 4.7 A** "hydrated") and GFP ((0.05 ± 0.04) μm²/s, **Figure 4.7 B** "hydrated") in the hydrated samples.

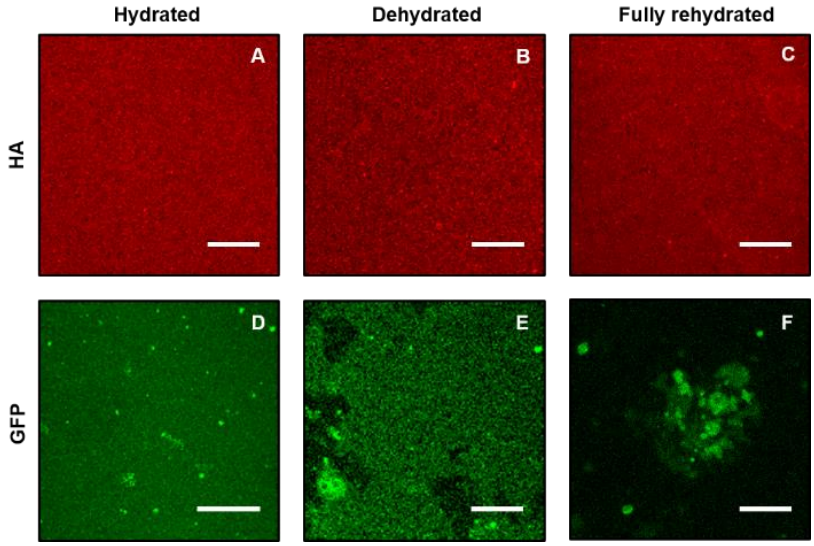

Figure 4.6. Fluorescence images of proteins in SLBs at different hydration conditions. (A and D) Representative images of proteins in hydrated SLBs in DPBS buffer immediately after preparation. (B and E) Representative images of proteins in dehydrated SLBs, after removal of bulk water and desiccation at 20 % RH. (C and F) Representative images of proteins in fully rehydrated SLBs in DPBS buffer. (A-C) AlexaFluor® 568 succinimidyl ester (A568) labeled HA conjugated to DOPC 90 mol % and DGS-NTA-Ni 10 mol % corresponding to the samples shown in Figure 4.3 (B, E and H), respectively. (D-F) GFP conjugated to DOPC 90 mol % and DGS-NTA-Ni 10 mol % corresponding to Figure 4.3 (C, F and I), respectively. Images were obtained in at least three independent bilayer replicates (~ 3 - 6 images for each hydration condition per replicate). Scale bars correspond to 20 μm.

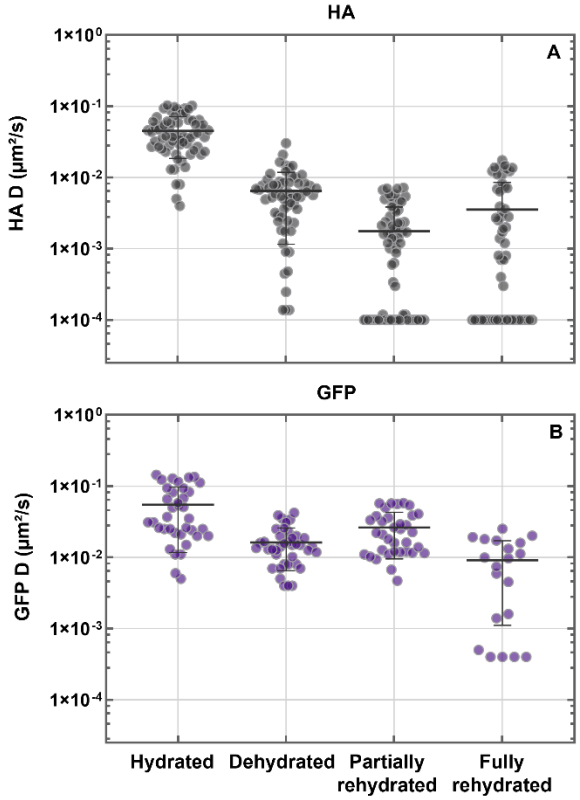

Figure 4.7. D of proteins in SLBs measured via RICS at different hydration conditions. (A) D measured via RICS for HA conjugated to the SLBs. (B) D measured via RICS for GFP conjugated to the SLBs. HA was labeled with A568 and anchored to SLBs containing DOPC 90 mol % and DGS-NTA-Ni 10 mol % and labeled with 0.01 mol % TF-PC. GFP was anchored to SLBs containing DOPC 90 mol % and DGS-NTA-Ni 10 mol % and labeled with 0.01 mol % Rho-PE. Both proteins were bound to the bilayer via His-tag and DGS-NTA-Ni. Data were obtained in at least three independent bilayer replicates (~ 9 - 12 measurements for each hydration condition per replicate). Individual points represent a single RICS measurement on one of the replicates. The horizontal lines show the mean D and the vertical lines the SD. For better visualization, D values below 1 x 10^{-4} $\mu m^2/s$ were set as constant and equal to this minimum threshold. Scale bars correspond to 20 μm.

As shown in **Figure 4.6 B**, the removal of bulk water following dehydration did not affect macroscopically the HA layer on the SLB. On the contrary, GFP protein layer was notably damaged (**Figure 4.6 E**). In terms of dynamics, sample dehydration caused an almost irreversible decrease in protein D, both for HA and GFP (**Figure 4.7** "dehydrated"). It is worth noting, though, that much slower dynamics were observed in dehydrated or partially rehydrated samples, for the case of HA-bilayers. In the dehydrated state, HA D

decreased in fact to ~ 15 % ((0.006 ± 0.005) μm²/s) while GFP D decreased to ~ 30 % ((0.016 ± 0.010) μm²/s) of the initial values. Fluorescence images of proteins in partially rehydrated samples were comparable to those obtained in dehydrated condition, as for the case of the lipid bilayers described in **4.3.1**. Also, partial rehydration led to a further decrease in HA mobility ((0.002 ± 0.002) μm²/s, **Figure 4.7 A** "partially rehydrated") but not for GFP ((0.026 ± 0.017) μm²/s, **Figure 4.7 B** "partially rehydrated"). Following full rehydration, HA-bilayers remained macroscopically unaltered (**Figure 4.6 C**) while GFP-bilayers remained spatially inhomogeneous (**Figure 4.6 F**). In these conditions, D values of (0.003 ± 0.005) μm²/s were obtained for HA (**Figure 4.7 A** "fully rehydrated") and (0.009 ± 0.008) μm²/s for GFP (**Figure 4.7 B** "fully rehydrated").

4.3.3 *Line-Scan Fluorescence Correlation Spectroscopy (LSFCS) measurements of HA on SLBs after dehydration-rehydration cycles*

RICS measurements were performed within a single frame acquisition (~ 1 s), due to the significant photobleaching observed especially after sample dehydration. Hence, information on protein dynamics could only be obtained at microsecond to millisecond time scales, which are slightly too fast, as evidenced by the rather large SDs. Furthermore, since RICS relies on a 2-dimensional spatial correlation on a larger region of the sample (compared to LSFCS which consists of a 1-dimensional spatial correlation analysis on a selected and restricted region of the bilayer), this approach can be more easily influenced by the presence of slow-moving large fluorescent objects. Therefore, RICS data were complemented by LSFCS measurements in order to obtain information on longer times scales (i.e. several seconds) and, thus, increase the statistical accuracy of the results in the case of very slow dynamics. The D of lipids determined via LSFCS were in all cases slightly higher (**Table 4.1**, **Figure 4.8 A**) compared to those obtained via RICS, as expected. Nevertheless, the general decrease of lipid dynamics upon dehydration did not differ, independently of the employed technique. In the case of fully rehydrated samples, a slight but significant ($p < 0.01$) increase in lipid dynamics could be observed compared to partially rehydrated samples at variance with the results obtained by RICS ($p > 0.20$, **Figure 4.4 B**).

Likewise in RICS (**section 4.3.2**), HA concentration was also determined by LSFCS. Here, the average total HA protein density on the bilayers was ~ 1.2 x 10^4 HA monomers/μm² or ~ 4000 HA trimers/μm². Taking into account the lower values obtained by RICS (~ 500 HA trimers/μm²), we estimate a protein surface density of at most ~ two times lower with respect to the protein density found in actual IAV envelopes. In the case of protein dynamics, similar observations were performed (**Table 4.2**, **Figure 4.8 B**). Although D values determined via LSFCS were consistently higher, both techniques indicated the same trend in the reduction of HA diffusion upon dehydration and subsequent sample rehydration.

Condition	RICS ($\mu m^2/s$)	LSFCS ($\mu m^2/s$)
Hydrated	0.24 ± 0.10	0.64 ± 0.17
Dehydrated	0.015 ± 0.006	0.026 ± 0.004
Partially rehydrated	0.007 ± 0.006	0.030 ± 0.013
Fully rehydrated	0.007 ± 0.008	0.079 ± 0.024

Table 4.1. D of lipids in HA-bilayers measured via RICS and LSFCS at different hydration conditions. All examined SLBs contained DOPC 90 mol % and DGS-NTA-Ni 10 mol % and were labeled with 0.01 mol % TF-PC. HA proteins were labeled with A568 and were anchored to the bilayer via His-tag and DGS-NTA-Ni. RICS data were obtained in at least three independent bilayer replicates (~ 9 - 12 measurements for each hydration condition per replicate) while LSFCS data were obtained in two independent bilayer replicates (~ 3 - 6 measurements for each hydration condition per replicate). Note that the table corresponds to Figure 4.4 B (RICS) & Figure 4.8 A (LSFCS).

Condition	RICS ($\mu m^2/s$)	LSFCS ($\mu m^2/s$)
Hydrated	0.045 ± 0.027	0.064 ± 0.018
Dehydrated	0.007 ± 0.005	0.016 ± 0.006
Partially rehydrated	0.0018 ± 0.0021	0.015 ± 0.004
Fully rehydrated	0.004 ± 0.005	0.013 ± 0.006

Table 4.2. D of HA proteins in HA-bilayers measured via RICS and LSFCS at different hydration conditions. All examined HA were labeled with A568 and conjugated to SLBs containing DOPC 90 mol % and DGS-NTA-Ni 10 mol % and labeled with 0.01 mol % TF-PC. HA proteins were anchored to the bilayer via His-tag and DGS-NTA-Ni. RICS data were obtained in at least three independent bilayer replicates (~ 9 - 12 measurements for each hydration condition per replicate) while LFCS data were obtained in two independent bilayer replicates (~ 3 - 6 measurements for each hydration condition per replicate). Note that the table corresponds to Figure 4.7 A (RICS) & Figure 4.8 B (LSFCS).

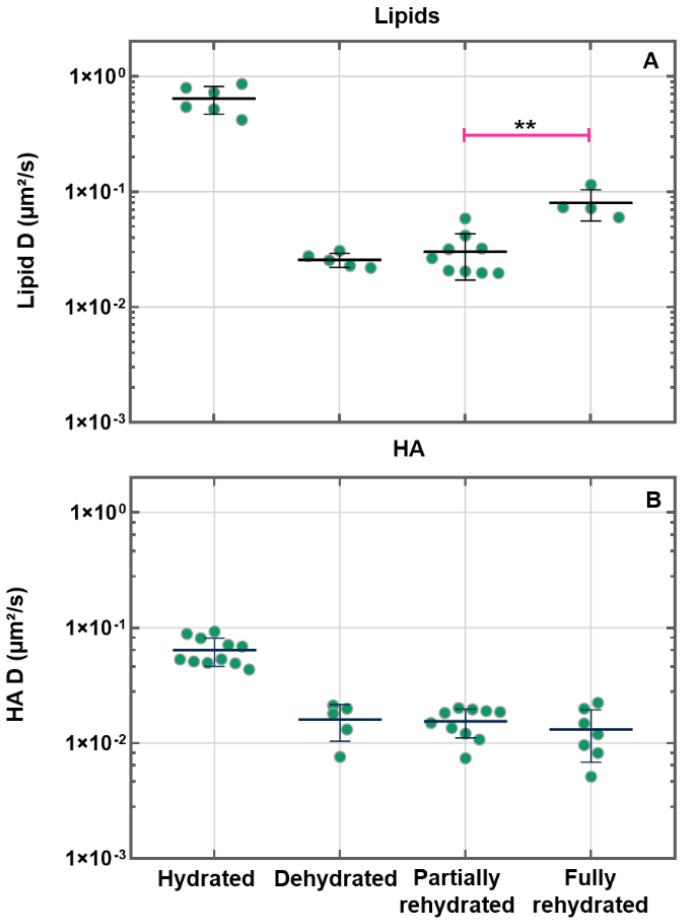

Figure 4.8. D of lipids and HA proteins in SLBs measured via LSFCS at different hydration conditions. HA was labeled with A568 and bound to SLBs containing DOPC 90 mol % and DGS-NTA-Ni 10 mol % and labeled with 0.01 mol % TF-PC. HA proteins were anchored to the bilayer via His-tag and DGS-NTA-Ni. D measured via LSFCS are shown for the lipids (A) and HA proteins (B). Data were obtained in two independent bilayer replicates (~ 3 - 6 measurements for each hydration condition per replicate). Individual points represent a single LSFCS measurement on one of the replicates. The grey horizontal lines show the mean D and the vertical lines the SD. The pink horizontal line in (A) indicates a significant but minor increase in lipid D in the fully hydrated samples with respect to the partially rehydrated condition (**$p < 0.01$).

4.3.4 *AFM scanning in water vapor*

The Fluorescence Microscopy experiments were complemented with AFM measurements, obtaining topography images and local surface characterization on the hydrated, dehydrated, partially rehydrated and fully rehydrated samples (**Figure 4.9**).

Freshly prepared protein-free bilayers appeared homogenous and flat, displaying a RMS surface roughness of (0.30 ± 0.07) nm on 5 x 3 μm^2 images (**Figure 4.9 A**). After anchoring the proteins to the SLBs, high protein density was expected to be observed, as in Fluorescence Microscopy. However, probably due to significant tip-sample interactions and the applied force to the soft surface [84] [89] [154], only few proteins anchored to the surface were observed, especially for HA-bilayers. The measured z_{max} of the single features on protein-bilayers was in average (14.7 ± 2.1) nm for HA (**Figure 4.9 B**) and (4.4 ± 1.1) nm for GFP (**Figure 4.9 C**). These results agree well with AFM studies on HA [139] [155] and GFP [156], as well as the crystal structure of the transmembrane domain of HA and the crystal structure of GFP [157] [158].

Following dehydration, topography AFM images in air were acquired. The protein-free bilayers presented major structural damage and extensive areas with uncovered glass (**Figure 4.9 D**) and – in agreement with Fluorescence Microscopy – the surface coverage decreased to (25 ± 6) %. Specifically, features with diverse sizes were observed: ~ 4 nm high patches **Figure 4.9 G**), structures with heights between 4 and 30 nm (**Figure 4.10 A** and **B**), and other objects with heights of ~ 100 nm (**Figure 4.10 A** and **C**), indicating the probable presence of bilayers patches, multi-layered lipids and lipid aggregates, respectively.

Topography images on dehydrated HA-bilayers consistently showed homogeneous samples on a macroscopic scale comparable to the fluorescence micrographs (**Figure 4.9 E** and **H**). However, at larger magnification, the high lateral resolution of AFM revealed membrane disruption (**Figure 4.10 D** and **E**). Indeed, a decrease in the surface coverage down to (61 ± 10) % was noticed. **Figure 4.11 A** is a typical representative zoom of **Figure 4.9 E** and shows homogenous distribution of nanoscale patches on the substrate of 100 - 500 nm lateral size and of ~ 4 nm height. The AFM height histograms (**Figure 4.12**) can be fitted to two Gaussian distributions, whose peak locations differ by (3.8 ± 0.6) nm, as expected for a single bilayer on a substrate, and as confirmed by the scratch and scan test (**Figure 4.13**). Note that the Gaussian fit is not required to obtain the result, but it makes sense in terms of assigning statistical height variations. Features that protrude ~ 13 nm (**Figure 4.11 A** and **B**) were also identified and might correspond to single or aggregated HA proteins anchored to the lipid bilayer.

Different from HA-bilayers, but similar to the protein-free bilayers, AFM scans on the microscale showed GFP-bilayers with extensive damage of the bilayer and exposure of the glass surface (**Figure 4.9 F** and **I**, **Figure 4.10 F** and **G**). The surface coverage was (44 ± 12) % and the height histograms from independent samples showed a large variation range that could not be fitted to a certain model. The data showed single peaks, possibly corresponding to bilayer patches, two distinguishable peaks that could be associated with

the glass surface and the dried bilayer, and even three peaks or more, probably due to residual lipids on the glass surface (**Figure 4.14**). In some areas, features of ~ 6 nm height that could correspond to GFP molecules were found (**Figure 4.11 C** and **D**). It is worth noting that quantifying the lateral dimensions of proteins in these samples was not in the scope of the investigation. Their shape is expected to be influenced by tip-sample convolution effects [84], by tip broadening as a consequence of scanning soft samples [159], and by the dynamic formation of aggregates.

For the analysis of partially rehydrated samples, the same areas as for dehydrated bilayers were scanned and zoomed in, and the surface topography between both conditions was then compared. On the protein-free bilayers (**Figure 4.9 J**), lateral expansion of the remaining lipid patches was observed, i.e. an increase in the surface coverage of ~ 15 %, as shown in **Figure 4.9 D** and **J**. Also, a large number of holes in the SLB, assigned to regions of exposed solid support, were filled, as observed by comparing the height profiles from **Figure 4.9 G** and **M** (see arrows). The HA-bilayers did not show significant structural alterations upon exposure to high humidity (**Figure 4.9 K** and **N**) while GFP-bilayers revealed membrane rearrangement in shape and height (**Figure 4.9 L** and **O**). For example, upon partial rehydration, topographic features on top of the lipid bilayer that changed in height and shape were observed (height profiles **I** and **O**). Such features can be identified as e.g. lipid aggregates swelling upon rehydration.

Finally, some topographical alterations of the protein-free bilayers and the GFP-bilayers upon full rehydration were noticed (**Figure 4.9 P** and **R**). The AFM images in protein-free bilayers revealed non-homogenous bilayer regions (**Figure 4.9 P** and **S**). Similarly, GFP-bilayers were non-uniform with defects and holes and large regions of uncovered glass (**Figure 4.9 R** and **U**). Interestingly, the high surface stiffness on fully rehydrated HA-bilayers enabled to use the same tips as for the measurements in air. This was only achieved in the HA-bilayers as in the previous cases these tips produced membrane delamination from the substrate. The fully rehydrated HA-bilayers were comparable to those in condition of dehydration or partial rehydration (**Figure 4.9 Q** and **T**). Of course, the AFM images were obtained in a different space scale with respect to the fluorescence images (**Figure 4.3 G-I**), though they only display information at the microscale which complements well the results obtained on the large scale.

Figure 4.9. AFM topography images and height profiles of SLBs at different hydration conditions. (A-C) Representative images of hydrated SLBs in DPBS buffer immediately after preparation. (D-I) Representative images of dehydrated SLBs, after removal of bulk water and desiccation at 20 % RH. (J-O) Representative images of partially rehydrated SLBs at 95 % RH. (P-R) Representative images of fully rehydrated SLBs in DPBS buffer. (A, D, J and P) Protein-free bilayers of DOPC 90 mol % and DGS-NTA-Ni 10 mol %. (B, E, K and Q) Bilayers of DOPC 90 mol % and DGS-NTA-Ni 10 mol % conjugated to HA. (C, F, L and R) Bilayers of DOPC 90 mol % and DGS-NTA-Ni 10 mol % conjugated to GFP. (G-I) Height profiles extracted from the horizontal lines of (D-F), respectively. (M-O) Height

profiles extracted from the horizontal lines of (J-L), respectively. (S-U) Height profiles extracted from the horizontal lines of (P-R), respectively. Red arrows in (M) point to changes in height with respect to (G).

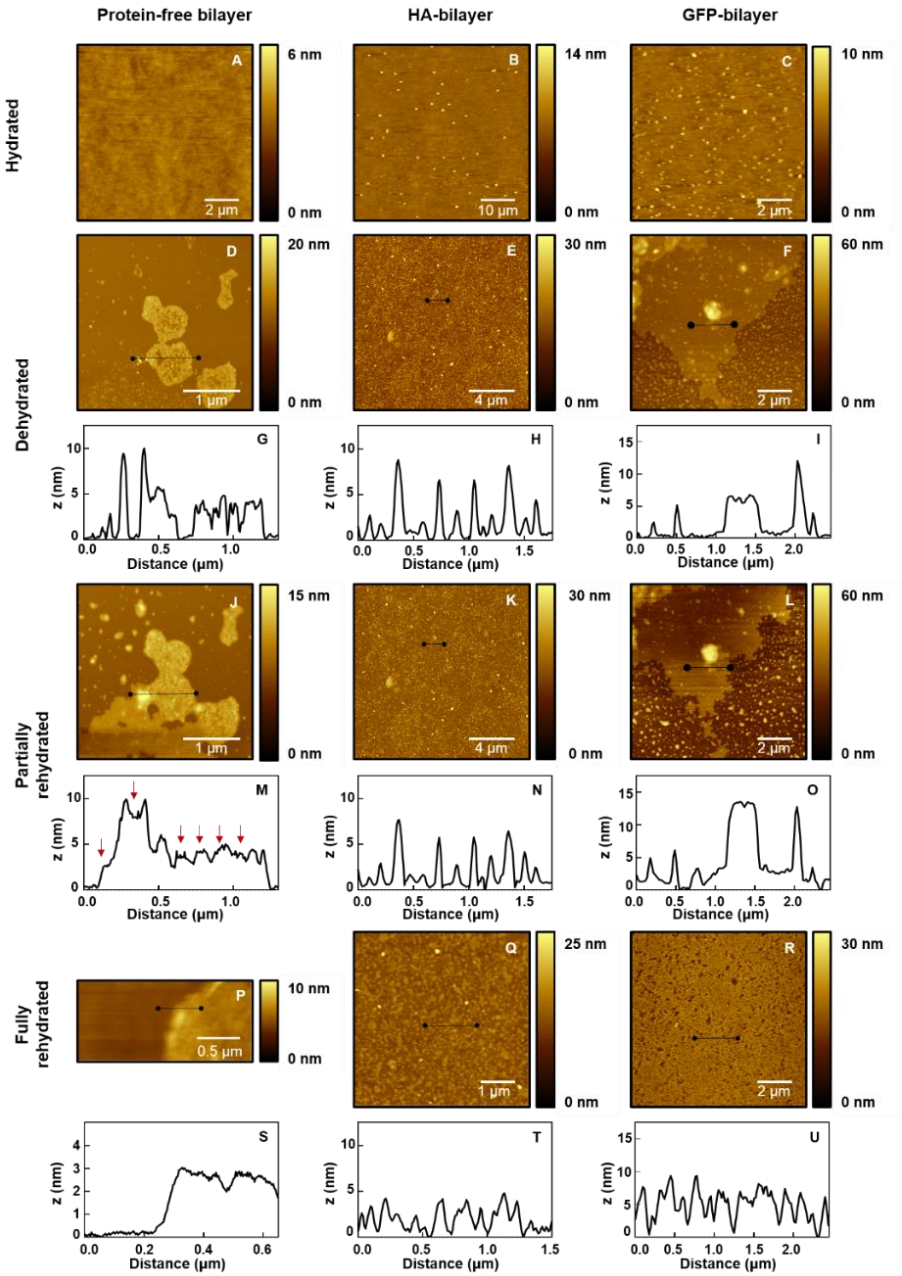

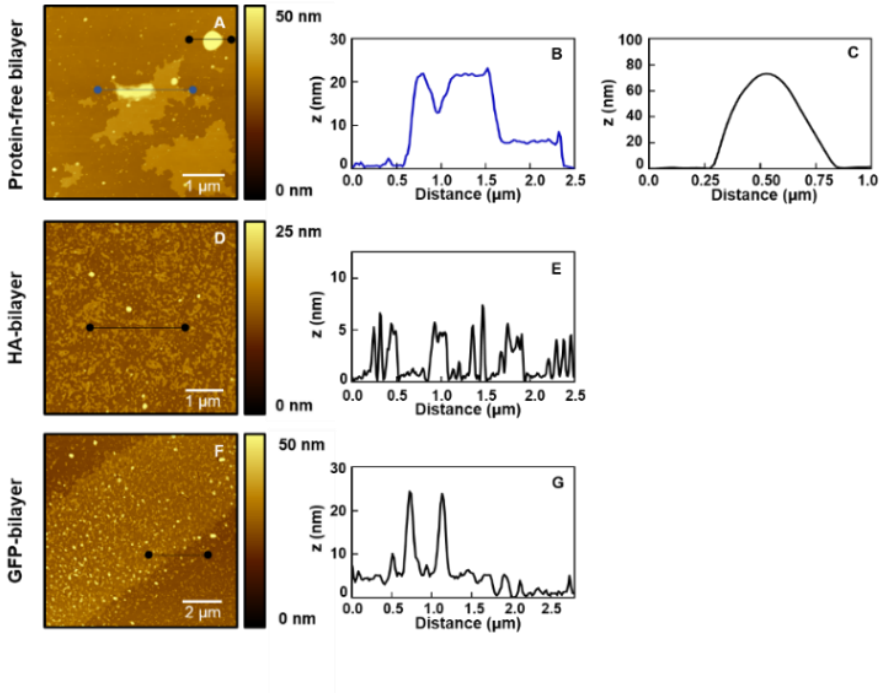

Figure 4.10. AFM topography images and height profiles of SLBs after dehydration. (A) Representative image of protein-free bilayers of DOPC 90 mol % and DGS-NTA-Ni 10 mol %. (B and C) Height profiles extracted from the blue and black horizontal lines in (A), respectively. (D) Representative image of bilayers of DOPC 90 mol % DGS-NTA-Ni 10 mol % conjugated to HA. (E) Height profile extracted from the horizontal line in (D). (F) Representative image of bilayers of DOPC 90 mol % and DGSNTA- Ni 10 mol % conjugated to GFP. (G) Height profile extracted from the horizontal line in (F).

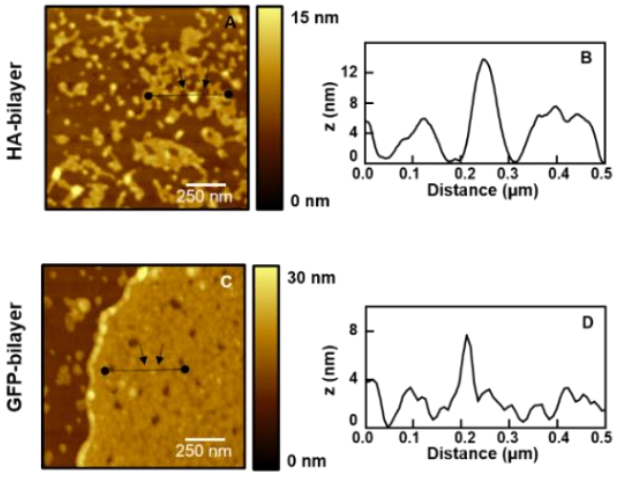

Figure 4.11. AFM topography images and height profiles of proteins on SLBs after dehydration. (A) Representative image of a SLB of DOPC 90 mol % and DGS-NTA-Ni 10 mol % conjugated to HA. (C) Representative image of a SLB of DOPC 90 mol % and DGS-NTA-Ni 10 mol % conjugated to GFP. (B and D) Height profiles extracted from the horizontal lines of (A and C), respectively. Black arrows indicate features that could be identified as proteins.

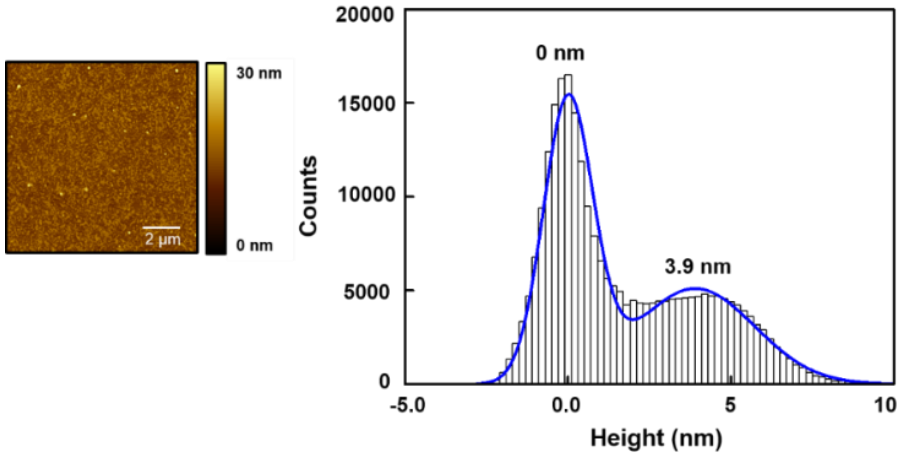

Figure 4.12. AFM topography image and height histogram of HA-bilayers after dehydration. The height histogram was fitted to a 2-peak Gaussian function (number of images, n = 16). The estimated height difference from the main peaks was considered as the depth of the lipid bilayer in the dehydrated state. Note that the height data provided by the AFM are not absolute values. Hence, we assigned arbitrarily the average height of the substrate underneath the bilayer to the value zero.

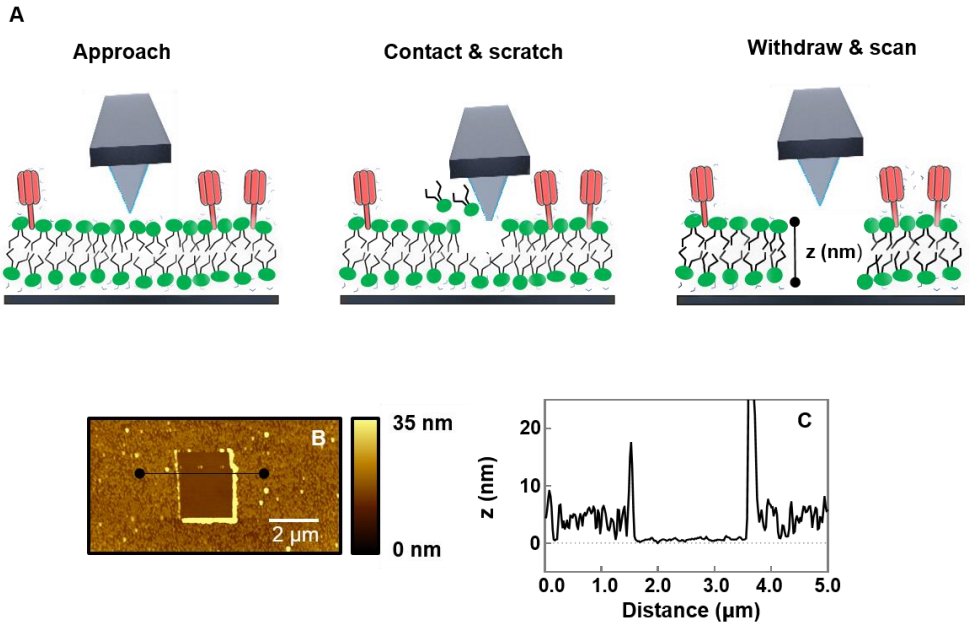

Figure 4.13. AFM scratch and scan test performed on HA-bilayers. (A) Representative scheme of the scratch and scan test: The tip approaches the sample surface till contact occurs. Scratching is performed in AFM contact mode at high setpoint values. Lately, the tip is withdrawn and the sample is scanned in tapping mode. (B) AFM topography image of a scratched region on DOPC 90 mol % and DGS-NTA-Ni 10 mol % SLB containing HA. (C) Height profile extracted from the horizontal line in (A).

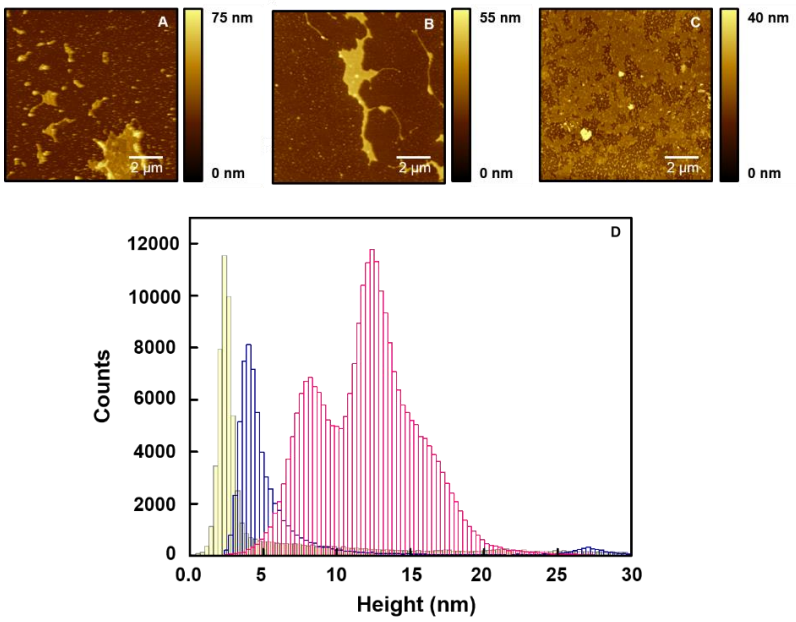

Figure 4.14. AFM topography images and height histograms of GFP-bilayers after dehydration. Representative AFM topography images of DOPC 90 mol % and DGS-NTA-Ni 10 mol % SLBs containing GFP. (A) Topography image of a GFP-bilayer corresponding to the yellow histogram exhibited in (D). (B) Topography image of a GFP-bilayer corresponding to the blue histogram exhibited in (D). (C) Topography image of a GFP-bilayer corresponding to the pink histogram exhibited in (D).

4.4 DISCUSSION

In this work Fluorescence Microscopy, RICS, LSFCS and AFM were used to study the effects of dehydration on the dynamics and structure of models of the Influenza virus envelope. The protective effects of HA at the macro- and microscopic spatial scale were specifically investigated from a biophysical point of view. The AFM and Fluorescence Microscopy setups allowed to follow controlled and reproducible dehydration-rehydration pathways on the selected hydration conditions.

The models consisted of PC lipid bilayers with HA incorporated at high concentration to mimic the IAV H1N1 envelope. In hydrated conditions, both membrane structure (**Figure 4.3 A-C**, **Figure 4.9 A-C**) and lipid dynamics (**Figure 4.4**) suggest that these bilayers are in the fluid phase [160] [161] [162]. In bilayers with incorporated proteins, the relatively slow dynamics (compared e.g. to those reported in [134]) might be ascribed to molecular crowding [163] due to high protein densities (**Figure 4.7**). Our findings

indicate that HA reduces the lipid mobility ~ 3-fold and GFP ~ 1.2-fold with respect to the protein-free bilayers. In coherence with our data, simulations on proteins at crowding exhibit a reduction in the lipid fluidity of ~ 2.5-fold relative to bulk. Also, the retardation in lipid D on membranes with large trimeric proteins is more pronounced with respect to smaller proteins (~ 60 % and ~ 40 % compared to the bulk) as exhibited for the cases of HA and GFP. These findings are probably related to steric hindrance effects that are more pronounced in larger proteins [164].

After sample dehydration, two different phenomena are observed: irreversible macroscopic disruption of the bilayers and microscopic membrane damage. Macroscopic disruption is observed in the scale of tens of micrometers while microscopic membrane damage is observed locally at the nanoscale, in less than 500 nanometer regions. The former phenomenon is hindered specifically by the presence of HA (**Figure 4.3 E** and **H**), as membranes without this protein exhibit clear structural damage (**Figure 4.3 D** and **F**). Such large-scale damage is irreversible and can be still observed also after partial or full rehydration (**Figure 4.3 G** and **I**). In protein-free bilayers, water appears therefore to induce reorganization, desorption, delamination and aggregation of lipid molecules, in line with previous results [165]. Extensive membrane damage also occurs in GFP-bilayers but not in HA-bilayers, suggesting that the protective effect on a macroscopic scale depends on the specific protein identity.

We hypothesize that the HA-induced protective effect is due to the formation of a glycoprotein-water matrix on the membrane when the protein is present at high concentrations. GFP, on the other hand, appears less prone to establish similar intermolecular interactions. HA is a trimeric glycoprotein rich in surface glycans with a high mannose content. It also contains more complex and branched glycans [166]. Surface glycans increase the overall stability of the proteins in solution [167] and mannosyl derivates were shown to support protein integrity upon freeze-drying or desiccation [168] [169]. Furthermore, AFM experiments indicate that mannobiose monolayers present strong self-adhesion forces which, in turn, may play a role in water structuring and retention of a water layer upon bulk dehydration [127]. Finally, exposure of certain organisms to extremely low humidity conditions can induce a so-called "anhydrobiosis" state, a condition in which high contents of trehalose, sucrose or other disaccharides are produced to avoid cell death [170]. While not providing direct evidence regarding the molecular mechanism, our experiments suggest that the high density of surface glycans in HA might be responsible for the formation of a rigid molecular matrix that retains water molecules and allows membrane preservation upon dehydration. A similar effect was previously reported for lipid bilayers which were preserved in dehydrated conditions by a layer of disaccharides [171], monosaccharides [172] or the presence of trehalose glycolipids [173].

Similar findings on the creation of air-stable membranes by protein crowding were reported by Holden et al., [174]. In their study, the addition of maximized ligand density

of streptavidin on biotinylated bilayers preserved the membrane after exposure to air. In stark contrast to our data, using other proteins as immunoglobulins G (IgGs) produced the same effect indicating that the protein's identity may not be determinant for membrane protection. Of interest, both streptavidin and IgGs are glycosylated proteins and the potential influence of the glycan composition on the results was not discussed. The type of interaction between the proteins and the bilayer also differs. Biotin-avidin binding is one of the strongest non-covalent interactions in nature (Kd ~ 10^{-15} M) [58], but Ni/His-tag interactions are comparatively weak (Kd ~ 10^{-6} M) [57]. Although this is not direct evidence, this may influence the dynamics and structure of the protein matrix after dehydration.

The second type of damage (i.e. microscopic membrane damage) is observed regardless of the membrane composition and the presence of proteins. Water removal induces a phase transition into a gel state [175] and a decrease in the lipid area per headgroup [176], resulting in membrane shrinkage, exposure of the glass substrate and reduction of the total surface coverage of the bilayers (**Figure 4.9 D-F**). As a consequence, we observed the formation of microscopic membrane defects which might not be necessarily connected to actual loss of lipids. These small discontinuities in the membrane might further hinder residual lipid diffusion (**Figure 4.4**) as also reported before [133]. Protein D decreased as well during dehydration, albeit only limitedly, probably due to the already slow dynamics in crowded hydrated samples (**Figure 4.7**).

Upon rehydration, microscopic membrane damage appears reversible in protein-free bilayers and in GFP-bilayers. The reintroduction of bulk water favors the rearrangement of lipids on the membranes, resulting in membrane expansion over the glass surface[177] and, possibly, a phase transition back to the liquid-crystalline state [178]. In agreement with our quantification of lipid dynamics (**Figure 4.4**), the re-establishment of membrane fluidity allows small defects to be repaired and membrane self-healing thus occurs at the micrometric scale (**Figure 4.9 J, L, P** and **R**). This local process does not appear to be influenced by large-scale irreversible macroscopic disruption on the bilayer, as reported in analogous investigations [179]. The larger data spread observed for lipid or protein D in protein-containing SLBs suggests that these samples are spatially inhomogeneous. These might be artificially enhanced by performing a single frame scanning by RICS where the quality of the collected data is compromised [82]. Results on LSFCS support this hypothesis, as the data variability in HA-bilayers decreases when increasing the time scale of the measurement (**Figure 4.8**, **Table 4.1**, **Table 4.2**).

On the other hand, HA-bilayers exhibit irreversible microscopic membrane damage. Rehydration does not change the apparent structure of the bilayers (**Figure 4.9 K** and **Q**) as the samples remain comparable to the dehydrated state. Also, lipid and protein dynamics are only marginally recovered (**Figure 4.4**, **Figure 4.7**, **Figure 4.8**). One possible explanation is that a rigid matrix of intermolecular interactions between the remaining water molecules and surface glycans of HA stabilizes the bilayer in a solid gel state. Such a bilayer phase is induced by dehydration (as also observed in protein-free and GFP

bilayers), but is not reversed by rehydration. Of interest, a suppression of gel to liquid-crystalline phase separation during membrane rehydration was associated to the prevention of content leakage from lipid vesicles [178].

In our model of the IAV H1N1 envelope we tested the protective effects of the HA ectodomain at crowding conditions. The quantification of protein concentration via Fluorescence Microscopy indicates that our model of the IAV H1N1 envelope contained HA at relatively high density (~ 10^3 - 10^4 HA monomers/μm^2), but still at most ~ two times less packed than in actual virions [26]. This suggests that the effects observed in bilayers due to protein-protein interactions are likely also relevant in the context of a viral envelope. In addition, in order to focus on the role of HA ectodomains, the effects of transmembrane and cytoplasmic domains on membrane stability were not considered in this model, since the protein was directly linked via Ni/His-tag to the bilayer. Also, one should note that the inner leaflet of the IAV membrane is bound to the matrix protein 1 (M1), which forms a dense matrix that affects the envelope stability [33] and is absent in our models of the viral envelope.

In this research, the IAV H1N1 model envelope probably undergoes a transition from fluid phase to solid state upon dehydration. It is worth noting though that IAV lipids are more likely to be found in a solid gel-like state rather than in a fluid disordered phase, already when fully hydrated [180] [39]. This is due to the fact that the viral envelope is highly enriched in PE and PS with much lower amounts of unsaturated PC, compared e.g. to the plasma membrane of the host cell [181] [182]. On the one hand, the fact that our model envelope is in the fluid phase in hydrated samples allows us to monitor protein and lipids dynamics as a function of water content. Also, the protective effects of HA are clearly distinguished with respect to e.g. IAV like-bilayers where the heterogeneous composition and phase separation may influence the data interpretation. On the other hand, this represents a limitation of our system since the observed fluid-to-solid phase transition might not occur in IAV virions upon dehydration. We hypothesize therefore that the irreversible microscopic membrane damage that we see in our samples does not play a major role in the process of virus survival at low humidity. In contrast, our data suggest that HA might play a fundamental role in protecting the virus envelope from large-scale damage and disintegration during dehydration, in agreement with membrane shrinkage reported in respiratory droplets [5] and sustained virus infectivity in aerosols at variable humidity [42].

4.5 CONCLUSIONS

This investigation exhibits a novel approach to investigate the biophysical properties of IAV H1N1 envelope under different hydration conditions from the macro- to the microscale. While the developed model is mainly limited by the specific membrane composition, the results indicate that HA might act as a membrane protectant upon

dehydration. This observation provides new insights regarding the molecular mechanisms determining virus stability and survival outside living cells. In general, the experimental approach presented here takes advantage of the synergy between AFM and Fluorescence Microscopy since the two techniques provide spatial information on different spatial scales. Also, the AFM and Fluorescence Microscopy setups enable to follow dehydration-rehydration cycles in a controlled and reproducible manner. More complex experimental setups might be used in future studies as testing temperature variations within humidity changes. Also, the role of specific lipids and surface glycans in determining the interactions between viral envelope and water molecules may also be addressed in future investigations.

Chapter 5

Examining the surface structure of Influenza A virus in air

This is the most explorative chapter of the thesis, it is focused on revealing the structural features of Influenza A H1N1 virus envelope at the nanoscale. Live attenuated Influenza vaccines were investigated by Atomic Force Microscopy and the adsorption on gold, silicon and polymethyl methacrylate was assessed. The results from this investigation show that there is a dependence on the adsorption of the vaccine components with the type of substrate. Although the scanning in air did not allow to obtain a detailed structure of single Influenza A H1N1 envelope, complete assembled viruses in the range of 100 nm were identified.

5.1. INTRODUCTION

In the previous chapters of this thesis, the use of simplified but accurate model systems to study the effect of humidity on Influenza A virus (IAV) envelope was developed. These approaches have proven new insights in the molecular stability of the virus at variable humidity. For instance, the dimannoside residues found on the surface glycoproteins hemagglutinin (HA) and neuraminidase (NA) may play a primary role in water retention after dehydration, while HA is involved in providing protective effects upon dehydration stress.

Despite these progresses, the mechanism of virus survival and stability at low humidity is still an open question and needs to be addressed using a more realistic model. On the one hand, working with the wild type virus in natural environments might be the most attractive strategy, not only from the biophysical interpretation of virus morphology but also to develop novel solutions to interfere with transmission. On the other hand, this approach is in general not a straightforward option, as the high virus spread, re-assortment and mutation rate represent a significant threat to humans [183] and inhibit to perform studies in conventional laboratories.

A simplified attempt is to mimic the entire virus envelope with the virus genome inactivated or weakened, which is in fact one of the main strategies in vaccine development. This can be achieved using virus-like particles (VLPs) [184], inactivated viruses [185] or live attenuated viruses [186]. Among them, inactivated Influenza vaccines (IIVs) and live attenuated Influenza vaccines (LAIVs) have been the most important, safe and cost-effective counter-measure to combat influenza disease, since their implementation seventy years ago [60].

Owing to the lack of replication, IIVs provide specific antibody-mediated protection, which is short lived due to an inactivation process. LAIVs are based on the introduction of temperature sensitive and attenuating mutations in internal protein gene segments [59]. This weakens the virus, but does not inactivate it. Therefore, LAIVs can mimic a natural infection by eliciting protective antibodies both locally and systemically, as well as induce cellular responses [60]. They preserve the viral structure after attenuation and can offer a safe source of virus strains – from monovalent to quadrivalent compositions – resulting in ideal candidates to perform biophysical studies on the virus envelope.

Referring briefly to the surface structure (**section 1.2.1**), IAVs are polymorph, mostly about spherical (80 - 120 nm in diameter), but also filamentous in shape (up to 300 nm length) [31]. The virus structure is contained within a lipid bilayer envelope, which contains the viral glycoproteins HA and NA, and the matrix 2 ion channels (M2) [187]. HA and NA are transmembrane proteins present in the ratio of approximately four to one. The trimeric HA forms "spikes" at the viral surface that protrude approximately 14 nm from the membrane. The tetrameric NA has a long-stemmed "mushroom-like" shape that

protrude approximately 16 nm into the extraviral space. A smaller number of M2 ion channels traverse the lipid envelope, with an HA:NA:M2 ratio of ~ 400:50:20 [32].

Atomic Force Microscopy (AFM) is a valuable tool to explore single virus structure in ambient conditions and can complement biological assays with fundamental investigation on wetting. This involves the role of adsorbing surfaces, confinement effects and high resolution imaging. In this research, intermittent contact AFM was used to elucidate the adsorption mechanism of a monovalent LAIV on solid surfaces, and physical interpretations in terms of single virus morphology were developed.

5.2. MATERIALS AND METHODS

5.2.1 *Materials*

Acetone (99.5 %) was purchased from Sigma-Aldrich (Steinheim, Germany). 2-propanol (99.5 %) was obtained from Acros (Geel, Belgium) and absolute ethanol (99 %) from Panreac (Castellar del Vallès, Spain). Deionized, filtered water (referred as "Milli-Q", specific resistance 18.2 $M\Omega cm^{-1}$, TOC (total organic content) < 10 ppb) was obtained by an Advantage System Millipore (Burlington, USA). Seasonal attenuated IAVs H1N1 (A/Bolivia/559/2013, non-hazardous, non-infectious) were kindly donated and were used without any further purification. The sample consisted of a monovalent vaccine in solution. The concentration and overall composition of the vaccine were not detailed.

5.2.2 *Sample preparation*

LAIV samples were adsorbed on silicon, gold and spin-coated polymethyl methacrylate (PMMA) on silicon substrates. Prior to sample adsorption, the wafers were chemically cleaned by successive serial sonication steps of 5 minutes each using acetone, 2-propanol and absolute ethanol and then dried with a nitrogen stream. Later, the samples were adsorbed. For this, a 10 μL droplet of sample was deposited on the substrates and incubated for 10 minutes. Afterwards, the droplet was withdrawn and the remaining liquid was dried in ambient conditions, thus avoiding washing steps. The procedure was done at room temperature (23 - 25 °C) inside a laminar flow cabinet in biosafety level 2 (BL2) laboratory.

5.2.3 *Contact angle measurements*

For static contact angle measurements, sessile drop experiments were performed in duplicate samples at ambient temperature (23 - 25 °C) with a standard contact angle measurement system (G10 goniometer, Krüss, Germany). A droplet of deionized, filtered

Milli-Q water of volume 4 μL was placed onto the substrates, and contact angles from the drop profile were measured.

5.2.4 *AFM measurements*

AFM topography and phase images were achieved by using an Agilent 5500 AFM (Keysight, Santa Clara, USA). Images of 256 x 256 pixels and 512 x 512 pixels were recorded in air in tapping mode at 24 °C, at speed rates between 0.9 and 1.2 lines per second and 0.2 and 0.6 lines per second, respectively. The phase images were manually calibrated by adjusting the phase contrast to the topography scans. The scanning was performed in at least two replicates per substrate. Silicon cantilevers (Multi-75, Budget Sensors, Sofia, Bulgaria) with a nominal radii of < 10 nm, force constant of 3 N/m and resonance frequency of 75 kHz were used for the experiments, regardless the selected substrate.

The images were examined by using picoView 1.14 software (Keysight, Santa Clara, USA). AFM images were analyzed after scanning with WSxM 5.0 Develop software version 8.4 [102] for obtaining the full width at half maximum (FWHM), maximum height (z_{max}) and height profiles of the sample specimen. The images were processed by levelling the plane of the image and applying parabolic flattening. Single viruses were manually selected by applying a criteria of single virus observation with a FWHM and z_{max} between 80 - 120 nm.

Gwyddion software version 2.47 (Gwyddion, Brno, Czech Republic) was used for displaying the topography images. The images were first levelled by mean plane subtraction, aligned by height median and the z-excursions outliers were manually removed by, e.g. correction of the scan line artefacts in the x-axis or misaligned segments within a single row. The height profiles were obtained with GraphPad Prism version 8.0.1 for Windows (GraphPad Software, San Diego, USA). The data were displayed as the mean ± standard deviation (SD).

5.3. RESULTS

5.3.1. *LAIV adsorbed on flat substrates*

LAIV samples were adsorbed on silicon, gold and PMMA and information on the sample adsorption was extracted by AFM measurements. Prior to sample deposition, the contact angle of Milli-Q water on gold was determined to 40 ± 1°, on silicon to 63 ± 4° and on PMMA to 63 ± 2°, indicating in the three cases hydrophilic substrates at the microscale (**section 2.1**).

As observed in previous studies (**section 3.3.3**) the adsorption depended on the chemical nature of the substrate. Although the active substance of the vaccine used in this study was the IAV strain A/Bolivia/559/2013, the stabilizing components, excipients and

co-adjuvants were not reported. In general, LAIVs present traces of sucrose, dipotassium phosphate, potassium dihydrogen phosphate, gelatin, arginine hydrochloride and monosodium glutamate monohydrate which are diluted in water to be nasally administered [188]. From this, the complex composition of the vaccine was reflected in a highly heterogeneous adsorption in all the tested conditions (**Figure 5.1** and **Figure 5.2**).

The sample adsorption on gold and silicon exhibited coffee ring phenomena (refer to **section 3.3.3**) after deposition and drying at the microscale (**Figure 5.1 A** and **D**, respectively). To avoid tip contamination, AFM imaging was performed outside the droplet. Three types of structures were mainly found: 1) features with heights below 20 nm, 2) features in the range of 20 - 60 nm, and 3) features between 80 - 120 nm.

On gold, the structures below 20 nm varied in size and shape and were frequently observed (**Figure 5.1 B** and **Figure 5.2 A**). The features between 20 - 60 nm were generally spherical, appeared in clusters or as individuals and were directly observed on the substrate (**Figure 5.1 B** and **Figure 5.2 B**) or above/immersed in layers of ~ 10 - 20 nm height (**Figure 5.1 C** and **Figure 5.2 D**). These structures presented a z_{max} of 36.2 ± 5.1 nm (number of objects, n = 21) when directly adsorbed to the substrate. Objects between 80 - 120 nm were directly adsorbed on the substrate and showed – in general – no agglomeration (**Figure 5.1 B** and **Figure 5.2 C**).

On silicon, although the same type of structures was observed, a predominance of individual spherical molecules in the range of 20 - 60 nm was noticed. As in the case of gold, these structures were adsorbed directly on the wafer (**Figure 5.1 E** and **Figure 5.2 E**) presenting a z_{max} of 33.6 ± 5.1 nm (n = 51) or on top or immersed in layers of ~ 10 nm height (**Figure 5.1 F** and **Figure 5.2 F**). Structures with lower heights were also present but less frequent with respect to gold, while protusions in the range of 80 - 120 nm were very rare.

The adsorption on PMMA was markedly different. Although the coffee ring phenomena was also observed, a more uniform sample adsorption and less agglomerated species were noticed inside the droplet (**Figure 5.1 G**). Yet, AFM images were performed outside the confined sample. A uniformly spread layer with defects and holes of ~ 2.5 - 8.0 nm steps was detected on the substrate and generally the structures were found above the layer (**Figure 5.1 H** and **I**, **Figure 5.2 H** and **J**). These objects varied in height, from ~ 10 nm (**Figure 5.2 I)** to ~ 120 nm (**Figure 5.2 G**) and were found as single species and in lower frequencies in agglomerated state.

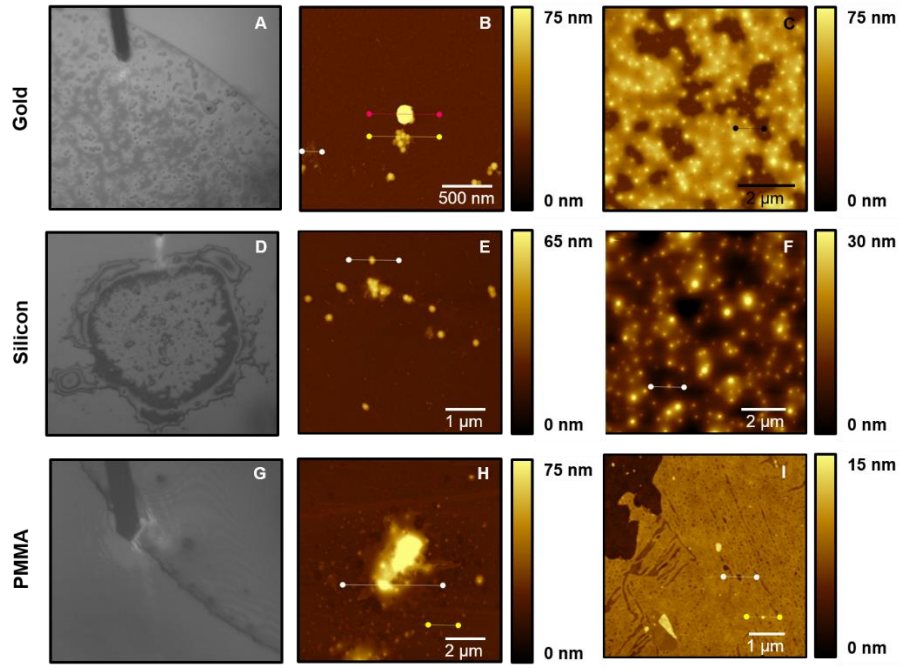

Figure 5.1. Representative Atomic Force Microscopy (AFM) images of a live attenuated Influenza vaccine (LAIV) on gold, silicon and polymethyl methacrylate (PMMA) in air at ambient conditions. (A, D and G) Optical images on gold, silicon and PMMA, respectively before AFM measurements. (B and C) Topography images of the sample adsorbed on gold. (E and F) Topography images of the sample adsorbed on silicon. (H and I) Topography images of the sample adsorbed on PMMA.

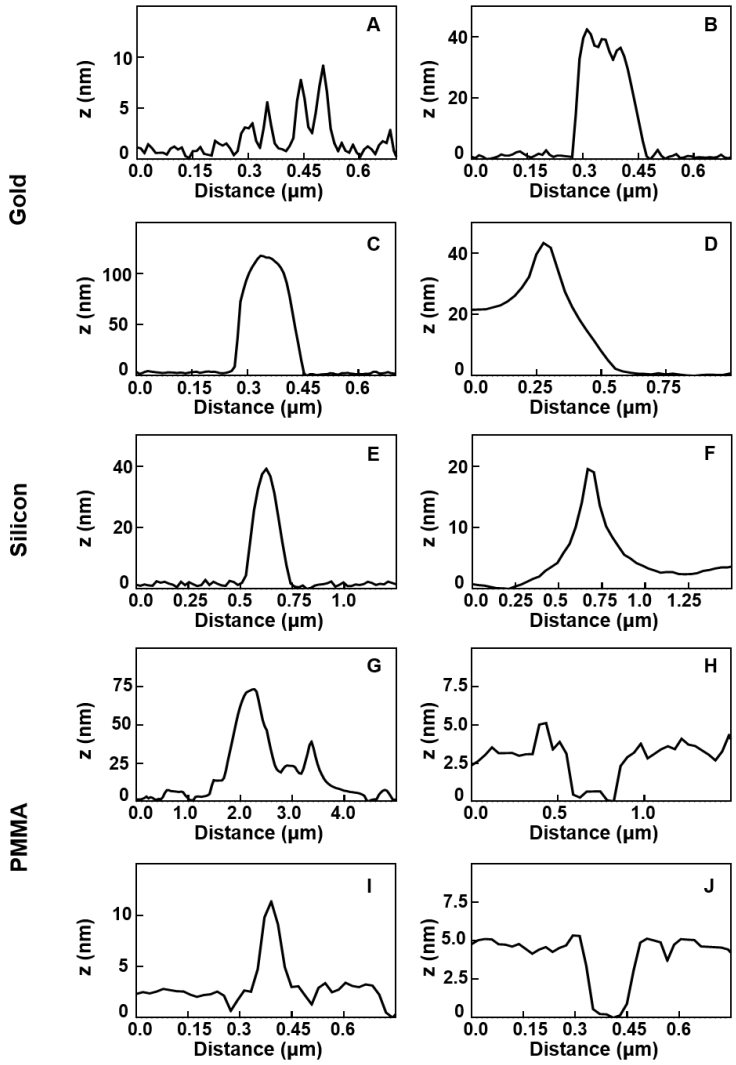

Figure 5.2. **Representative AFM height profiles of a LAIV on gold, silicon and PMMA in air at ambient conditions**. (A, B and C) Height profiles extracted from the white, yellow and pink horizontal lines in Figure 5.1 (B), respectively. (D) Height profile extracted from the black horizontal line in Figure 5.1 (C). (E) Height profile extracted from the horizontal line in Figure 5.1 (E). (F) Height profile extracted from the horizontal line in Figure 5.1 (F). (G and H) Height profiles extracted from the white and yellow horizontal lines in Figure 5.1 (H), respectively. (I and J) Height profiles extracted from the yellow and white horizontal lines in Figure 5.1 (I), respectively.

5.3.2. *IAV envelope morphology*

After assessment of the LAIV adsorption on different substrates, we focused the research on revealing the structural features of complete enveloped virus at the nanoscale. Taking into account the diameter of a spherical virus of 80 - 120 nm [35] [26] [189], AFM measurements were performed in air on isolated structures with morphologies that corresponded to the reported size. For this, the experiments were performed on gold and PMMA at small scan areas and low speed (**Figure 5.3**). It is commonly understood that each type of virus has a substrate preference [189]; hence, AFM measurements were not achieved on silicon as the frequency to find individual molecules in the reported range was almost zero. Topography and phase images were obtained to achieve a more complete picture of the virus envelope. From the topography images, one can observe the main structural features i.e. size, shape, and morphology. Phase images may highlight physical properties (i.e. mechanical properties) that are not readily discernible in the topographic map. For instance, fine morphological features and interactions between the tip and the sample are, in general, better distinguished in phase images [83] [190].

In coherence with previous AFM studies on Influenza X-31 virus [21], **Figure 5.3 A** shows a scanned object on gold with FWHM of 130 nm and a z_{max} of 112 nm (**Figure 5.3 C**). From the topography images, some protrusions were noticed on the scanned object, however they were not easily distinguished neither by the color map nor by the height profiles. Phase images complement these findings as one can observe the protrusions by changes in the phase contrast (**Figure 5.3 B,** pink arrows). Also, the uniform phase signal from the substrate – which is different from the scanned object – indicates that the molecules are directly adsorbed on the surface. Still, a detailed quantitative analysis of the scanned object is not possible (e.g. height quantification of the protrusions) due to the high contribution of adhesion forces between the tip and the sample, and scanning artifacts like tip geometrical convolution (**section 3.3.4**), tip/sample damage (or contamination) provided by scanning in air [86] [191].

The topography images on PMMA also exhibited corrugated objects in the range of 80 - 120 nm with some protrusions onto the scanned structures. The features were not found as individuals but immersed in cross-linked networks or meshes of ~ 4 nm height, which were not observed in the gold substrates (**Figure 5.3 D**). This was in coherence with the results obtained in the previous **section 5.3.1.** The protrusions were also distinguished by the phase images as well as the network on the substrate (**Figure 5.3 E**). The same phase signal was found on top of the scanned objects and the features on the substrate (**Figure 5.3 E,** light blue arrows), suggesting the same type of interactions between the tip and both components. Likewise in gold, the conditions of the experiment did not allow to obtain a detailed quantitative analysis of the scanned samples but an overview of the size, shape and surface morphology (**Figure 5.3 F**).

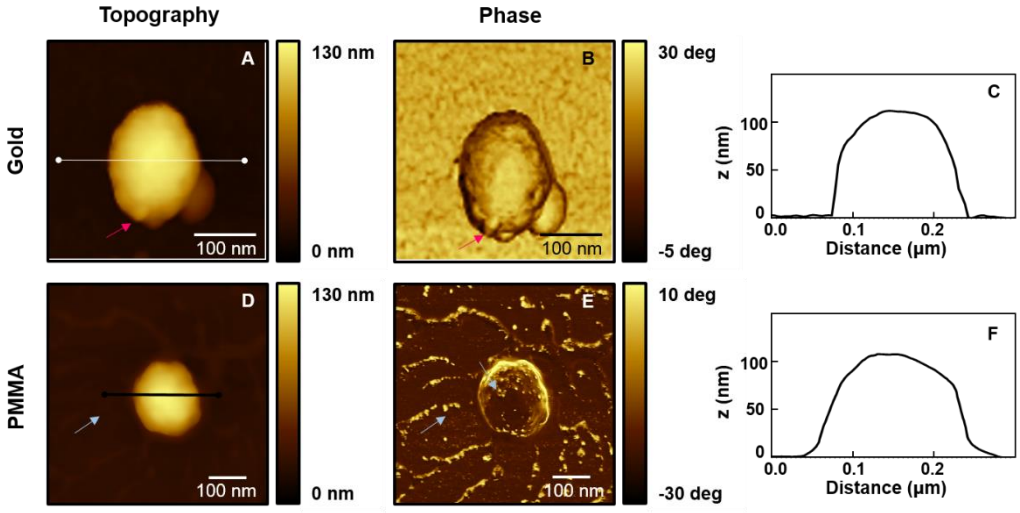

Figure 5.3. Representative AFM images and height profiles of Influenza A virus (IAV) envelope in air at ambient conditions. (A and D) Topography images. (B and E) Phase images. (C and F) Height profiles obtained from (A and D), respectively. Note that images (A and B) were obtained on gold while images (D and E) were obtained on PMMA. Pink arrows indicate protrusions detected in the topography and phase images in (A and B), respectively. Light blue arrows indicate protrusions detected in the topography and phase images in (D and E), respectively.

5.4. DISCUSSION

In this research, the possibility to study the surface morphology of IAV envelope by using a monovalent LAIV was explored. The reason for selecting this type of sample is to guarantee the use of non-hazardous and non-infectious viruses to be easily analyzed by standard biophysical methods, allowing the possibility to perform surface studies in air at varying humidity conditions. Here, the samples were tested in air at ambient conditions. In analogy to the previous research developed in **Chapter 3**, this corresponds to "medium humidity" conditions equal to (50 ± 5) % of relative humidity (**section 3.2.10**).

The adsorption of LAIV samples on diverse substrates was assessed by AFM imaging and the surface structure of a complete IAV was attempted to be examined. Likewise in **Chapter 3** from this thesis (**section 3.3.3**), the results show that the adsorption of the sample depends on the nature of the substrate. We used flat substrates chemically different but with similar hydrophilicity at the microscale. The samples were adsorbed by physisorption, thus avoiding the formation of chemical bonds that may alter the structure of the sample components [189]. Irrespective from the nature of the substrate, the deposition method resulted in coffee ring phenomena [119]. The adsorption was

performed by incubation of a droplet and later withdrawal without washing steps. Since the sample was used as received by the manufacturer, traces of salts and stabilizing components above the micrometer range were observed (**Figure 5.1 A**, **D** and **G**). Therefore, they might have influenced in the water evaporation rate, explaining the observed coffee ring phenomena (for further details refer to **section 3.3.3** and **section 3.4**).

At the nanoscale, different features were observed. These were in general very difficult to interpret. In all the tested substrates, structures below 20 nm in height were found mainly as cross-linked or porous networks (**Figure 5.1 C** and **F**, **Figure 5.2 D** and **F** and **Figure 5.3 D** and **E**). The complex composition of LAIVs encloses water-soluble biomaterials as gelatin or stabilizing disaccharides [188] that can interact with the substrate and also with the virus itself. Gelatin, for instance, is a protein derived from collagen, with the capacity to form network structures and cross-linked porous gels. For a certain concentration, the final conformation that the substance adopts depends on the gelation process, trigged by changes in temperature over time [192]. In general, the height of gelatin films or fibers is in the range of tens of nanometers [193]. We therefore hypothesize the presence of a porous network on the tested substrates due to gelatin.

In PMMA, along with the cross-linked or porous networks, uniformly spread layers of steps between ~ 2.5 – 8.0 nm were noticed (**Figure 5.1 H** and **I** and **Figure 5.2 H**-**J**). These features might be linked to another type of component and fit well with lipid bilayers or multi-layered lipids (**section 4.3.4**) from – possibly – the IAV lipid membrane. In this sense, to observe such features, virus disassembly might occur as a consequence of sample adsorption (in solution) or due to the dehydration process. The molecular mechanisms involved here cannot be determined from our data, as AFM imaging was only achieved after sample dehydration.

The adsorbed samples also exhibited objects in the range of 20 - 60 nm in height, which were more evident on silicon substrates. The observed morphology can be connected to virus compression after dehydration due to water evaporation and/or strong and maximized interactions between the sample and the substrate. Studies on X-31 strains have shown that dehydration might decrease the surface stiffness of the envelope and affect the diameter and morphology; even though some virus remain comparable to the initial values in solution [21]. To our knowledge, the envelope diameter measured by AFM results in minimal values in the order of ~ 60 nm [21], which might not fit to our data. Of course, this interpretation is merely hypothetical as the exact composition of the sample and virus concentration is unknown.

Finally, the sample contained mostly "spherical" structures of 80 - 120 nm but not elongated objects. These are in coherence with single IAVs. Zoom into these structures enabled to observe that the viral particles are corrugated (**Figure 5.3 A** and **B**); these corrugations probably correspond to the HA and NA proteins, the major protein components of the virus envelope. Another option is artificially aggregated proteins by the tip during scanning, as the IAV envelope surface stiffness is relatively low (~ 0.02 N/m)

when comparing with other encapsulated viruses as human immunodeficiency virus (~ 3.15 N/m on the immature virion) or non-enveloped viruses as tobacco mosaic virus (~ 0.80 N/m) [194]. Also, the tip could not delineate individual molecules, protein domains or assemblies, typically found in IAV AFM images in liquid (solution) [187]. Thus, the lateral segregation of the proteins as well as the dimensions in the viral membrane could not be quantified. A possible explanation for this discrepancy is the well-known limited lateral resolution of the tip (radius ~ 10 nm) which is similar to the transmembrane glycoproteins domains (~ 14 nm for HA and 16 nm for NA) causing geometrical convolution effects (**section 3.3.4**). Also, the densely packed proteins [195] [26] might inhibit a straightforward scanning, as the tip cannot properly trace the high aspect-ratio glycoproteins. This is bolstered by scanning in air, which may result in a low resolution of the virus structure [84]. Indeed, generally AFM scanning on viruses are achieved in liquid environments (solution) not only to mimic their natural environments, but also to avoid adhesion forces between the tip and the sample (primarily capillary forces). These forces may cause sample damage or deformation as well as slow scan rates [86] [189], as actually performed in our experiments. Nonetheless, the finding of ~ 100 nm diameter corrugated viruses after sample dehydration provides a good indication on the high stability of the IAV envelope after water withdrawal and evaporation. Still, the exact composition of the monovalent LAIV requires to be clarified since stabilizing components like disaccharides or salts might act as a protective agents upon dehydration [171].

5.5. CONCLUSIONS

This research exhibits an alternative method to investigate the biophysical properties of the IAV envelope by using a monovalent LAIV. Under the conditions of the experiments, the complex surface structure of the virus was not resolved in detail but an overview on the size and morphology was obtained. Preserved single IAV envelopes were identified in air, suggesting that the sample can be used for further analysis under different hydration conditions. While the interpretation of the data is mainly limited by the unknown composition of the sample, the results indicate that the virus might be stable upon dehydration. In this context, we have characterized physisorbed IAVs on chemically different flat substrates at the nanoscale. This provides a novel approach of LAIVs as model systems of the IAV envelope to study the morphology changes taking place under various humidity conditions.

Chapter 6

Conclusions and outlook

In this research we could unveil hydration mechanisms driven by humidity variations on models of Influenza A virus (IAV) envelope, with a purely biophysical interpretation.

The basic requirement is the combination of specialized techniques, in some cases additionally adapted to the experiments. These techniques, described in **Chapter 2**, certainly allowed to study the interaction of water with the model systems at the micro- and nanoscale. Contact angle measurements provided information on the hydrophilic nature of the substrates at the microscale. By Dynamic Light Scattering (DLS) and Zeta Potential (ZP) measurements we could estimate the size and charge of nanoparticles in aqueous solution. Vibrational Sum Frequency Generation Spectroscopy (VSFG) and Fourier Transform Infrared Spectroscopy (FT-IR) were used as complementary techniques to achieve information on the chemical composition of the model systems, and to characterize adsorbed/absorbed water on the sample and at the interface after dehydration. Electron Microscopy enabled to characterize the studied samples in terms of morphology, size, and agglomeration tendency in hydrophilic and hydrophobic conditions after dehydration. Confocal Fluorescence Microscopy, Raster Image Correlation Spectroscopy (RICS) and Line-Scan Fluorescence Correlation Spectroscopy (LSFCS) were successfully used to study the structure and dynamics of biological membranes under dehydration-rehydration cycles at the microscale. Atomic Force Microscopy (AFM) in controlled atmospheres – the *vedette* of this investigation – provided new insights on sample morphology and hydration layers at the nanoscale, from fully hydrated states (solution) to dehydrated conditions.

In **Chapter 3**, the diverse properties of dimannoside-coated gold nanoparticles (*Dimanno*-AuNPs) and polyethylene glycol gold nanoparticles (PEG-AuNPs) under hydrophilic and hydrophobic conditions at different hydration states -from solution to dehydration- were demonstrated. The *Dimanno*-AuNPs can be interpreted as model systems of the IAV surface glycoprotein hemagglutinin (HA), based on size and surface chemistry. The main findings are the presence of a thin water layer on the particles, and structuring properties at the interface after dehydration; both are possibly due to strong

hydrogen bonding interactions. Of note, performing FT-IR after sample dehydration in deuterated water will finally complement the results obtained at the air interface, thus providing a more complete scenario of adsorbed/absorbed water after sample dehydration. The adsorption of an ultrathin water layer, from dehydrated conditions to high humidity, is additionally demonstrated. In analogy, the dimannoside residues found on the surface glycoproteins HA and neuraminidase (NA) should play a primary role in water retention after dehydration. This is one of very few interpretations of the "survival" of Influenza viruses in dry conditions, that is actually based on experimental data rather than assumptions or general considerations. Obviously, this is yet restricted to Influenza, and cannot be transferred to other viruses.

The ability to induce water structuring may be important for retaining a hydrated layer and could offer advantages for virus stability and survival. In this direction, our model has only been studied for dimannose residues and has not been compared with "lower" (mannose) or "higher" (oligomannose) glycans. The latter would make sense in view of the high-mannose branched glycans found on IAVs. Furthermore, we have only assessed the behavior of the particles in spherical structures, while HA has a stem domain (rod shape) with a globular domain (spherical shape). To obtain a complete analysis of the role of the surface glycans and of shape, future studies could address these points. A first step would be studying rod-shaped particles to better mimic the HA and change the glycan surface composition to complex and branched structures that are found on the surface of the glycoproteins. The effects on structuring properties and water retention of these residues might also be addressed by changing the glycan coverage on the gold particles.

In **Chapter 4**, we introduced a novel approach to investigate the IAV H1N1 envelope under different hydration level, by the development of a supported lipid bilayer that contains HA at very high density – a "flattened" and very simplified model of the viral envelope. The results indicate that HA can act as a membrane protectant upon dehydration. While membrane dehydration experiments are known, although rarely reported, HA has to our knowledge never been considered as a factor, despite its high coverage on the viral envelope. The experiments provide new insights regarding the molecular mechanisms, which determine virus stability and survival outside living cells; these are primary features to design successful campaigns for controlling virus transmission.

The model is mainly limited by the specific membrane composition, hence, future studies could address the lack of NA and matrix 2 ion channel (M2), the role of specific lipids (i.e. cholesterol, phosphatidylethanolamine and phosphatidylserine), as well as the incorporation of glycolipids on the membrane. Actually, the composition of the IAV envelope contains Forssman glycolipids – the most abundant sphingolipids in the virion – which alter a number of biophysical properties of the IAV envelope, e.g. reduced mobility of the bilayer lipid and protein species. In analogy to the dehydration resistance provided by trehalose glycolipids in mycobacteria membranes, the Forssman glycolipids might

confer stability of the IAV envelope upon dehydration. Yet, the protective effects on the surface envelope have never been studied in detail. Regarding HA, future research might point towards the use of the wild type protein, with incorporated cytoplasmic and transmembrane domains. Indeed, this was already tested in this investigation; we purified HA from Influenza X-31 virus and performed detergent-mediated incorporation into the supported lipid bilayers. However, the purification yield was notably low, thus HA was only incorporated at low density packing. Future investigations could address this issue, as well as design new strategies to increase the surface density of HA via Nickel (Ni^{2+})/hexahistidine-Tag interaction. Control experiments may also include removal of glycosylation sites in HA – by enzyme digestion – to understand the specific role of the surface glycans. From this, a more complete analysis of the interactions between the viral envelope and water molecules should be obtained.

Finally, in **Chapter 5**, a monovalent live attenuated Influenza vaccine (LAIV) was used as a model system of the complete IAV envelope. This research approach is an alternative method to investigate its biophysical properties. Under the conditions of the experiments, the complex surface structure of the virus was not resolved in detail, but an overview on the size and morphology was obtained in dehydrated conditions – the exceptional stability upon partial dehydration is established, and **Chapters 3** and **4** provide a detailed model picture. Here, we have characterized the virus structure adsorbed on a flat surface which can be used as an analogous model of the IAV during transmission in aerosols. The use of a LAIV with undetermined exact composition limits the interpretation to detection of virus particles and their arrangement and approximate shape on the surface.

Future studies should be based on better defined and purified LAIVs, and use application surfaces, e.g. surfaces that mimic the respiratory tract. The presence of salts or saccharides, as in mucus, might enhance the "survival", but must first be avoided to obtain meaningful results at the nanoscale. Future research should include dehydration (or even dehydration-rehydration cycles) during AFM measurements; this would already very closely follow a realistic scenario.

Acknowledgements

I would like to express my deep gratitude to those involved in helping me for the completion of my PhD thesis, through their valuable discussions, guidance and support.

I want to thank the institutions where this PhD thesis was performed: CIC-nanoGUNE (BRTA) (Self-Assembly Group) and the Materials Physics Center (Polymers and Soft Matter Group), as well as the places where the international research visits were developed, namely the University of Potsdam (Cell Membrane Biophysics Group – Physikalische Biochemie) and the Fritz Haber Institute of the Max Planck Society (Nonlinear Spectro-electrochemistry Group). I want to acknowledge the European Molecular Biology Organization (EMBO, Short-Term Fellowship 2019, Grant number 8397) and the German Academic Exchange Service (DAAD, Research Grants –Short-Term Grants 2020, Grant number 57507442) for giving me support on these international visits.

I would like to thank my PhD supervisors, Dr. A.M. Bittner and Dr. S. Cerveny Murcia for their mentoring and advices through all this entire process and for the extraordinary scientific independence they allowed me to exercise.

I would like to express my gratitude to C. Wege and Y. Tong for performing the external assessment and offering remarkable suggestions in this PhD thesis progress. I would like to acknowledge K. Blank and R. Dünnebacke for providing me with an Atomic Force Microscopy instrument during my research visit at Potsdam. I want to give special thanks to C. Tollan and E. Nikulina for their valuable time and great collaboration in Electron Microscopy imaging. Also, to I. Garcia for donating the gold nanoparticles used in this investigation. To M. Gallego and M. Moller for mentoring me in negative staining methods. I am also thankful to U. Montejo Insausti for helping my research in Atomic Force Microscopy imaging. To A. Petrich and Z. Aguirre Sourrouille for valuable discussions as well as J.H. Melillo for sharing his knowledge in Electron Microscopy and most important, in the PhD program.

I want to personally thank A. Eleta Lopez and S. Chiantia –my *off shore* or indirect scientific advisors- for mentoring me through all this process. Their continuous encourage, timeless help and research up to the highest level truly inspired my career path in science.

I want to thank the former and the present members of the Self-Assembly Group (M. Okuda, M. Rekondo Salsamendi and E. Georgilis) as well as the nano-Coffee colleagues (M.C. Villoslada Hidalgo, S. Azpeitia Coscaron, M. Menniti and G. De Salvo). Specially, M. Cascajo-Castresana, G. Prêtre and I. Moreno for simply, being always there.

I am grateful to A. Varor, J. Nesprias, J. de Combi, N. Benítez and particularly to J. Gómez Saá and A. Falcoff for their outstanding support, principally in my writing process.

Finally, I am indebted to my close friends and of course, to my family, for their permanent encouragement and for the many visits to every world destination that my studies demanded me to be.

List of Publications

The results presented in this work have been communicated in the following article:

M.A. Iriarte-Alonso, A.M. Bittner, S. Chiantia, Influenza A virus hemagglutinin prevents extensive membrane damage upon dehydration, Biochim. Biophys. Acta - Biomembr. (2022). Accepted.

Publications indirectly related to this thesis include:

M. Cascajo-Castresana, R.O. David, **M.A. Iriarte-Alonso**, A.M. Bittner, C. Marcolli, Protein aggregates nucleate ice: The example of apoferritin, Atmos. Chem. Phys. 20 (2020) 3291–3315. https://doi.org/10.5194/acp-20-3291-2020.

References

[1] A. Lehninger, Principles of Biochemistry, 1st Ed., Worth Publishers Inc., U.S.A. (1998).

[2] M. Moriyama, W.J. Hugentobler, Seasonality of Respiratory Viral Infections, Annu. Rev. Virol. 8 (2020) 83–101. https://doi.org/ 10.1146/annurev-virology-012420-022445.

[3] B. Killingley, J. Nguyen-Van-Tam, Routes of influenza transmission, Influenza Other Respi. Viruses. 7 (2013) 42–51. https://doi.org/10.1111/irv.12080.

[4] V.N. Petrova, C.A. Russell, The evolution of seasonal influenza viruses, Nat. Rev. Microbiol. 16 (2018) 47–60. https://doi.org/10.1038/nrmicro.2017.118.

[5] E.P. Vejerano, L.C. Marr, Physico-chemical characteristics of evaporating respiratory fluid droplets, J. R. Soc. Interface. 15 (2018) 1–10. https://doi.org/10.1098/rsif.2017.0939.

[6] R.S. Papineni, F.S. Rosenthal, The size distribution of droplets in the exhaled breath of healthy human subjects, J. Aerosol Med. Depos. Clear. Eff. Lung. 10 (1997) 105–116. https://doi.org/10.1089/jam.1997.10.105.

[7] W. Kauzmann, Some Factors in the Interpretation of Protein Denaturation, Adv. Protein Chem. 14 (1959) 1–63. https://doi.org/10.1016/S0065-3233(08)60608-7.

[8] R.L. Baldwin, Dynamic hydration shell restores Kauzmann's 1959 explanation of how the hydrophobic factor drives protein folding, Proc. Natl. Acad. Sci. U.S.A. 111 (2014) 13052–13056. https://doi.org/10.1073/pnas.1414556111.

[9] P. Ball, Water as an active constituent in cell biology, Chem. Rev. 108 (2008) 74–108. https://doi.org/10.1021/cr068037a.

[10] B. Bagchi, Water dynamics in the hydration layer around proteins and micelles, Chem. Rev. 105 (2005) 3197–3219. https://doi.org/10.1021/cr020661+.

[11] D. Laage, T. Elsaesser, J.T. Hynes, Water Dynamics in the Hydration Shells of Biomolecules, Chem. Rev. 117 (2017) 10694–10725.

https://doi.org/10.1021/acs.chemrev.6b00765.

[12] J. Funahashi, Y. Yamagata, Positive contribution of hydration structure on the surface of human lysozyme to the conformational stability, J. Biol. Chem. 277 (2002) 21792–21800. https://doi.org/10.1074/jbc.M110728200.

[13] K. Kobayashi, N. Oyabu, K. Kimura, S. Ido, K. Suzuki, T. Imai, K. Tagami, M. Tsukada, H. Yamada, Visualization of hydration layers on muscovite mica in aqueous solution by frequency-modulation atomic force microscopy, J. Chem. Phys. 138 (2013). https://doi.org/10.1063/1.4803742.

[14] T. Fukuma, Water distribution at solid/liquid interfaces visualized by frequency modulation atomic force microscopy, Sci. Technol. Adv. Mater. 11 (2010) 033003. https://doi.org/10.1088/1468-6996/11/3/033003.

[15] T. Zuk, F. Rakowski, J.P. Radomski, A model of influenza virus spread as a function of temperature and humidity, Comput. Biol. Chem. 33 (2009) 176–180. https://doi.org/10.1016/j.compbiolchem.2008.12.001.

[16] J. Gralton, E. Tovey, M.L. McLaws, W.D. Rawlinson, The role of particle size in aerosolised pathogen transmission: A review, J. Infect. 62 (2011) 1–13. https://doi.org/10.1016/j.jinf.2010.11.010.

[17] A. Lwoff, The concept of virus., J. Gen. Microbiol. 17 (1957) 239–253. https://doi.org/10.1099/00221287-17-2-239.

[18] E.V. Koonin, V. V. Dolja, M. Krupovic, J.H. Kuhn, Viruses defined by the position of the virosphere within the replicator space. Microbiol. Mol. Biol. Rev. (2021) 85:e00193-20. https:// doi.org/10.1128/MMBR.00193-20.

[19] M.G. Mateu, Structure and Physics of Viruses, 1st Ed., Springer Publishing Co., U.S.A. (2013). https://doi.org/10.1007/978-94-007-6552-8.

[20] L. Herrero-Uribe, Viruses, definitions and reality, Rev. Biol. Trop. 59 (2011) 993–998. https://doi.org/10.15517/rbt.v0i0.3372.

[21] S. Li, Doctoral thesis dissertation: Atomic force microscopy study on the mechanics of influenza viruses and liposomes, Georg-August-Universität Göttingen. (2012).

[22] A.M.Q. King, M.J. Adams, E.B. Carstens, E.J. Lefkowitz, Virus Taxonomy:

Classification and Nomenclature of Viruses, 9th Report, Elsevier Science Inc., U.S.A. (2012).

[23] A.P. Schmitt, R.A. Lamb, Influenza Virus Assembly and Budding at the Viral Budozone, Adv. Virus Res. 64 (2005) 383–416. https://doi.org/10.1016/S0065-3527(05)64012-2.

[24] N.H.L. Leung, Transmissibility and transmission of respiratory viruses, Nat. Rev. Microbiol. 19 (2021) 528–545. https://doi.org/10.1038/s41579-021-00535-6.

[25] World Health Organization, Influenza (Seasonal) (2022). [Online; accessed 20-February-2022]. https://www.who.int/news-room/fact-sheets/detail/influenza-(seasonal).

[26] A. Harris, G. Cardone, D.C. Winkler, J.B. Heymann, M. Brecher, J.M. White, A.C. Steven, Influenza virus pleiomorphy characterized by cryoelectron tomography, Proc. Natl. Acad. Sci. U.S.A. 103 (2006) 19123–19127. https://doi.org/10.1073/pnas.0607614103.

[27] W. Van Breedam, S. Pöhlmann, H.W. Favoreel, R.J. de Groot, H.J. Nauwynck, Bitter-sweet symphony: Glycan-lectin interactions in virus biology, FEMS Microbiol. Rev. 38 (2014) 598–632. https://doi.org/10.1111/1574-6976.12052.

[28] I.A. York, J. Stevens, I.V. Alymova, Influenza virus N-linked glycosylation and innate immunity, Biosci. Rep. 39 (2019) 1–15. https://doi.org/10.1042/BSR20171505.

[29] P. Kim, Y.H. Jang, S. Bin Kwon, C.M. Lee, G. Han, B.L. Seong, Glycosylation of hemagglutinin and neuraminidase of influenza a virus as signature for ecological spillover and adaptation among influenza reservoirs, Viruses. 10 (2018) 1–18. https://doi.org/10.3390/v10040183.

[30] M.D. Tate, E.R. Job, Y.M. Deng, V. Gunalan, S. Maurer-Stroh, P.C. Reading, Playing hide and seek: How glycosylation of the influenza virus hemagglutinin can modulate the immune response to infection, Viruses. 6 (2014) 1294–1316. https://doi.org/10.3390/v6031294.

[31] N.M. Bouvier, P. Palese, The biology of influenza viruses, Vaccine. 26 (2008). https://doi.org/10.1016/j.vaccine.2008.07.039.

[32] A. Petrich, V. Dunsing, S. Bobone, S. Chiantia, Influenza A M2 recruits M1 to the

plasma membrane: A fluorescence fluctuation microscopy study, Biophys. J. 120 (2021) 5478–5490. https://doi.org/10.1016/j.bpj.2021.11.023.

[33] C.T. Höfer, S. Di Lella, I. Dahmani, N. Jungnick, N. Bordag, S. Bobone, Q. Huang, S. Keller, A. Herrmann, S. Chiantia, Structural determinants of the interaction between influenza A virus matrix protein M1 and lipid membranes, Biochim. Biophys. Acta - Biomembr. 1861 (2019) 1123–1134. https://doi.org/10.1016/j.bbamem.2019.03.013.

[34] O. Weber, The role of viruses in the etiology and pathogenesis of common cold, Common Cold. (2009) 107–147. https://doi.org/10.1007/978-3-7643-9912-2_5.

[35] S. Wasilewski, L.J. Calder, T. Grant, P.B. Rosenthal, Distribution of surface glycoproteins on influenza A virus determined by electron cryotomography, Vaccine. 30 (2012) 7368–7373. https://doi.org/10.1016/j.vaccine.2012.09.082.

[36] G.J. Harper, Airborne micro-organisms: Survival tests with four viruses, J. Hyg. (Lond). 59 (1961) 479–486. https://doi.org/10.1017/S0022172400039176.

[37] A. Ianevski, E. Zusinaite, N. Shtaida, H. Kallio-Kokko, M. Valkonen, A. Kantele, K. Telling, I. Lutsar, P. Letjuka, N. Metelitsa, V. Oksenych, U. Dumpis, A. Vitkauskiene, K. Stašaitis, C. Öhrmalm, K. Bondeson, A. Bergqvist, R.J. Cox, T. Tenson, A. Merits, D.E. Kainov, Low temperature and low UV indexes correlated with peaks of influenza virus activity in northern europe during 2010–2018, Viruses. 11 (2019). https://doi.org/10.3390/v11030207.

[38] J.J. McDevitt, S.N. Rudnick, L.J. Radonovich, Aerosol susceptibility of influenza virus to UV-C light, Appl. Environ. Microbiol. 78 (2012) 1666–1669. https://doi.org/10.1128/AEM.06960-11.

[39] I. V. Polozov, L. Bezrukov, K. Gawrisch, J. Zimmerberg, Progressive ordering with decreasing temperature of the phospholipids of influenza virus, Nat. Chem. Biol. 4 (2008) 248–255. https://doi.org/10.1038/nchembio.77.

[40] T. Reddy, D. Shorthouse, D.L. Parton, E. Jefferys, P.W. Fowler, M. Chavent, M. Baaden, M.S.P. Sansom, Nothing to Sneeze At: A Dynamic and Integrative Computational Model of an Influenza A Virion, Structure. 23 (2015) 584–597. https://doi.org/10.1016/j.str.2014.12.019.

[41] W. Yang, L.C. Marr, Dynamics of Airborne influenza A viruses indoors and

dependence on humidity, PLoS One. 6 (2011). https://doi.org/10.1371/journal.pone.0021481.

[42] K.A. Kormuth, K. Lin, A.J. Prussin, E.P. Vejerano, A.J. Tiwari, S.S. Cox, M.M. Myerburg, S.S. Lakdawala, L.C. Marr, Influenza virus infectivity is retained in aerosols and droplets independent of relative humidity, J. Infect. Dis. 218 (2018) 739–747. https://doi.org/10.1093/infdis/jiy221.

[43] K.A. Kormuth, K. Lin, Z. Qian, M.M. Myerburg, L.C. Marr, S.S. Lakdawala, Environmental Persistence of Influenza Viruses Is Dependent upon Virus Type and Host Origin, MSphere. 4 (2019) 1–14. https://doi.org/10.1128/msphere.00552-19.

[44] J. McDevitt, S. Rudnick, M. First, J. Spengler, Role of absolute humidity in the inactivation of influenza viruses on stainless steel surfaces at elevated temperatures, Appl. Environ. Microbiol. 76 (2010) 3943–3947. https://doi.org/10.1128/AEM.02674-09.

[45] J. Shaman, M. Kohn, Absolute humidity modulates influenza survival, transmission, and seasonality, Proc. Natl. Acad. Sci. U.S.A. 106 (2009) 3243–3248. https://doi.org/10.1073/pnas.0806852106.

[46] J. Shaman, V.E. Pitzer, C. Viboud, B.T. Grenfell, M. Lipsitch, Absolute humidity and the seasonal onset of influenza in the continental United States, PLoS Biol. 8 (2010). https://doi.org/10.1371/journal.pbio.1000316.

[47] E.R. Deyle, M.C. Maher, R.D. Hernandez, S. Basu, G. Sugihara, Global environmental drivers of influenza, Proc. Natl. Acad. Sci. U.S.A. 113 (2016) 13081–13086. https://doi.org/10.1073/pnas.1607747113.

[48] L.C. Marr, J.W. Tang, J. Van Mullekom, S.S. Lakdawala, Mechanistic insights into the effect of humidity on airborne influenza virus survival, transmission and incidence, J. R. Soc. Interface. 16 (2019). https://doi.org/10.1098/rsif.2018.0298.

[49] O. Martínez-Ávila, K. Hijazi, M. Marradi, C. Clavel, C. Campion, C. Kelly, S. Penadés, Gold Manno-Glyconanoparticles: Multivalent systems to block HIV-1 gp120 binding to the lectin DC-SIGN, Chem. - A Eur. J. 15 (2009) 9874–9888. https://doi.org/10.1002/chem.200900923.

[50] C. Gröger, K. Lutz, E. Brunner, Biomolecular self-assembly and its relevance in silica biomineralization, Cell Biochem. Biophys. 50 (2008) 23–39.

https://doi.org/10.1007/s12013-007-9003-2.

[51] L. Wang, C. Gong, X. Yuan, G. Wei, Controlling the self-assembly of biomolecules into functional nanomaterials through internal interactions and external stimulations: A review, Nanomaterials. 9 (2019). https://doi.org/10.3390/nano9020285.

[52] A. Checco, H. Schollmeyer, J. Daillant, P. Guenoun, R. Boukherroub, Nanoscale wettability of self-assembled monolayers investigated by noncontact atomic force microscopy, Langmuir. 22 (2006) 116–126. https://doi.org/10.1021/la051419b.

[53] E. Sackmann, Supported membranes: Scientific and practical applications, Science 271 (1996) 43–48. https://doi.org/10.1126/science.271.5245.43.

[54] P.S. Cremer, J.T. Groves, L.A. Kung, S.G. Boxer, Writing and Erasing Barriers to Lateral Mobility into Fluid Phospholipid Bilayers, Langmuir 15 (1999) 3893–3896.

[55] Y.F. Dufrêne, T. Boland, J.W. Schneider, W.R. Barger, G.U. Lee, Characterization of the physical properties of model biomembranes at the nanometer scale with the atomic force microscope, Faraday Discuss. 111 (1999) 79–94. https://doi.org/10.1039/a807637e.

[56] K. Mulligan, Z.J. Jakubek, L.J. Johnston, Supported lipid bilayers on biocompatible polysaccharide multilayers, Langmuir. 27 (2011) 14352–14359. https://doi.org/10.1021/la203207p.

[57] F. Khan, M. He, M.J. Taussig, Double-hexahistidine tag with high-affinity binding for protein immobilization, purification, and detection on Ni-nitrilotriacetic acid surfaces, Anal. Chem. 78 (2006) 3072–3079. https://doi.org/10.1021/ac060184l.

[58] M.E. Kimple, A.L. Brill, R.L. Pasker, Overview of affinity tags for protein purification, Curr. Protoc. Protein Sci. (2013) 608–616. https://doi.org/10.1002/0471140864.ps0909s73.

[59] B. Holzer, S.B. Morgan, V. Martini, R. Sharma, B. Clark, C. Chiu, F.J. Salguero, E. Tchilian, Immunogenicity and Protective Efficacy of Seasonal Human Live Attenuated Cold-Adapted Influenza Virus Vaccine in Pigs, Front. Immunol. 10 (2019) 1–13. https://doi.org/10.3389/fimmu.2019.02625.

[60] K.G.I. Mohn, I. Smith, H. Sjursen, R.J. Cox, Immune responses after live attenuated

influenza vaccination, Hum. Vaccines Immunother. 14 (2018) 571–578. https://doi.org/10.1080/21645515.2017.1377376.

[61] G. Kumar, K.N. Prabhu, Review of non-reactive and reactive wetting of liquids on surfaces, Adv. Colloid Interface Sci. 133 (2007) 61–89. https://doi.org/10.1016/j.cis.2007.04.009.

[62] C.P. Stallard, K.A. McDonnell, O.D. Onayemi, J.P. O'Gara, D.P. Dowling, Evaluation of protein adsorption on atmospheric plasma deposited coatings exhibiting superhydrophilic to superhydrophobic properties, Biointerphases. 7 (2012) 1–12. https://doi.org/10.1007/s13758-012-0031-0.

[63] J. Den Engelsman, P. Garidel, R. Smulders, H. Koll, B. Smith, S. Bassarab, A. Seidl, O. Hainzl, W. Jiskoot, Strategies for the assessment of protein aggregates in pharmaceutical biotech product development, Pharm. Res. 28 (2011) 920–933. https://doi.org/10.1007/s11095-010-0297-1.

[64] J. Stetefeld, S.A. McKenna, T.R. Patel, Dynamic light scattering: a practical guide and applications in biomedical sciences, Biophys. Rev. 8 (2016) 409–427. https://doi.org/10.1007/s12551-016-0218-6.

[65] R. Xu, Particle Characterization: Light Scattering Methods, 1st Ed., Springer Publishing Co., U.S.A. (2003). https://doi.org/10.1016/s1672-2515(07)60008-6.

[66] S. Bhattacharjee, DLS and zeta potential - What they are and what they are not?, J. Control. Release. 235 (2016) 337–351. https://doi.org/10.1016/j.jconrel.2016.06.017.

[67] Malvern Instruments Ltd., Zeta potential: An Introduction in 30 minutes, Zetasizer Nano Serles Tech. Note. MRK654-01. 2 (2011) 1–6. [Online; accessed 20-February-2022]. https://www.research.colostate.edu/wp-content/uploads/2018/11/ZetaPotential-Introduction-in-30min-Malvern.pdf.

[68] Bio-Rad Laboratories Inc., A Guide to Polyacrylamide Gel Electrophoresis and Detection, Bulletin 6040. [Online; accessed 20-February-2022]. https://www.bio-rad.com/webroot/web/pdf/lsr/literature/Bulletin_6040.pdf.

[69] The Native Antigen Company, Certificate of Analysis Influenza A [A/Puerto Rico/8/1934 (H1N1)] Hemagglutinin (HA), His-tag. (2019). [Online; accessed 14-January-2022].

https://thenativeantigencompany.com/wp-content/uploads/2018/10/CofA-FLU-H1N1-HA-100-Batch-16070611.pdf.

[70] X.D. Zhu, H. Suhr, Y.R. Shen, Surface vibrational spectroscopy by infrared-visible sum frequency generation, Phys. Rev. B. 35 (1987) 3047–3050. https://doi.org/10.1103/PhysRevB.35.3047.

[71] V.P. Gupta, Molecular and Laser Spectroscopy -Advances and Applications, 1st Ed., Elsevier Science Inc., U.S.A. (2017).

[72] R.F. Egerton, Physical principles of electron microscopy, Mater. Today. 8 (2005) 49. https://doi.org/10.1016/s1369-7021(05)71290-6.

[73] K. Akhtar, S.A. Khan, S.B. Khan, A.M. Asiri, Handbook of Materials Characterization, ed., S.K. Sharma, Chapter 4: Scanning Electron Microscopy: Principle and Applications in Nanomaterials Characterization, 1st Ed., Springer Publishing Co., U.S.A. (2018) 113-145. https://doi.org/10.1007/978-3-319-92955-2.

[74] P.J. Goodhew, J. Humphreys, R. Beanland, Electron Microscopy and Analysis, 3rd Ed., CRC Press (2000). https://doi.org/10.1201/9781482289343.

[75] Carl Zeiss Microscopy GmbH, Principles of Fluorescence and Fluorescence Microscopy, Technology Note (2019). [Online; accessed 20-February-2022]. https://pages.zeiss.com/rs/896-XMS-794/images/ZEISS-Microscopy_Technology-Note_Principles-of-Fluorescence.pdf.

[76] D. Coling, B. Kachar, Principles and Application of Fluorescence Microscopy, Curr. Protoc. Mol. Biol. 44 (1998) 1–11. https://doi.org/10.1002/0471142727.mb1410s44.

[77] E.L. Elson, Fluorescence correlation spectroscopy: Past, present, future, Biophys. J. 101 (2011) 2855–2870. https://doi.org/10.1016/j.bpj.2011.11.012.

[78] E. Gielen, N. Smisdom, B. De Clercq, E. Gratton, M. Digman, J. Rigo, J. Hofkens, Y. Engelborghs, M. Ameloot, Measuring Diffusion of Lipid-like Probes in Artificial and Natural Membranes by Raster Image Correlation Spectroscopy (RICS): Use of a Commercial Laser-Scanning Microscope with Analog Detection, Langmuir. 25 (2009) 5209–5218. https://doi.org/10.1021/la8040538.

[79] I. Visco, Doctoral thesis dissertation: Breaking symmetry: reconstitution of unmixing and polarization events in model membranes, Ludwig-Maximilians-

Universität München (2015).

[80] J. Ries, S. Chiantia, P. Schwille, Accurate determination of membrane dynamics with line-scan FCS, Biophys. J. 96 (2009) 1999–2008. https://doi.org/10.1016/j.bpj.2008.12.3888.

[81] M.A. Digman, C.M. Brown, P. Sengupta, P.W. Wiseman, A.R. Horwitz, E. Gratton, Measuring fast dynamics in solutions and cells with a laser scanning microscope, Biophys. J. 89 (2005) 1317–1327. https://doi.org/10.1529/biophysj.105.062836.

[82] M. Longfils, N. Smisdom, M. Ameloot, M. Rudemo, V. Lemmens, G.S. Fernández, M. Röding, N. Lorén, J. Hendrix, A. Särkkä, Raster Image Correlation Spectroscopy Performance Evaluation, Biophys. J. 117 (2019) 1900–1914. https://doi.org/10.1016/j.bpj.2019.09.045.

[83] Agilent Technologies, Inc., Agilent Technologies 5500 Scanning Probe Microscope User's Guide, Manual Part Number N9410-90001 (2008). [Online; accessed 20-February-2022]. https://afmhelp.com/docs/manuals/agilent_5500_user_manual_revB.pdf.

[84] A. Eleta-Lopez, A. Calò, Key factors of scanning a plant virus with AFM in air and aqueous solution, Microsc. Res. Tech. 80 (2017) 18–29. https://doi.org/10.1002/jemt.22741.

[85] E. Pereira da Silva, M. Chaves, G. Junior da Silva, L. Baldo de Arruda, P.N. Lisboa-Filho, S.F. Durrant, J.R.R. Bortoleto, Al-Doping Effect on the Surface Morphology of ZnO Films Grown by Reactive RF Magnetron Sputtering, Mater. Sci. Appl. 04 (2013) 761–767. https://doi.org/10.4236/msa.2013.412096.

[86] V. V. Tsukruk, S. Singamaneni, Scanning Probe Microscopy of Soft Matter: Fundamentals and Practises, 1st Ed., Wiley-VCH Verlag GmbH & Co. KGaA. (2011). https://doi.org/10.1002/9783527639953.

[87] M. Luna, J. Colchero, A. Gil, J. Gómez-Herrero, A.M. Baró, Application of non-contact scanning force microscopy to the study of water adsorption on graphite, gold and mica, Appl. Surf. Sci. 157 (2000) 393–397. https://doi.org/10.1016/S0169-4332(99)00556-5.

[88] A. Calò, A. Eleta-Lopez, T. Ondarçuhu, A. Verdaguer, A.M. Bittner, Nanoscale wetting of single viruses, Molecules. 26 (2021) 1–11.

https://doi.org/10.3390/molecules26175184.

[89] S. Santos, A. Verdaguer, T. Souier, N.H. Thomson, M. Chiesa, Measuring the true height of water films on surfaces, Nanotechnology. 22 (2011). https://doi.org/10.1088/0957-4484/22/46/465705.

[90] S. Ghosal, A. Verdaguer, J.C. Hemminger, M. Salmeron, In situ study of water-induced segregation of bromide in bromide-doped sodium chloride by scanning polarization force microscopy, J. Phys. Chem. A. 109 (2005) 4744–4749. https://doi.org/10.1021/jp046250+.

[91] S. Benaglia, C.A. Amo, R. Garcia, Fast, quantitative and high resolution mapping of viscoelastic properties with bimodal AFM, Nanoscale. 11 (2019) 15289–15297. https://doi.org/10.1039/c9nr04396a.

[92] L. Zitzler, S. Herminghaus, F. Mugele, Capillary forces in tapping mode atomic force microscopy, Phys. Rev. B - Condens. Matter Mater. Phys. 66 (2002) 1–8. https://doi.org/10.1103/PhysRevB.66.155436.

[93] R. García, A. San Paulo, Amplitude curves and operating regimes in dynamic atomic force microscopy, Ultramicroscopy. 82 (2000) 79–83. https://doi.org/10.1016/S0304-3991(99)00132-1.

[94] N. Climent, I. García, M. Marradi, F. Chiodo, L. Miralles, M.J. Maleno, J.M. Gatell, F. García, S. Penadés, M. Plana, Loading dendritic cells with gold nanoparticles (GNPs) bearing HIV-peptides and mannosides enhance HIV-specific T cell responses, Nanomedicine Nanotechnology, Biol. Med. 14 (2018) 339–351. https://doi.org/10.1016/j.nano.2017.11.009.

[95] G. Sonavane, K. Tomoda, K. Makino, Biodistribution of colloidal gold nanoparticles after intravenous administration: Effect of particle size, Colloids Surfaces B Biointerfaces. 66 (2008) 274–280. https://doi.org/10.1016/j.colsurfb.2008.07.004.

[96] K.D. McReynolds, M.J. Hadd, J. Gervay-Hague, Synthesis of biotinylated glycoconjugates and their use in a novel ELISA for direct comparison of HIV-1 gp120 recognition of GalCer and related carbohydrate analogues, Bioconjug. Chem. 10 (1999) 1021–1031. https://doi.org/10.1021/bc990050x.

[97] C.N. Scanlan, J. Offer, N. Zitzmann, R.A. Dwek, Exploiting the defensive sugars of HIV-1 for drug and vaccine design, Nature. 446 (2007) 1038–1045.

https://doi.org/10.1038/nature05818.

[98] S. Ng, N.E. Basta, B.J. Cowling, Association between temperature, Humidity and ebolavirus disease outbreaks in Africa, 1976 to 2014, Eurosurveillance. 19 (2014) 1–11. https://doi.org/10.2807/1560-7917.es2014.19.35.20892.

[99] W. Weissenhorn, A. Dessen, L.J. Calder, S.C. Harrison, J.J. Skehel, D.C. Wiley, Structural basis for membrane fusion by enveloped viruses, Mol. Membr. Biol. 16 (1999) 3–9. https://doi.org/10.1080/096876899294706.

[100] A.E. Lopez, S. Moreno-Flores, D. Pum, U.B. Sleytr, J.L. Toca-Herrera, Surface dependence of protein nanocrystal formation, Small. 6 (2010) 396–403. https://doi.org/10.1002/smll.200901169.

[101] S. Abramoff, M.D. Magalhaes, P.J. Ram, Image Processing with ImageJ, Biophotonics Int. 11 (2004) 36–42.

[102] I. Horcas, R. Fernández, J.M. Gómez-Rodríguez, J. Colchero, J. Gómez-Herrero, A.M. Baro, WSXM: A software for scanning probe microscopy and a tool for nanotechnology, Rev. Sci. Instrum. 78 (2007). https://doi.org/10.1063/1.2432410.

[103] K. Shameli, M. Bin Ahmad, S.D. Jazayeri, S. Sedaghat, P. Shabanzadeh, H. Jahangirian, M. Mahdavi, Y. Abdollahi, Synthesis and characterization of polyethylene glycol mediated silver nanoparticles by the green method, Int. J. Mol. Sci. 13 (2012) 6639–6650. https://doi.org/10.3390/ijms13066639.

[104] L.F. Leopold, I.S. Tódor, Z. Diaconeasa, D. Rugină, A. Ştefancu, N. Leopold, C. Coman, Assessment of PEG and BSA-PEG gold nanoparticles cellular interaction, Colloids Surfaces A Physicochem. Eng. Asp. 532 (2017) 70–76. https://doi.org/10.1016/j.colsurfa.2017.06.061.

[105] Chemistry LibreTextsTM, Spectroscopy of Carboxylic Acids (2020). [Online; accessed 9-December-2021]. https://chem.libretexts.org/@go/page/45921.

[106] National Institute of Advanced Industrial Science and Technology (2021). [Online; accessed 9-December-2021]. https://sdbs.db.aist.go.jp.

[107] H.A. Wells, R.H. Atalla, An investigation of the vibrational spectra of glucose, galactose and mannose, J. Mol. Struct. 224 (1990) 385–424. https://doi.org/10.1016/0022-2860(90)87031-R.

[108] D. Lin-Vien, N.B. Colthup, W.G. Fateley, J.G. Grasselli, The Handbook of Infrared and Raman Characteristic Frequencies of Organic Molecules, 1st Ed., Elsevier Science Inc., U.S.A. (1991).

[109] D. Horak, M. Babic, P. Jendelova, V. Herynek, M. Trchova, Z. Pientka, E. Pollert, M. Hajek, E. Sykova, D-Mannose-Modified Iron Oxide Nanoparticles for Stem Cell Labeling, Bioconjugate Chem. 18 (2007) 635−644.

[110] E. Wiercigroch, E. Szafraniec, K. Czamara, M.Z. Pacia, K. Majzner, K. Kochan, A. Kaczor, M. Baranska, K. Malek, Raman and infrared spectroscopy of carbohydrates: A review, Spectrochim. Acta - Part A Mol. Biomol. Spectrosc. 185 (2017) 317–335. https://doi.org/10.1016/j.saa.2017.05.045.

[111] X. Wang, O. Ramström, M. Yan, A photochemically initiated chemistry for coupling underivatized carbohydrates to gold nanoparticles, J. Mater. Chem. 19 (2009) 8944–8949. https://doi.org/10.1039/b917900c.

[112] R.N. Ward, P.B. Davies, C.D. Bain, Orientation of surfactants adsorbed on a hydrophobic surface, J. Phys. Chem. 97 (1993) 7141–7143. https://doi.org/10.1021/j100130a005.

[113] M.U.A. Ahlqvist, L.S. Taylor, Water diffusion in hydrated crystalline and amorphous sugars monitored using H/D exchange, J. Pharm. Sci. 91 (2002) 690–698. https://doi.org/10.1002/jps.10068.

[114] M. Cascajo-Castresana, R.O. David, M.A. Iriarte-Alonso, A.M. Bittner, C. Marcolli, Protein aggregates nucleate ice: The example of apoferritin, Atmos. Chem. Phys. 20 (2020) 3291–3315. https://doi.org/10.5194/acp-20-3291-2020.

[115] J.H. Melillo, J.P. Gabriel, F. Pabst, T. Blochowicz, S. Cerveny, Dynamics of aqueous peptide solutions in folded and disordered states examined by dynamic light scattering and dielectric spectroscopy, Phys. Chem. Chem. Phys. 23 (2021) 15020–15029. https://doi.org/10.1039/d1cp01893k.

[116] nanoComposix, Citrate Surface (2021). [Online; accessed 15-December-2021]. https://nanocomposix.com/pages/citrate-surface.

[117] J.R. Harris, Electron Microscopy Methods and Protocols, ed., M. A. Nasser Hajibagheri, Chapter 2: Negative Staining of Thinly Spread Biological Particulates, 1st Ed., Springer Publishing Co., U.S.A. (1999).

https://doi.org/https://doi.org/10.1385/1-59259-201-5:13.

[118] P. Del Pino, F. Yang, B. Pelaz, Q. Zhang, K. Kantner, R. Hartmann, N. Martinez De Baroja, M. Gallego, M. Möller, B.B. Manshian, S.J. Soenen, R. Riedel, N. Hampp, W.J. Parak, Basic Physicochemical Properties of Polyethylene Glycol Coated Gold Nanoparticles that Determine Their Interaction with Cells, Angew. Chemie - Int. Ed. 55 (2016). Supp. Info: https://onlinelibrary.wiley.com/action/downloadSupplement?doi=10.1002%2Fanie.201511733&file=anie201511733-sup-0001-misc_information.pdf.

[119] X. Shen, C-M. Ho, T-S. Wong, Minimal Size of Coffee Ring Structure, J. Phys. Chem. B. 114 (2010) 5269–5274. https://doi.org/doi:10.1021/jp912190v.

[120] C. Kunstmann-Olsen, D. Belić, D.F. Bradley, M.P. Grzelczak, M. Brust, Humidity-Dependent Reversible Transitions in Gold Nanoparticle Superlattices, Chem. Mater. 28 (2016) 2970–2980. https://doi.org/10.1021/acs.chemmater.6b00070.

[121] A.E. López, D. Pum, U.B. Sleytr, J.L. Toca-Herrera, Influence of surface chemistry and protein concentration on the adsorption rate and S-layer crystal formation, Phys. Chem. Chem. Phys. 13 (2011) 11905–11913. https://doi.org/10.1039/c1cp00052g.

[122] K.K. Katti, V. Kattumuri, S. Bhaskaran, K. V. Katti, R. Kannan, Facile and general method for synthesis of sugar-coated gold nanoparticles, Int. J. Green Nanotechnol. Biomed. 1 (2009) 1–8. https://doi.org/10.1080/19430850902983848.

[123] N. Leopold, V. Chiş, N.E. Mircescu, O.T. Marişca, O.M. Buja, L.F. Leopold, C. Socaciu, C. Braicu, A. Irimie, I. Berindan-Neagoe, One step synthesis of SERS active colloidal gold nanoparticles by reduction with polyethylene glycol, Colloids Surfaces A Physicochem. Eng. Asp. 436 (2013) 133–138. https://doi.org/10.1016/j.colsurfa.2013.05.075.

[124] T. Fukuma, R. Garcia, Atomic- and Molecular-Resolution Mapping of Solid-Liquid Interfaces by 3D Atomic Force Microscopy, ACS Nano. 12 (2018) 11785–11797. https://doi.org/10.1021/acsnano.8b07216.

[125] C. Kunstmann-Olsen, D. Belić, M. Brust, Monitoring pattern formation in drying and wetting dispersions of gold nanoparticles by ESEM, Faraday Discuss. 181 (2015) 281–298. https://doi.org/10.1039/c4fd00270a.

[126] A.M. Alkilany, C.J. Murphy, Toxicity and cellular uptake of gold nanoparticles: What we have learned so far?, J. Nanoparticle Res. 12 (2010) 2313–2333. https://doi.org/10.1007/s11051-010-9911-8.

[127] H.K. Abeyratne-Perera, P.L. Chandran, Mannose Surfaces Exhibit Self-Latching, Water Structuring, and Resilience to Chaotropes: Implications for Pathogen Virulence, Langmuir. 33 (2017) 9178–9189. https://doi.org/10.1021/acs.langmuir.7b01006.

[128] K.M. Gustin, J.A. Belser, V. Veguilla, H. Zeng, J.M. Katz, T.M. Tumpey, T.R. Maines, Environmental conditions affect exhalation of H3N2 seasonal and variant influenza viruses and respiratory droplet transmission in ferrets, PLoS One. 10 (2015) 1–19. https://doi.org/10.1371/journal.pone.0125874.

[129] A.C. Lowen, S. Mubareka, J. Steel, P. Palese, Influenza virus transmission is dependent on relative humidity and temperature, PLoS Pathog. 3 (2007) 1470–1476. https://doi.org/10.1371/journal.ppat.0030151.

[130] L.J. Calder, P.B. Rosenthal, Structural Snapshots of Influenza Virus Membrane Fusion by Cryomicroscopy, Nat. Struct. Mol .Biol. 23 (2019) 853–858. https://doi.org/10.1038/nsmb.3271.Structural.

[131] M.D. Vahey, D.A. Fletcher, Influenza a virus surface proteins are organized to help penetrate host mucus, Elife. 8 (2019) 1–24. https://doi.org/10.7554/eLife.43764.

[132] E. Sackmann, Membrane bending energy concept of vesicle- and cell-shapes and shape-transitions, FEBS Lett. 346 (1994) 3–16. https://doi.org/10.1016/0014-5793(94)00484-6.

[133] E.T. Castellana, P.S. Cremer, Solid supported lipid bilayers: From biophysical studies to sensor design, Surf. Sci. Rep. 61 (2006) 429–444. https://doi.org/10.1016/j.surfrep.2006.06.001.

[134] S. Chiantia, J. Ries, N. Kahya, P. Schwille, Combined AFM and two-focus SFCS study of raft-exhibiting model membranes, ChemPhysChem. 7 (2006) 2409–2418. https://doi.org/10.1002/cphc.200600464.

[135] W.C. Lin, C.D. Blanchette, T.V. Ratto, M.L. Longo, Lipid asymmetry in DLPC/DSPC-supported lipid bilayers: A combined AFM and fluorescence microscopy study, Biophys. J. 90 (2006) 228–237.

https://doi.org/10.1529/biophysj.105.067066.

[136] H.G. Franquelim, D. Gaspar, A.S. Veiga, N.C. Santos, M.A.R.B. Castanho, Decoding distinct membrane interactions of HIV-1 fusion inhibitors using a combined atomic force and fluorescence microscopy approach, Biochim. Biophys. Acta - Biomembr. 1828 (2013) 1777–1785. https://doi.org/10.1016/j.bbamem.2013.03.006.

[137] K. Stirnnagel, D. Lüftenegger, A. Stange, A. Swiersy, E. Müllers, J. Reh, N. Stanke, A. Große, S. Chiantia, H. Keller, P. Schwille, H. Hanenberg, H. Zentgraf, D. Lindemann, Analysis of Prototype Foamy Virus particle-host cell interaction with autofluorescent retroviral particles, Retrovirology. 7 (2010) 1–17. https://doi.org/10.1186/1742-4690-7-45.

[138] R. Macháň, M. Hof, Recent developments in fluorescence correlation spectroscopy for diffusion measurements in planar lipid membranes, Int. J. Mol. Sci. 11 (2010) 427–457. https://doi.org/10.3390/ijms11020427.

[139] R.F. Epand, C.M. Yip, L. V. Chernomordik, D.L. LeDuc, Y.K. Shin, R.M. Epand, Self-assembly of influenza hemagglutinin: Studies of ectodomain aggregation by in situ atomic force microscopy, Biochim. Biophys. Acta - Biomembr. 1513 (2001) 167–175. https://doi.org/10.1016/S0005-2736(01)00350-9.

[140] V. Reiter-Scherer, J.L. Cuellar-Camacho, S. Bhatia, R. Haag, A. Herrmann, D. Lauster, J.P. Rabe, Force Spectroscopy Shows Dynamic Binding of Influenza Hemagglutinin and Neuraminidase to Sialic Acid, Biophys. J. 116 (2019) 1037–1048. https://doi.org/10.1016/j.bpj.2019.01.041.

[141] N. Barinov, N. Ivanov, A. Kopylov, D. Klinov, E. Zavyalova, Direct visualization of the oligomeric state of hemagglutinins of influenza virus by high-resolution atomic force microscopy, Biochimie. 146 (2018) 148–155. https://doi.org/10.1016/j.biochi.2017.12.014.

[142] K. Lim, N. Kodera, H. Wang, M.S. Mohamed, M. Hazawa, A. Kobayashi, T. Yoshida, R. Hanayama, S. Yano, T. Ando, R.W. Wong, High-Speed AFM Reveals Molecular Dynamics of Human Influenza A Hemagglutinin and Its Interaction with Exosomes, Nano Lett. 20 (2020) 6320–6328. https://doi.org/10.1021/acs.nanolett.0c01755.

[143] S. Gamage, M. Howard, H. Makita, B. Cross, G. Hastings, M. Luo, Y. Abate, Probing structural changes in single enveloped virus particles using nano-infrared

spectroscopic imaging, PLoS One. 13 (2018) 1–12. https://doi.org/10.1371/journal.pone.0199112.

[144] A.A. Brian, H.M. McConnell, Allogeneic stimulation of cytotoxic T cells by supported planar membranes, Proc. Natl. Acad. Sci. U.S.A. 81 (1984) 6159–6163. https://doi.org/10.1073/pnas.81.19.6159.

[145] F.A. Thomas, I. Visco, Z. Petrášek, F. Heinemann, P. Schwille, Diffusion coefficients and dissociation constants of enhanced green fluorescent protein binding to free standing membranes, Data Br. 5 (2015) 537–541. https://doi.org/10.1016/j.dib.2015.10.002.

[146] C. Üzüm, J. Hellwig, N. Madaboosi, D. Volodkin, R. von Klitzing, Growth behaviour and mechanical properties of PLL/HA multilayer films studied by AFM, Beilstein J. Nanotechnol. 3 (2012) 778–788. https://doi.org/10.3762/bjnano.3.87.

[147] J. Hendrix, T. Dekens, W. Schrimpf, D.C. Lamb, Arbitrary-Region Raster Image Correlation Spectroscopy, Biophys. J. 111 (2016) 1785–1796. https://doi.org/10.1016/j.bpj.2016.09.012.

[148] V. Dunsing, A. Petrich, S. Chiantia, Spectral Detection Enables Multi-Color Fluorescence Fluctuation Spectroscopy Studies in Living Cells, Biophys. J. 120 (2021) 356a. https://doi.org/10.1016/j.bpj.2020.11.2206.

[149] S. Bobone, M. Hilsch, J. Storm, V. Dunsing, A. Herrmann, S. Chiantia, Phosphatidylserine Lateral Organization Influences the Interaction of Influenza Virus Matrix Protein 1 with Lipid Membranes, J. Virol. 91 (2017). https://doi.org/10.1128/jvi.00267-17.

[150] R. Tzoneva, T. Stoyanova, A. Petrich, D. Popova, V. Uzunova, A. Momchilova, S. Chiantia, Effect of erufosine on membrane lipid order in breast cancer cell models, Biomolecules. 10 (2020). https://doi.org/10.3390/biom10050802.

[151] J.A. Nye, J.T. Groves, Kinetic control of histidine-tagged protein surface density on supported lipid bilayers, Langmuir. 24 (2008) 4145–4149. https://doi.org/10.1021/la703788h.

[152] D. Shcherbo, E.A. Souslova, J. Goedhart, T. V. Chepurnykh, A. Gaintzeva, I.I. Shemiakina, T.W.J. Gadella, S. Lukyanov, D.M. Chudakov, Practical and reliable FRET/FLIM pair of fluorescent proteins, BMC Biotechnol. 9 (2009) 1–6.

https://doi.org/10.1186/1472-6750-9-24.

[153] K.S. Sarkisyan, A.S. Goryashchenko, P. V. Lidsky, D.A. Gorbachev, N.G. Bozhanova, A.Y. Gorokhovatsky, A.R. Pereverzeva, A.P. Ryumina, V. V. Zherdeva, A.P. Savitsky, K.M. Solntsev, A.S. Bommarius, G. V. Sharonov, J.R. Lindquist, M. Drobizhev, T.E. Hughes, A. Rebane, K.A. Lukyanov, A.S. Mishin, Green Fluorescent Protein with Anionic Tryptophan-Based Chromophore and Long Fluorescence Lifetime, Biophys. J. 109 (2015) 380–389. https://doi.org/10.1016/j.bpj.2015.06.018.

[154] K. Dimitrievski, M. Zäch, V.P. Zhdanov, B. Kasemo, Imaging and manipulation of adsorbed lipid vesicles by an AFM tip: Experiment and Monte Carlo simulations, Colloids Surfaces B Biointerfaces. 47 (2006) 115–125. https://doi.org/10.1016/j.colsurfb.2005.12.002.

[155] K.S. Lim, M.S. Mohamed, H. Wang, Hartono, M. Hazawa, A. Kobayashi, D.C.C. Voon, N. Kodera, T. Ando, R.W. Wong, Direct visualization of avian influenza H5N1 hemagglutinin precursor and its conformational change by high-speed atomic force microscopy, Biochim. Biophys. Acta - Gen. Subj. 1864 (2020) 0–1. https://doi.org/10.1016/j.bbagen.2019.02.015.

[156] Z. Liu, Y. Zu, Y. Fu, Z. Zhang, R. Meng, Assembling and imaging of his-tag green fluorescent protein on mica surfaces studied by atomic force microscopy and fluorescence microscopy, Microsc. Res. Tech. 71 (2008) 802–809. https://doi.org/10.1002/jemt.20622.

[157] S.J. Gamblin, J.J. Skehel, Influenza hemagglutinin and neuraminidase membrane glycoproteins, J. Biol. Chem. 285 (2010) 28403–28409. https://doi.org/10.1074/jbc.R110.129809.

[158] F. Yang, L.G. Moss, G.N. Phillips, The Molecular Structure of Green Fluorescent Protein The Molecular Structure of Green Fluorescent Protein, Nat. Biotechnol. 14 (2011) 1246–1251. http://www.nature.com/naturebiotechnology.

[159] P. West, A Guide to AFM Image Artifacts, Pacific Nanotechnology Inc. [Online; accessed 15-December-2021]. https://www.physik.uni-wuerzburg.de/fileadmin/physik-fpraktikum/2020/AFM/AFM_Bild-Artefakte.pdf.

[160] S.J. Attwood, Y. Choi, Z. Leonenko, Preparation of DOPC and DPPC supported planar lipid bilayers for atomic force microscopy and atomic force spectroscopy,

Int. J. Mol. Sci. 14 (2013) 3514–3539. https://doi.org/10.3390/ijms14023514.

[161] M. Stelzle, R. Miehlich, E. Sackmann, Two-dimensional microelectrophoresis, Biophys. J. 63 (1992) 1346–1354.

[162] A. Benda, M. Beneš, V. Mareček, A. Lhotský, W.T. Hermens, M. Hof, How to determine diffusion coefficients in planar phospholipid systems by confocal fluorescence correlation spectroscopy, Langmuir. 19 (2003) 4120–4126. https://doi.org/10.1021/la0270136.

[163] G. Raghunath, R.B. Dyer, Kinetics of Histidine-Tagged Protein Association to Nickel-Decorated Liposome Surfaces, Langmuir. 35 (2019) 12550–12561. https://doi.org/10.1021/acs.langmuir.9b01700.

[164] J.E. Goose, M.S.P. Sansom, Reduced Lateral Mobility of Lipids and Proteins in Crowded Membranes, PLoS Comput. Biol. 9 (2013). https://doi.org/10.1371/journal.pcbi.1003033.

[165] Y. Deng, Y. Wang, B. Holtz, J. Li, N. Traaseth, G. Veglia, B.J. Stottrup, R. Elde, D. Pei, A. Guo, X.Y. Zhu, Fluidic and air-stable supported lipid bilayer and cell-mimicking microarrays, J. Am. Chem. Soc. 130 (2008) 6267–6271. https://doi.org/10.1021/ja800049f.

[166] M.O. Altman, M. Angel, I. Košík, N.S. Trovão, S.J. Zost, J.S. Gibbs, L. Casalino, R.E. Amaro, S.E. Hensley, M.I. Nelson, J.W. Yewdell, Human influenza a virus hemagglutinin glycan evolution follows a temporal pattern to a glycan limit, MBio. 10 (2019) 1–15. https://doi.org/10.1128/mBio.00204-19.

[167] J.H. Crowe, L.M. Crowe, J.F. Carpenter, C. Aurell Wistrom, Stabilization of dry phospholipid bilayers and proteins by sugars., Biochem. J. 242 (1987) 1–10. https://doi.org/10.1042/bj2420001.

[168] K. Hellman, D.S. Miller, K.A. Cammack, The effect of freeze-drying on the quaternary structure of l-asparaginase from Erwinia carotovora, Biochim. Biophys. Acta. 749 (1983) 133–142. https://doi.org/10.1016/0167-4838(83)90245-5.

[169] D. Zygmunt, P. Labrude, C. Vigneron, D. Larcher, Structure and functional properties of oxyhaemoglobin regenerated from methaemoglobin obtained chemically or by freeze-drying, Int. J. Biol. Macromol. 9 (1987) 197–204. https://doi.org/10.1016/0141-8130(87)90053-5.

[170] J.H. Crowe, F.A. Hoekstra, L.M. Crowe, Anhydrobiosis, Annu. Rev. Physiol. 54 (1992) 579–599. https://doi.org/10.1146/annurev.ph.54.030192.003051.

[171] S. Chiantia, N. Kahya, P. Schwille, Dehydration damage of domain-exhibiting supported bilayers: An AFM study on the protective effects of disaccharides and other stabilizing substances, Langmuir. 21 (2005) 6317–6323. https://doi.org/10.1021/la050115m.

[172] A. Dhaliwal, A. Khondker, R. Alsop, M.C. Rheinstädter, Glucose can protect membranes against dehydration damage by inducing a glassy membrane state at low hydrations, Membranes (Basel). 9 (2019). https://doi.org/10.3390/membranes9010015.

[173] C.W. Harland, D. Rabuka, C.R. Bertozzi, R. Parthasarathy, The Mycobacterium tuberculosis virulence factor trehalose dimycolate imparts desiccation resistance to model mycobacterial membranes, Biophys. J. 94 (2008) 4718–4724. https://doi.org/10.1529/biophysj.107.125542.

[174] M.A. Holden, S.Y. Jung, T. Yang, E.T. Castellana, P.S. Cremer, Creating fluid and air-stable solid supported lipid bilayers, J. Am. Chem. Soc. 126 (2004) 6512–6513. https://doi.org/10.1021/ja048504a.

[175] J.H. Crowe, L.M. Crowe, Water and Ions in Biological Systems, eds., A. Pullman A, V. Vasilescu, L. Packer, Chapter: Hydration Dependent Lipid Phase Transitions in a Biological Membrane, 1st Ed., Springer Publishing Co., U.S.A. (1985). https://doi.org/https://doi.org/10.1007/978-1-4899-0424-9_44.

[176] S. Malik, A. Debnath, Dehydration induced dynamical heterogeneity and ordering mechanism of lipid bilayers, J. Chem. Phys. 174904 (2021). https://doi.org/10.1063/5.0044614.

[177] E.A. Disalvo, F. Lairion, F. Martini, E. Tymczyszyn, M. Frías, H. Almaleck, G.J. Gordillo, Structural and functional properties of hydration and confined water in membrane interfaces, Biochim. Biophys. Acta - Biomembr. 1778 (2008) 2655–2670. https://doi.org/10.1016/j.bbamem.2008.08.025.

[178] J.H. Crowe, L.M. Crowe, F.A. Hoekstra, Phase transitions and permeability changes in dry membranes during rehydration, J. Bioenerg. Biomembr. 21 (1989) 77–91. https://doi.org/10.1007/BF00762213.

[179] F. Albertorio, A.J. Diaz, T. Yang, V.A. Chapa, S. Kataoka, E.T. Castellana, P.S. Cremer, Fluid and air-stable lipopolymer membranes for biosensor applications, Langmuir. 21 (2005) 7476–7482. https://doi.org/10.1021/la050871s.

[180] F.R. Landsberger, J. Lenard, J. Paxton, R.W. Compans, Spin-labeled electron spin resonance study of the lipid-containing membrane of influenza virus., Proc. Natl. Acad. Sci. U.S.A. 68 (1971) 2579–2583. https://doi.org/10.1073/pnas.68.10.2579.

[181] A.G. Bukrinskaya, J.G. Molotkovsky, E.L. Vodovozova, Y.M. Manevich, L.D. Bergelson, The molecular organization of the influenza virus surface. Studies using photoreactive and fluorescent labeled phospholipid probes, Biochim. Biophys. Acta - Biomembr. 897 (1987) 285–292. https://doi.org/10.1016/0005-2736(87)90424-X.

[182] P.T. Ivanova, D.S. Myers, S.B. Milne, J.L. Mcclaren, P.G. Thomas, H.A. Brown, Lipid Composition of the Viral Envelope of Three Strains of Influenza Virus - Not All Viruses Are Created Equal, ACS Infect. Dis. 1 (2015) 435–442. https://doi.org/10.1021/acsinfecdis.5b00040.

[183] E.J.A. Schrauwen, M. De Graaf, S. Herfst, G.F. Rimmelzwaan, A.D.M.E. Osterhaus, R.A.M. Fouchier, Determinants of virulence of influenza A virus, Eur. J. Clin. Microbiol. Infect. Dis. 33 (2014) 479–490. https://doi.org/10.1007/s10096-013-1984-8.

[184] P. Roy, R. Noad, Virus-like particles as a vaccine delivery system: Myths and facts, Hum. Vaccin. 4 (2008) 5–12. https://doi.org/10.4161/hv.4.1.5559.

[185] A. Sabbaghi, S.M. Miri, M. Keshavarz, M. Zargar, A. Ghaemi, Inactivation methods for whole influenza vaccine production, Rev. Med. Virol. 29 (2019) 1–11. https://doi.org/10.1002/rmv.2074.

[186] B.R. Murphy, K. Coelingh, Principles Underlying the Development and Use of Live Attenuated Cold-Adapted Influenza A and B Virus Vaccines, Viral Immunol. 15 (2002) 295–323.

[187] C. Godefroy, S. Dahmane, P. Dosset, O. Adam, M.C. Nicolai, F. Ronzon, P.E. Milhiet, Mimicking influenza virus fusion using supported lipid bilayers, Langmuir. 30 (2014) 11394–11400. https://doi.org/10.1021/la502591a.

[188] AstraZeneca, Pandemic influenza vaccine H5N1 AstraZeneca nasal spray, Suspension (2009). [Online; accessed 20-February-2022]. https://www.ema.europa.eu/en/documents/product-information/pandemic-

influenza-vaccine-h5n1-astrazeneca-epar-product-information_en.pdf.

[189] P.J. de Pablo, I.A.T. Schaap, Atomic Force Microscopy of Viruses, Adv. Exp. Med. Biol. 1140 (2019) 159–179. https://doi.org/10.1007/978-3-030-14741-9_8.

[190] M. Brogly, F. Ahmad, S. Bistac, Scanning Probe Microscopy in Nanoscience and Nanotechnology 2, ed., B. Bhushan, Chapter 16: Assessment of Nanoadhesion and Nanofriction Properties of Formulated Cellulose-Based Biopolymers by AFM, 1st Ed., Springer Publishing Co., U.S.A. (2011). https://doi.org/10.1007/978-3-642-10497-8_16.

[191] N. Martín-González, A. Ortega-Esteban, F. Moreno-Madrid, A. Llauró, M. Hernando-Pérez, P.J. de Pablo, Atomic Force Microscopy of Protein Shells: Virus Capsids and Beyond, Chapter 15: Single Molecule Analysis: Methods and Protocols, Methods in Molecular Biology, 1st Ed., Springer Publishing Co., U.S.A. (2017). https://doi.org/10.1007/978-1-4939-7271-5_15.

[192] A.R. Mackie, A.P. Gunning, M.J. Ridout, V.J. Morris, Gelation of gelatin observation in the bulk and at the air-water interface, Biopolymers. 46 (1998) 245–252. https://doi.org/10.1002/(sici)1097-0282(19981005)46:4<245::aid-bip6>3.0.co;2-p.

[193] V.I. Uricanu, M.H.G. Duits, R.M.F. Nelissen, M.L. Bennink, J. Mellema, Local structure and elasticity of soft gelatin gels studied with atomic force microscopy, Langmuir. 19 (2003) 8182–8194. https://doi.org/10.1021/la0347004.

[194] M.G. Mateu, Mechanical properties of viruses analyzed by atomic force microscopy: A virological perspective, Virus Res. 168 (2012) 1–22. https://doi.org/10.1016/j.virusres.2012.06.008.
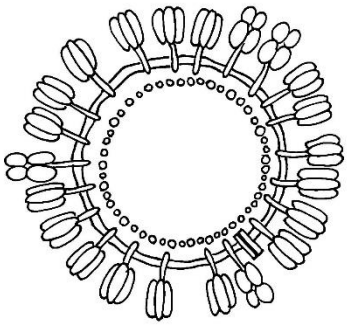
[195] B. Srinivasan, H. Rokadia, S. Tung, R. Wang, Y. Li, AFM investigation of avian influenza viruses, ASME Int. Mech. Eng. Congr. Expo. Proc. 2 (2010) 277–281. https://doi.org/10.1115/IMECE2010-38952.